Pure

Scotland's Rural College

An overview of converting reductive photocatalyst into all solid-state and direct Z-scheme system for water splitting and CO2 reduction

Raizada, Pankaj; Kumar, Abhinandan; Hasija, Vasudha; Singh, Pardeep; Thakur, Vijay Kumar; Khan, Aftab Aslam Parwaz

==An overview of== converting reductive photocatalyst into all ~~solid~~ solid-state and direct Z-scheme system for water splitting and CO₂ reduction

Pankaj Raizada[a,b], Abhinandan Kumar[a], Vasudha Hasija[a], Pardeep Singh [a,b] Vijay Kumar Thakur[c*], Aftab Aslam Parwaz Khan[d,e]*

[a]School of Chemistry, Faculty of Basic Sciences, Shoolini University, Solan (HP), India--173229

[b]Himalayan Centre for Excellence in Nanotechnology, Shoolini University. Solan (HP) India-173229

[c]Biorefining and Advanced Materials Research Center, Scotland's Rural College (SRUC), Kings Buildings, West Mains Road, Edinburgh EH9 3JG, UK

[d]Center of Excellence for Advanced Materials Research, King Abdulaziz University, P. O. Box 80203, Jeddah 21589, Saudi Arabia

[e]Chemistry Department, Faculty of Science, King Abdulaziz University, P. O. Box 80203, Jeddah 21589, Saudi Arabia

*Corresponding authors: pankajchem1@gmail.com; vijay.kumar@cranfield.ac.uk

Abstract

Considering the current scenario of rising environmental and energy concerns, engineering of Z-scheme photocatalytic systems is in the spotlight. The prime reason for this includes efficient redox abilities and effective space separation along with the migration of photoinduced charge carriers over conventional heterojunction systems. Herein we foreground the stumbling blocks of traditional heterojunction systems and enlighten the generations of Z-scheme photocatalysis originating from liquid-phase to direct Z-scheme photocatalytic systems. We provide substantial criteria and selection aspects of choosing reductive type photocatalysts as a potential aspirant for the Z-scheme photocatalytic system. As Z-scheme photocatalytic systems render effective space separation of photogenerated carriers, active species generation, wide optical absorption and amended redox ability. We focus on comprehensive illustration of all solid solid-state and direct Z-scheme photocatalysts by coupling reductive type photocatalysts with other semiconductor material and explored their potential for efficacious conversion of solar energy into functional energy. Herein, we aim to provide in-depth and updated criteria of for selecting Z-scheme photocatalysts for CO_2 reduction, water splitting, and nitrogen fixation. Lastly, the article compiles with a conclusive note about future perspectives and challenges accompanying all solid solid-state and direct Z-scheme Z photocatalysts and their energy conversion applications.

Abbreviations

A/D, Acceptor/donor; AOT, Advanced oxidation technology; ASS, All solid state; Eg, Band gap energy ; CNTs, Carbon nano tubes; CNS, Carbon nano sheets; CB, Conduction band; DFT, density function theory; DMP, 1,2 dimethyl phenol; DBP, 1,2 dibromophenol; electron-hole pair, EHP; EM , electron mediator; ESR, electron spin resonance; e^-, electron; Er, erythromycin; GO, graphene oxide; $g\text{-}C_3N_4$, graphitic carbon nitride; HOMO, Highest occupied molecular orbital; h^+, hole; HER, Hydrogen evolution rate; OH^-, Hydroxyl radical; IEF; interfacial electric field; LUMO, lowest unoccupied molecular orbital; MoS_2, molybdenum disulfide; NPs, nanoparticles; NSs, Nanosheets; NOM, natural organic matter; NIR, near infrared region; OWS, overall water splitting; OER, Oxygen evolution rate; $\cdot O_2^-$, peroxide; PL, Photoluminescence; PS, Photosystem; Pg, protonated; QD, quantum dots; ROS, reactive oxygen species; rGO, reduced graphene oxide; RhB, rhodamine B; SC, semiconductor; EPR; Spin trapping electron paramagnetic resonance; $\cdot O_2^{-2}$, superoxide; SPR, Surface plasmon resonance; TC, tetracycline; TCH, tetracycline hydrochloride; TOC, total organic carbon; TEM, Transmission electron microscopy; TCP, 2,4,6-tricholorphenol; TEOA, triethanolamine; VB, valence band; XRD, X-ray diffraction; XPS, X-ray photoelectron spectroscopy.

Contents

1. Introduction

Nowadays, industrial indispensability and accelerating anthropogenic activities have reached ~~to~~ an alarming level. The interminable increasing challenges related to dwindling renewable natural resources, solar energy conservation and environmental pollutions are of great concern [1-3]. The overriding issues impede global energy consumption; therefore, it is indispensable to explore eco-friendly technologies for environment protection and energy resorption. A sought-after advanced oxidation technology (AOT); Honda and Fujishima effect stimulated the age of heterogeneous photocatalysis with titanium dioxide (TiO_2). Photocatalysis involves the photoassisted generation of strong oxidant holes (h^+) in the valence band (VB) and reductant electrons (e^-) in the conduction band (CB) of the semiconductor photocatalysts after the absorption of solar energy. In detail, when a semiconductor photocatalyst is exposed under visible-light with energy greater than or equal to their bandgap energy, the VB electrons get promoted to ~~higher~~ higher-level CB generating a hole behind in VB (Fig. 1a). After excitation, the photoinduced excitons migrate to the surface of photocatalyst. For efficient photocatalysis, the CB electrons should possess strong reduction ability with a chemical potential in the range of +0.5 to -1.5 V (vs NHE) and the VB holes should possess strong oxidising capacity with oxidation potential in the range of +1.0-+3.5 V (vs NHE) [4-11]. The process further involves the interfacial transfer of photocarriers which generates various reactive oxygen species (ROS) like; peroxide ($O_2\cdot$), superoxide ($\cdot O_2^-$), and hydroxyl radicals ($\cdot OH$) which participate in photodegradation of pollutants, reduction of CO_2 to hydrocarbon fuels, overall water splitting, N_2 fixation and biohazard disinfection [12-15]. However, after excitation, the electrons might reassemble and dissipate the input energy in the form of light or heat which needs to be addressed in order to attain higher photocatalytic efficacy. To date, designing a robust promising photocatalyst to overcome indisputable energy inadequacy and environmental degradation has become a cutting-edge research topic [16-19]. For effectual conversion of solar energy into functional fuels, various reductive type photocatalysts (ZnS, CdS, Ta_3N_5, $TaON$, Cu_2O, SiC, Bi_2S_3 etc)

5

154 which fulfil the necessary criteria of a photocatalytic process have been reported. However,

155 the cost-effectiveness and physico-chemical stability hinders their photocatalytic efficiency.

156 Therefore, to accentuate the journey of delivering large-scale benefits in the province of

157 photocatalysis, graphitic carbon nitride (g-C$_3$N$_4$) has garnered incredible fascination among

158 scientific communities. Moreover, g-C$_3$N$_4$ on account of its hierarchical properties including

159 appropriate optical band gap ~2.7 eV (with oxidative potential at +1.57 V and reductive at -

160 1.13 V vs NHE at pH 7) is an utterly smart solar light harvesting photocatalyst [5, 9].

161 Moreover, its substantially accessible surface sites with high thermal and chemical stability

162 offers unprecedented breakthroughs in various realms of environment conservation [20, 21].

163 For achieving high space charge separation efficacy and broad visible light absorption, many

164 strategies like, coupling, doping, co-catalyst incorporation and heterojunction construction

165 have been frequently adopted. Out of all these strategies, heterojunction formation proves its

166 worth and can be classified as conventional [22-25] and Z-scheme heterojunctions [26-30].

167 Conventional heterojunction formation involves semiconductor composites which are formed

168 by the combination of two or more semiconductors depending upon their band gaps [31-37].

169 These are further of three types as shown in (Fig. 1b-d). In type-I heterojunction, VB of

170 semiconductor-II (SC-II) lies lower than semiconductor-I (SC-I), and CB of SC-II is higher

171 than the CB of SC-I forming a straddling gap. The migration of charge carriers proceeds in a

172 way that gathering of electrons and holes occurs only on SC-I resulting. It causes poor charge

173 separation of photogenerated electron and hole pairs along with lower redox potential as both

174 oxidation and reduction reactions occur at the same semiconductor [22, 23]. In type-II

175 heterojunction, the band positions are at optimal levels (staggered gap) that offer spatial

176 charge carrier separation with enhanced photocatalytic efficacy as compared to type-I. But its

177 redox potential is low due to occurrence of oxidation and reduction reactions on SC-I with

178 lower oxidation potential and SC-II with lower reduction potential. Type-III heterojunctions

179 have broken gap situation involving separation of charge carriers similar to type-II

180 heterojunctions [22, 38]. The broken band–gap in type-III heterojunction does not intersect

181 causing no charge carrier separation for enhanced photocatalytic activity.

182 **< Please Insert Fig. 1 Here>**

183 ~~In order t~~To encounter the aforementioned issues and to achieve superior photocatalytic

184 efficiency, Z-scheme heterojunction systems have intrigued researchers [27, 28]. The

185 concept of Z-scheme photocatalysis was initially introduced by Bard in 1979. Ensuing ideal

186 conditions for photocatalysis, Z-scheme heterojunction results in more negative CB edge

187 and more positive VB edge thus narrowing band-gap of semiconductor [39]. The progression

188 path of Z-scheme photocatalysis from the first generation to the third generation has been

189 depicted in (Fig. 2). In contrast to type-II heterojunction, photogenerated electron-hole pair

190 (EHP) separation in Z-scheme follows a different pathway (Fig. 3b-d). In Z-scheme mode,

191 upon visible light irradiation electrons in CB of SC-II combines with photogenerated VB

192 holes of SC-I. This leads to the formation of sufficiently strong oxidative VB holes in SC-II

193 and reductive electrons in CB of SC-I. Due to the difference in band alignment and work

194 function of the semiconductor photocatalysts, the resulting induced interface electric field

195 expedite separation of EHP. The name Z-scheme is proposed because it imitates natural

196 photosynthesis in plants and follows the same mechanism of charge transfer pathway that

197 contains two-step photoexcitation which shows resemblance to the letter 'Z'. Natural

198 photosynthesis involves two photo-induced chemical reactions in PS I (photosystem I) and

199 PS II (photosystem II) with various intermediary enzymes which endorse oxidation and

200 reduction reactions as shown in (Fig. 3a). Firstly, PS I accompanying chlorophyll P680

201 under solar light irradiation are converted to excited state $P680^*$ as (Eq.1):

$$\text{chlorophyll } P680 + h\nu \rightarrow \text{chlorophyll } P680^* \qquad (1)$$
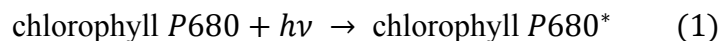
203 Simultaneously, oxidation of water molecules generates O_2 on chlorophyll P680. The

204 electrons migrate from $P680^*$ to chlorophyll P700 (accompanying PS ll) in presence of

205 enzymatic action via electrons transfer chain. Upon absorption of sun-light, chlorophyll P700

206 changes to excited state chlorophyll $P700^*$ as:

$$\text{chlorophyll } P700 + h\nu \rightarrow \text{chlorophyll } P700^* \qquad (2)$$
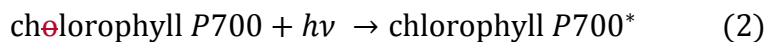
208 The photoexcited electrons react with $NADP^+$ to produce reduced coenzyme-II which is

209 further used for the reduction of CO_2 [40]. Z-scheme is categorised into three main

210 generations as depicted in Fig. 3b-d. The first generation is liquid phase Z-scheme

211 photocatalyst, fabricated by coupling of two different semiconductor materials via a shuttle

212 redox liquid-state mediator (species which acts as an electron acceptor and donor (A/D) pair)

213 [41,42]. Both SC-I and SC-II get photoexcited under solar light illumination and release
214 electrons and holes in CB and VB, respectively (Fig. 3b). Further, migration of CB electrons
215 from SC-II to VB of SC-I takes place through redox mediator by following reactions [Eq. 3
216 and 4], resulting in the formation of holes in VB of SC-II.

$$A + e^-(\text{at CB of SC} - \text{ll}) \rightarrow D \quad\quad\quad (3)$$

$$D + h^+(\text{at VB of SC} - \text{l}) \rightarrow A \quad\quad\quad (4)$$
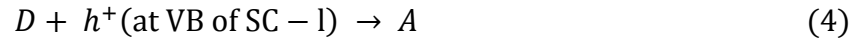
219 By this process, photoexcited electrons remain on SC-l with more reduction potential,
220 whereas the photogenerated holes remain on SC-II. In this way, the optimal spatial charge
221 separation along with optimized redox potential is achieved. However, there are some typical
222 shortcomings in the first generation of Z-scheme like, (1) Use of reversible shuttle redox
223 mediators like I^-/IO_3^- and Fe^{2+}/Fe^{3+} causes a backward reaction [22]. During the
224 photochemical reaction, donor and acceptor species like Fe^{2+} and Fe^{3+} will compete with
225 reactants for oxidation and reduction reactions, respectively. So, overall photocatalytic
226 efficacy of Z-scheme system is lowered. Moreover, the liquid phase Z-scheme system is
227 operational in a liquid state only and hence limits its application for gaseous and solid phase
228 systems.

229 **<Please Insert Fig. 2 Here>**

231 The second generation of Z-scheme photocatalysis is all-solid-state (ASS) photocatalytic
232 system [43, 44]. ASS Z-scheme systems are designed by combining two different
233 semiconductor materials and an electron mediator at the surface junction which are usually
234 noble-metal nanoparticles (NPs) (Ag, Au, Pt, Bi and Cu) or carbon materials like (graphene
235 oxide (GO), carbon nanotubes (CNT's), reduced graphene oxide (RGO) and carbon [45] (Fig.
236 3c). Noble-metal NPs, are proven to be successful in eliminating backward reaction occurring
237 in first first-generation Z-scheme systems. However, the applicability of metal NPs (NPs) at
238 semiconductor surface junction is accompanied with certain inherited limitations *i.e.* its high
239 cost, photo-corrosive nature and strong optical light absorption which narrows its wide-scale
240 applications [46]. Thus, mediator free ASS Z-scheme system was introduced by Wang and his
241 peer group in 2009, using ZnO and CdS system in direct contact with each other [47] (Fig.
242 3d). Thereafter in 2013, the third generation of Z-scheme entitled as direct Z-Scheme

243 photocatalyst get acquainted to overcome all drawbacks of first and second-generation Z-
244 scheme aimed for enhanced photocatalytic efficiency and redox potential. As the name
245 implies in-direct Z-scheme photocatalyst, two photocatalytic systems form a direct surface
246 junction with each other omitting requirement of redox mediators or noble metals at interface
247 thereby, reducing light light-shielding effect and lowering manufacturing cost [48-50].
248 Though both the Z-scheme system and type-II photocatalytic systems have the same structure
249 yet their charge separation mechanism is totally different. In direct Z-scheme, photoinduced
250 CB electrons in SC-II possessing less reduction potential combine with VB-holes in SC-l with
251 low oxidation potential. By this means, SC-II is occupied with photogenerated holes
252 possessing high oxidation potential and photo-irradiated electrons possessing high reduction
253 potential remains in SC-I thereby, optimum space charge separation along with superior redox
254 ability is accomplished. Direct Z-scheme photocatalyst attains comparatively greater
255 photocatalytic activity than the type-II system as the charge migration pathway is
256 substantially more favourable. In direct Z-scheme, migration of charge carriers is
257 thermodynamically feasible by electrostatic attraction among photogenerated charge carriers.
258 For fabrication of direct Z-scheme robust photocatalyst, appropriate band positions with
259 extended solar light harvesting range is are required [39, 51-53].

<Please Insert Fig. 3 Here>

261

262 Hitherto, intensive research studies have been incorporated on exploring the potential of Z-
263 scheme photocatalytic systems for environmental and energy concerns [54]. For example, Xu
264 *et al*. represented a comprehensive viewpoint involving designing, modification and
265 applications of direct Z-scheme photocatalysts for modulating optoelectronic properties of
266 semiconductor photocatalysts [55]. Similarly, Low *et al*. summarized potentials of direct Z-
267 scheme heterojunction systems over conventional double charge transfer system and depicted
268 the characterization techniques to verify the formation of direct Z-scheme system along with
269 their useful photocatalytic applications. Considering all the significant efforts to exploit the
270 fascinating features of Z-scheme photocatalytic systems, the present study summarizes an all-
271 inclusive overview on of the criteria and selectivity aspects required for photocatalytic
272 conversion of CO_2 along with water splitting. We believe that a comprehensive review
273 focusing on reductive type photocatalyst hybridized with other semiconductor material

forming ASS and direct Z-scheme system can effectively offer new ideas for selecting and synthesizing new photocatalysts which can fulfil the criteria of energy conversion applications. To date, no such study mentioning criteria for photocatalytic CO_2 reduction and water splitting along with selectivity aspects utilizing reductive type photocatalyst ~~have~~ has been reported. Furthermore, we aim to represent the importance of converting conventional heterostructure into ASS and direct Z-scheme heterojunction system ~~in order~~ to achieve amended space charge isolation of photocarriers to carryout photo-redox reactions at distinct semiconductor materials. We further assume that the critical insight into the mechanistic viewpoint of ASS and Z-scheme heterostructures could bring substantial improvement in the field of photocatalysis. To get a measure of the catalog of different research articles related to ASS and direct Z-scheme photocatalysts, we cruised data with the help of 'Scopus' database as it provides the most significant citations. Moreover, it is one of the most authentic means of receiving information regarding current drifts and historic progression in the research field. Through Scopus, we found 2588 and 3181 articles by using keywords "All ~~solid~~ solid-state Z-scheme photocatalysts" and "Direct Z-scheme photocatalysts, respectively from 2009 to January, 2020 (Fig. 4a). Furthermore, Fig. 4b and c represent the applicability of ASS and direct Z-scheme systems in pollutant degradation, CO_2 reduction, overall water splitting and H_2 production. The main discussion of the present review is divided into the following sections:

- ~~Basic~~ The basic principle of photocatalytic CO_2 reduction and water splitting.
- ~~Selectivity~~ The selectivity of the photocatalyst.
- All-solid-state Z-scheme photocatalysts.
- Direct Z-scheme photocatalysts.
- Photocatalytic CO_2 reduction.
- Photocatalytic water splitting.
- Other application.
- Conclusion and viewpoint.

<center>**<Please Insert Fig. 4 Here>**</center>

2. ~~Basic~~ The basic principle of Photocatalytic CO_2 reduction

304 Currently, about 6 billion tons of CO_2 is released into the atmosphere which is causing severe

305 climate and health issues. As a consequence of ~~elevating~~ elevated CO_2 levels in the atmosphere,

306 global warming is one of the growing worldwide concerns. The photoassisted reduction of CO_2

307 into functional hydrocarbon fuels has become an attractive pursuit to produce clean energy and

308 tackle the energy and environment problems [56]. The era of photocatalytic CO_2 reduction

309 started back in the 1970s by the photoconversion of CO_2 into useful organic compounds [57].

310 Thereafter, with increasing advancements in technology, the process of photocatalytic CO_2

311 reduction gained significant pace. The photoreduction process mainly involves the recycling of

312 CO_2 and subsequent generation of functional chemical fuels [58]. In detail, for photo-reduction

313 of CO_2, the prerequisite condition is the use of appropriate photocatalyst to deploy visible light

314 and a resulted photoreaction with CO_2 in gaseous or aqueous phase system. As a result of photo-

315 oxidation reactions, the photocatalyst will reduce CO_2 to different hydrocarbons like methanol,

316 methane, formic acid hydrogen and formaldehyde which can be utilized as fuel and feedstock for

317 different reactions depending upon its reduction potential [59]. Since the gaseous CO_2 is

318 relatively stable with $\Delta G_f^0 = -394.4\ kJmol^{-1}$, therefore, external energy must be supplied for its

319 transformation into reduced products [60]. Moreover, for spontaneous photo-reduction of CO_2

320 (ΔG = negative), the applied potential should be more negative than the standard reduction

321 potential. The formal redox potentials required for different photocatalytic CO_2 reduction

322 reactions can be obtained from thermodynamic studies and are given in Eq. 5-11.
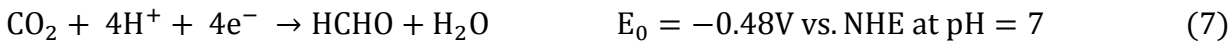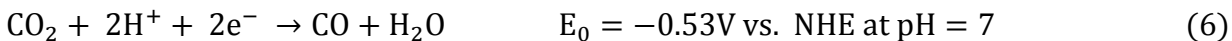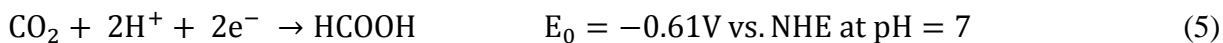
323

324 $\quad CO_2 + 2H^+ + 2e^- \rightarrow HCOOH \qquad\qquad E_0 = -0.61V\ vs.\ NHE\ at\ pH = 7 \qquad\qquad (5)$

325

326 $\quad CO_2 + 2H^+ + 2e^- \rightarrow CO + H_2O \qquad\qquad E_0 = -0.53V\ vs.\ NHE\ at\ pH = 7 \qquad\qquad (6)$

327

328 $\quad CO_2 + 4H^+ + 4e^- \rightarrow HCHO + H_2O \qquad\qquad E_0 = -0.48V\ vs.\ NHE\ at\ pH = 7 \qquad\qquad (7)$

329

330 $\quad CO_2 + 6H^+ + 6e^- \rightarrow CH_3OH + H_2O \qquad\qquad E_0 = -0.38V\ vs.\ NHE\ at\ pH = 7 \qquad\qquad (8)$

331

332 $\quad CO_2 + 8H^+ + 8e^- \rightarrow CH_4 + 2H_2O \qquad\qquad E_0 = -0.24V\ vs.\ NHE\ at\ pH = 7 \qquad\qquad (9)$

333

334 $\quad 2H^+ + 2e^- \rightarrow H_2 \qquad\qquad E_0 = -0.41V\ vs.\ NHE\ at\ pH = 7 \qquad\qquad (10)$

$$2H_2O + 4H^+ \rightarrow O_2 + 4H^+ \qquad\qquad E_0 = +0.82V \text{ vs. NHE at pH} = 7 \qquad (11)$$

The efficiency of photocatalytic CO_2 conversion depends directly on the band-gap energy of the photocatalytic material along with appropriate redox potential values. In general, the effective transmission of electrons to the surface of photocatalyst containing adsorbed CO_2 is thermodynamically feasible only if the CB edge of semiconductor material lies at more negative potential than the required standard potential. For instance, the photocatalytic CO_2 reduction into methanol can be facile if the CB of semiconductor photocatalyst lies at potential more negative than -0.38 V which is the standard reduction potential for CO_2 conversion into methanol at pH 7 vs. NHE [58, 61].

Consequently, a suitable photocatalytic material for photo-reduction of CO_2 must fulfil the following criteria:

(i) transmission of multiple electrons from photocatalyst to adsorbed CO_2; (ii) the CB positioning in semiconductor photocatalyst should lie at more negative potential than the CO_2 redox potential and its subsequent reduced products; (iii) the facile adsorption of reactant molecules like, H_2O, CO_2 and carbonates on photocatalyst and desorption of products through diffusion into the system after photo-reduction reaction; (iv) the photoinduced VB holes of a semiconductor should interact with oxide species (H_2O or other sacrificial agents) to avoid the recombination with electrons as well as secondary reactions with the reduced products (as shown in Eq. 11) [62]. Thus, based on the above discussion it can be assumed that the ability of photo-reduction of CO_2 can be significantly enhanced *via* the synergistic effect of optimal CO_2 adsorption, broad visible light absorption and efficacious charge separation.

In general, from the aforementioned chemical equations, it can be seen that there is a need of for hydrogen source and electron donor for the photoassisted reduction of CO_2 which can be fulfilled by H_2O. However, there lies an uncertainty for using H_2O as an electron donor due to its ability to indulge into a side reaction for the production of H_2 as shown by Eq. 10 [63]. During photocatalytic reduction of CO_2, H_2O can undergo both oxidation (by VB holes) and reduction (by CB electrons) to produce O_2 and H_2, respectively. This can significantly obstruct the photo-reduction efficacy of CO_2 into hydrocarbon fuels. Consequently, the overall photoassisted reduction efficiency of CO_2 is comparably lower than that of H_2 generation through water

splitting which is in agreement with thermodynamic and kinetic studies [64]. As per thermodynamic consideration, the photocatalytic CO_2 reduction requires six to eight electrons with more negative reduction value than two-electron reduction process for photocatalytic H_2 generation. Simultaneously, the complex mechanism of CO_2 photo-reduction must involve basic chemical reaction involving the transference of electrons and protons to adsorbed CO_2. Thus, the photocatalyst must overcome thermodynamic as well as the kinetic criterion by generating spatially separated reaction sites to avoid subsequent H_2 production and facile photocarriers transfer to CO_2 [62,64,65]. So far, Z-scheme photocatalysts are capable to exhibit effective space separation of photocarriers and incremented redox abilities for efficient photo-reduction of CO_2 into hydrocarbons. The effectual migration and space isolation *via* Z-scheme mode renders superior redox ability to the photocatalytic system which can be substantially utilised in photoreduction reaction.

3. Basic The basic principle of photocatalytic water splitting

The increasing concerns of environment and energy disputes have led researchers to exploit sustainable and re-generated fuels possessing energy-dense and green features [66-69]. Hydrogen (H_2), a carbon carbon-free energy carrier owning exceptional energy density along with heat value 120-140 $MJKg^{-1}$, is a best best-suited alternative till date to replace traditional fossil fuels as it does not generate pollutants during combustion. Currently, about 44.5 million tons of H_2 is produced worldwide and with such production rate, it will take years for H_2 to become the primary source of energy [70]. Artificial photosynthesis phenomenon for photocatalytic solar to chemical energy conversion offers highly significant means to generate fuels from the water with minimal impact on the environment. Utilizing solar energy and joining it with water by means of utilizing photoassisted water splitting offers a great deal for H_2 generation. In photocatalytic water splitting, water is introduced into a module designed for water splitting and converted into H_2, which is further utilized in systems to generate high high-efficiency power. Considering that, the basic criteria of generating H_2 and O_2 at the solid-liquid interface strictly rely on efficient visible light harvesting. As such, the efficacious utilization of visible light leads to the conversion of solar energy into chemical functional energy and its storage for further usage [71, 72]. Overall water splitting into H_2 and O_2 is an uphill chemical reaction (Eq. 16) which accompanies an increase in Gibbs free energy [73] as shown below:

$$H_2O \rightarrow \frac{1}{2}O_2 + H_2 \qquad E_0 = 1.23 \text{ eV vs NHE at pH} = 0 \qquad (\Delta G^0 = 237 kJmol^{-1}) \quad (16)$$
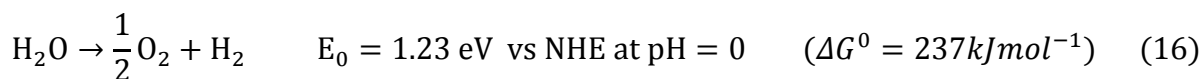
Due to uphill reaction kinetics, there is a need ~~of~~ for external energy to carry out the ~~water~~ water-splitting reaction. In photocatalytic water splitting, visible light is the external driving force which converts solar energy into hydrogen by utilizing water as the only reactant. Due to slow reaction kinetics, the involvement of semiconductor photocatalysts into the phenomenon becomes necessary. The basic criteria to evolve H_2 and O_2 involve the absorption of photons by semiconductor photocatalyst to generate holes and electrons which participate in the oxidation of H_2O and reduction of H^+, respectively. Moreover, the overall aspects including efficacy, cost-effectiveness and stability must be superior in comparison with industrial processes of generating H_2 ~~in order~~ to achieve the widespread application of visibly driven photocatalytic water splitting. In detail, during photocatalytic water splitting following steps take place; (i) After absorbing energy greater than the band-gap of the semiconductor, VB electrons get excited to CB thereby, produce electrons and holes (ii) photo-excited electrons and holes independently get diffused on the semiconductor surface, and (iii) subsequently undergoes surface chemical reactions involving oxidation and reduction of water by photogenerated holes and electrons to produce O_2 and H_2, respectively as shown by (Eq. 17 and 18);

$$2H^+ + 2e^- \rightarrow H_2 \qquad E_0 = \ 0 \text{ eV vs. NHE at pH} = 0 \qquad (17)$$
$$H_2O \rightarrow 4H^+ + 4e\text{-} + O_2 \qquad E_0 = 1.23eV \text{ vs. NHE at pH} = 0 \qquad (18)$$
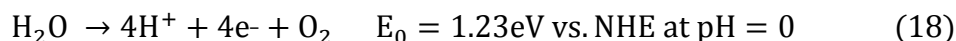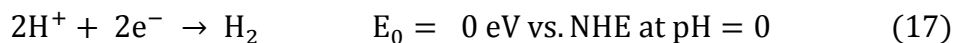
Thermodynamically, the prerequisites for aforementioned reactions to~~–~~ proceed are; the CB minimum for a photocatalyst must lie at more negative potential than that of H^+/H_2 level (0 V vs. NHE at 0.059 pH), while the VB maximum should be more positive than that of O_2/H_2O energy level (1.23 V Vs. NHE) [74]. Precisely, ~~in order~~ to achieve photocatalytic OWS, a photocatalyst must overcome an energy barrier of 1.23 eV. Moreover, oxidation/reduction of water by photogenerated holes/electrons greatly depends upon band positioning of photocatalysts and redox potential of water which should be precisely matched. The schematic illustration for water splitting process is shown in (Fig. 5). In general, water splitting is a complex phenomenon posing

427 stringent conditions of selecting a photocatalyst with suitable band positioning for H_2 and O_2
428 evolution. Despite of considerable exploitation and development in the field of photocatalysis,
429 the efficiency and stability of photocatalytic water splitting still faces huge challenges from both
430 thermodynamic as well as kinetic factors due to the unsatisfactory catalytic features of the
431 semiconductor material. Moreover, notably, the insufficient STH conversion efficiency is
432 another factor that needs to be addressed effectively. For this purpose, sacrificial reagents like
433 methanol (CH_3OH) and sodium thiosulphate ($Na_2S_2O_8$) are used as irreversible electron donor
434 and acceptor in hydrogen evolution reaction (HER) and oxygen evolution reaction (OER),
435 respectively. In contrast, sacrificial half-reactions are downhill reactions comprising decrease in
436 Gibbs free energy, also photon energy doesn't get stored, hence, it is important to design
437 photocatalysts which do not need these reagents [75]. Till date, many photocatalytic water
438 splitting systems involving sacrificial agents have been reported where they promote the
439 suppression of EHP by depleting holes or by providing hydrogen atoms for H_2 evolution.
440 Besides, adding sacrificial agents into the photocatalysis generates extra chemical energy into the
441 reaction except for solar energy. Moreover, the sluggish reaction kinetics inhibits the overall
442 efficiency of photocatalytic water splitting. Thus exploring semiconductor photocatalysts with
443 significantly high-efficacy, stability, economical and physicochemical features is of utmost
444 concern for the growth of photocatalytic water splitting.

445

446 **<Please Insert Fig. 5 Here>**

447 **4. Selectivity of photocatalyst**

448 Typically, the selection of photocatalyst and various strategies to improve photocatalytic
449 performance are the most crucial aspects to be considered for achieving superior efficacy.
450 Besides, to attain pilot pilot-scale applications of the photocatalyst; recyclability, reusability and
451 photo-stability of the photocatalytic material are equally substantial. Visibly driven
452 photocatalytic water splitting process as well as photoreduction of CO₂, as well as
453 photoreduction of CO2, can be classified into three main steps: absorption of a photon,
454 migration/separation of photocarriers, and surface redox reactions. These steps strictly depend
455 upon the type of photocatalyst being employed in the photocatalytic process as discussed below.
456 The effectiveness of any photocatalytic process firmly relies on the band-gap energy as well as
457 band edge positioning of semiconductor material for efficient absorption of a photon. Since, the

15

458　initial step of photocatalysis involves the effectual harnessing of visible light which in a way

459　depends upon the bandgap energy of the semiconductor photocatalyst. In detail, upon visible

460　light exposure, the semiconductor photocatalyst possessing appropriate bandgap energy (E_g) can

461　produce photoinduced EHP by the excitation of electrons from VB of a photocatalyst to its CB

462　leaving holes behind. Only after this important step, the photocatalytic process can further

463　proceed. However, the obstacle of photocarriers recombination can significantly limit the

464　effective number of photocarriers reaching at the surface of photocatalyst which can hinder the

465　overall efficacy of the photocatalytic process. Furthermore, for adequate enhancement in the

466　photon absorption process, band engineering plays a vital role. For instance, band-gap tuning of

467　the photocatalyst through doping is one of the most crucial techniques used for this purpose [76].

468　It is widely investigated that the addition of metallic and non-metallic impurities in

469　heterojunction system can effectively enhance photoactivity by lowering the band-gap energy,

470　boosting the visible light harnessing and imparting useful physical features [77]. To date, various

471　metallic and non-metallic dopants such as; Sodium (Na), lithium (Li), copper (Cu), iron (Fe),

472　carbon (c), phosphorous (P), boron (B), sulphur (S), oxygen (O), and so many others have been

473　extensively explored [78-80]. The introduction of metal dopants into the photocatalytic system

474　can adequately enhance the solar light harvesting, decrease the band-gap and boost the

475　photocatalytic performance by improving the movement rate of photocarriers as well as by

476　reducing the reassembly of EHP [81]. For example, Gao *et al*. reported a one-step pyrolysis

477　process to design Fe-doped g-C$_3$N$_4$ nanosheets (NSs) which exhibited significantly enhanced

478　MB degradation efficacy as well as H$_2$ production rate [82]. Doping of g-C$_3$N$_4$ with Fe

479　remarkably increments the photocatalytic performance of g-C$_3$N$_4$ by tuning its electronic

480　properties. It is observed that, non-metal dopants are preferred over metal dopants as by doping

481　the system with a metal ion, the thermal stability of the system significantly decreases due to

482　mid-gap energy levels [83]. While due to high electronegativity and high ionization energy, the

483　non-metal dopants control the thermal changes and maintain the metal-free behaviour of the

484　system. Thus, through band-gap engineering, photocatalytic efficacy of the system can be

485　significantly improved by means ofemploying effective thermal and electronic features which

486　can boost the harnessing of visible light.

487　So far, it is observed that the photocatalysts with wide band-gap energy cannot harvest solar

488　energy efficiently and the photocatalysts with narrow band-gap energy undergo quick reassembly

16

of photocarriers. As a consequence, the overall photocatalytic efficacy of the system drops substantially. The second step that involves effective migration and separation of photoinduced carriers play a crucial role to increment the photoactivity of the system. For instance, crystallinity and surface morphology of the photocatalyst strongly affects the photocatalytic efficiency of the system [84, 85]. Since, EHP generation as well as separation, as well as separation, depends on both crystallinity and surface properties of the photocatalyst. Generally, highly crystalline semiconductor materials render significantly high photocatalytic activity. Moreover, highly crystalline photocatalyst owing to minimal surface defects can effectively inhibit EHP recombination sites. The reduced particle size of the photocatalyst can also increment the photoactivity due to diminished EHP diffusion length [86-88]. Furthermore, trapping of photocarriers in a shallow energy range resides near the band edge level can be utilized to enhance the lifespan of EHP as well as to enhance their spatial separation [89]. Alongside, trapping of photocarriers significantly decreases their mobility as well as energetics [90]. For example, a sample of g-C_3N_4 holds a superior concentration of trapped electrons with the high lifespan of a microsecond to second [91]. However, due to profound trapping, these electrons could barely migrate to the surface sites of photocatalyst and participate in the photocatalytic process. Thus, some other strategies for superior migration and separation of photocarriers involve shortening of transmission distance, reduced surface defects and formation of heterojunction systems. In order to shorten the transmission distance for efficient charge migration and separation, reduction in particle size of photocatalytic material can be very useful [90]. Since, the possibility of EHP reassembly is very high with the suspended NPs with lesser size than that of electron-hole diffusion lengths. Through optimal starting material and synthesis routes, the particle size of the photocatalysts can be controlled. As the NPs with appropriately smaller size provides short diffusion distance through which carriers can easily transfer to the active surface sites and play a part in the process. Although defects at surface morphology act as active reaction sites and reduce the reassembly rate of EHP. However, the presence of killer defects at the surface of photocatalytic material serves as a recombination centre which greatly affects the photoactivity [92]. For controlling the surface defects and to promote the crystallinity of g-C_3N_4, a molten salt flux strategy by utilizing the mixture of NaCl/KCl was reported [93]. The addition of a mixture of salts in the synthesis remarkably enhanced the crystallinity and inhibits the formation of defects. Such a technique can be utilized to synthesise different

520 photocatalysts (SrTiO₃, Sn₂TiO₄, Ta₃N₅ etc.) with high crystallinity and ~~less~~ fewer defects

521 [90,94,95]. Another frequently functionalized technique to suppress the reassembly of

522 photocarriers is the tailoring of heterojunction systems. Till date, the formation of Z-scheme

523 systems utilizing two or more than two semiconductor photocatalysts is greatly explored. The

524 superior mechanistic functioning of Z-scheme system facilitates the effective separation and

525 migration of photocarriers by inhibiting the reassembly of charge carriers. The systematic

526 representation of different selectivity aspects along with the criteria to achieve them is

527 represented in Fig. 6.

<Please Insert Fig. 6 Here>

529 Although, scientists have paid due attention to develop new advanced semiconductor

530 photocatalysts to harvest solar light for various photocatalytic applications. However widespread

531 applicability of photocatalytic material could be achieved if it is cost-effective and derived from

532 ~~earth~~ earth-abundant precursors. Compounds of Re, Ru, Os, Rh, Ir, Pd, Pt, Ag and Au are not

533 referred as ~~earth~~ earth-abundant as they are very costly due to the use of expensive precursors

534 which limits their applicability on a commercial scale. However, the transition ~~metal~~ metal-based

535 photocatalysts involving the compounds of Mn, Fe, Co, Ni, Mo, Cu, and W are widely explored

536 due to their ~~earth~~ earth-abundant feedstock and significant photocatalytic features. Oxides of Fe

537 for various photocatalytic applications have been heavily exploited as they are appealing

538 photocatalytic material and globally scalable [96]. Besides, abundance and cost-efficiency of

539 iron make~~s~~ it a more suitable photocatalyst for the clean energy conversion process. Other than

540 transition metals, carbonaceous materials namely graphene, and g-C₃N₄ are metal-free

541 semiconductor material obtained from ~~earth~~ earth-abundant C and N rich precursors. Moreover,

542 exceptionally high physicochemical stability and non-toxicity of g-C₃N₄ makes it more

543 favourable and broadly utilized photocatalyst.

544 Other parameters which influence the selection of photocatalytic material involve the separation

545 and recycling ability of the photocatalyst. To maintain the cost-effectiveness in photocatalysis it

546 is equally essential that a photocatalytic material can be easily separated from the reaction

547 mixture and recovered for further usage. It is a well-known fact that photocatalyst with particle

548 size less than 1 μm offers great activity and stability as it experiences significantly low attrition.

549 But the main difficulty of utilising such small particles is their separation from the reaction

18

550 mixture. Selecting a photocatalytic material with magnetically rich properties can be a useful

551 approach for the efficient separation of photocatalysts [97]. Thus, a significant advancement in

552 this area can be explored to develop more photocatalysts with high magnetic behaviour for ease

553 of separation. Other than this, immobilizing the nano-size powdered photocatalyst with a

554 supporting material can effectively improve the separation without consuming much time. Since

555 without immobilization, the chances of inefficient separation along with significant loss of

556 photocatalyst are very high [98]. For instance, powdery g-C_3N_4 nanocatalysts do not exhibit

557 magnetisation and are difficult to separate from the system. Consequently, it becomes important

558 to develop a facile technique for the efficient immobilization of g-C_3N_4 utilizing a proper

559 supporting material which avoids the costly as well as time time-consuming separation process.

560 For instance, Dong *et al*. immobilized powdery g-C_3N_4 nanocatalyst on well-arranged Al_2O_3

561 ceramic foam through the in-situ process [98]. It was observed that the optimal immobilization

562 of g-C_3N_4 on Al_2O_3 supports was effectively achieved by pyrolysis at 600 °C for about 2 h.

563 Moreover, the immobilized g-C_3N_4 photocatalyst exhibited excellent stability and recycling

564 efficiency without deactivation.

565 The difficulties arise from the applicability of photocatalyst from laboratory to pilot scale

566 applications which demand low low-cost photocatalysts which exhibit superior redox ability and

567 quantum efficiency. A more reliable mechanistic approach regarding solar light harvesting,

568 separation of photocarriers, surface redox reactions, photocatalyst-liquid interface interaction and

569 photo-reactor design should be incorporated for the widespread practical applications of the

570 photocatalyst. Noteworthy, the biggest task of comparing various photocatalytic materials

571 originates from the different reaction conditions along with variation in photocatalytic activity

572 measurement [78]. Ultimately selecting an optimal photocatalyst which exhibits superior

573 photocatalytic properties including, effectual visible light harnessing, separation/migration of

574 charge carriers, effective transmission of photocarriers to the surface and significant surface

575 adsorption capacity fulfils the basic condition in order to attain higher quantum efficiency.

576 Till date, various photocatalytic materials with significant photocatalytic activities have been

577 reported for various photoassisted activities [99-105]. Various reduction type photocatalysts like;

578 CdS, TaON, Cu_2O, Ta_3N_5, SiC, ZnS, Bi_2S_3 etc. have been successfully utilized for photo-

579 reduction of CO_2 as well as for H_2 generation (Fig. 7). Out of all these photocatalysts, graphite

graphite-like g-C₃N₄ is a most fascinating metal-free conjugated photocatalytic material due to its amazing physical as well as chemical features. The past few years have observed a g-C₃N₄-driven "gold-rush" excelling in the field of photocatalysis as an outstanding 2D metal-free conjugated polymer. Its low-cost, ~~earth~~ earth-abundant and facile synthesis involving ~~nitrogen~~ nitrogen-rich precursors like urea [106,107], melamine [108-110], thiourea [111,112] and dicyandiamide [113,114] ~~has~~ have spurred enormous interests of research groups. In case of g-C₃N₄, its CB potential locates around -1.12 V vs. NHE (pH = 0) and its VB potential locates at about 1.57 V. It is noteworthy that an oxidation photocatalyst with low VB edge position exhibits strong oxidation potential while, a reduction photocatalyst generally with high CB edge shows strong reduction ability [115]. Therefore, from the CB position of g-C₃N₄ (-1.12 V), it is evident that it is a reduction type photocatalyst with high reduction potential which is highly suitable for CO₂ reduction and water splitting through Z-scheme pathway. Since, Z-scheme charge transfer mode renders exceptionally high space charge separation efficiency and maintains considerably high redox ability of the system which is highly desired in photoconversion applications.

<Please Insert Fig. 7 Here>

5. All-Solid-State Z-scheme photocatalysts

In 2006, the ~~first~~ first-ever all-solid-state Z-scheme TiO₂-Au-Cds system was constructed via a photochemical deposition-precipitation route which involved photoreduction of Au NPs (NPs) on TiO₂ surface. The photo_reduced Au NPs act as reduction sites with CdS shell around and accelerated photocarrier's separation in ASS TiO₂-Au-CdS Z-scheme. The idea of solid electron mediator gained due attention of researchers because of the improved photocatalytic ability of an as-obtained ternary system (TiO₂-Au-CdS) than binary systems (Au-TiO₂ and TiO₂-CdS) [116]. An ASS Z-scheme photocatalytic system is fabricated without A/D pair, instead, a solid electron mediator (M) is used at the surface junction of two semiconductors which can be mentioned as SC-M-SC. By inserting a conductor (electron mediator), ~~an~~ ohmic contact with small resistance is generated at the interface [117,118]. Because of this ohmic contact, the photo-irradiated CB electrons from SC-II can recombine directly with photoinduced holes from the VB of SC-I which lowers the distance of electron migration pathway in Z-scheme. Moreover, the absence of redox mediator perfectly avoids backward reactions occurring in the ~~first~~ first-generation Z-scheme

20

system. Also, overall redox potential ability is increased as photoinduced electrons and holes in CB of SC-I and in VB of SC-II, respectively, are mostly reserved for forwarding redox reactions. Additionally, the absence of liquid-phase A/D pair in SC-M-SC systems extends its applications in both gaseous and ~~solid~~ solid-phase conditions for water splitting and photoreduction of CO_2 (Table 1). Electron mediators are comprised of redox mediators, conductors involving noble metal NPs and carbon materials which are applicable in liquid-phase Z-scheme (1st generation Z-scheme). However, redox mediators limit the ~~wide~~ wide-scale application of Z-scheme system because of backward reactions, less ~~light~~ light-harvesting and significantly poor tolerance towards pH change in photocatalytic reactions [119, 120]. In ASS Z-scheme systems, metal NPs like Au, Ag, Pt, Cu and Bi, and carbon family members; (GO, CNT, rGO, fullerene and carbon nanosheets (CNS)) are employed as solid electron mediators owing to rapid photocarriers separation as they act as electron sink [121-123]. Mediators and solid conductors act as a charge diffusion bridge in ASS Z-scheme system which endows significant isolation of photoinduced excitons. The following section will summarise ASS Z-scheme systems with different electron mediators (noble metal NPs and carbonaceous material) in photocatalysis.

5.1 Noble ~~metal~~ metal-mediated ASS photocatalysts

Inherent anticorrosive nature of noble metals with resistance to chemical action and oxidation at high temperature expand their utilization in photocatalytic applications. The prominent feature of noble metal NPs ~~is~~ in the presence of absorption bands in optical spectral range due to resonance plasmon excitation. The existence of this plasmonic resonance is complemented by a sharp increase of electric field amplitude inside and around NPs leading to plasmon-excitons. It is widely apprehended that noble metal NPs can function as traps and boosted the transfer efficacy of photocarriers [124]. Besides, noble metal NPs exhibit surface plasmon resonance (SPR) that reinforce optical absorption of bulk g-C_3N_4 and at the same time foster thermal redox ability during photocatalytic reactions [125]. Recently, a sandwich-structured ternary photocatalyst CdS/Au/g-C_3N_4 with sulphur-doping was designed by bath deposition method [126]. The incremented photocatalytic activity of resulted ternary system was governed by water splitting and dye degradation applications as compared to binary systems CdS/g-C_3N_4 and Au/g-C_3N_4. The experimental results were explained using the Z-scheme charge migration mechanism in which Au NPs acted as electron transfer mediator. ~~In order t~~To fabricate a tunable heterojunction photocatalyst CdS/Au/g-C_3N_4, Au@CdS ~~core~~ core-shell assembly was placed onto the g-C_3N_4

21

surface. The photocatalytic activity of heterojunction photocatalyst incremented about 125.8 times for hydrogen production compared to bulk g-C$_3$N$_4$ under visible light irradiation. These reports signify that a ternary photocatalyst involving both noble metal NPs and semiconductor is an effectual strategy for enhancing photocatalytic efficacy of g-C$_3$N$_4$. Moreover, synthesis procedure used to tailor ternary photocatalytic system CdS-Au-g-C$_3$N$_4$ turned out to be a major drawback since binary composite CdS-g-C$_3$N$_4$ is still found in resulting ternary composite. To surmount the aforementioned drawbacks, a more facile synthetic technique is practiced practised comprising of two-step photoreduction method.

In another work, Gao *et al.* utilized Ag metal NPs as an electron mediator and designed g-C$_3$N$_4$/Ag/LaFeO$_3$ nanocomposite through photoreduction deposition followed by hydrothermal route [127]. It was observed that the three-component ASS Z-scheme photocatalytic system exhibited exceedingly well photoactivity than those of single as well two-component system due to the SPR effect of Ag metal. The SPR effect induced by Ag metal NPs established an internal electric field in the Z-scheme system which helped in the effectual separation of photocarriers. The presence of Ag metal NPs in the microstructure of g-C$_3$N$_4$/Ag/LaFeO$_3$ nanocomposite was analysed by HR-TEM examination (Fig. 8a and b). The intact contact between g-C$_3$N$_4$ and LaFeO$_3$ was clearly visible along with deposited Ag NPs at the surface junction utilizing the scale of about 10 nm. Other than HR-TEM, XPS spectra were also observed to investigate the presence of Ag NPs in the Z-scheme heterojunction system. The XPS spectral studies indicated the presence of all the respective elements present in g-C$_3$N$_4$/Ag/LaFeO$_3$ ASS system along with their orbitals. Moreover, the Ag 3d spectra displayed the presence of both photos reduced Ag$^+$ (with corresponding peaks at 368.2 eV and 374.2 eV) and Ag (with corresponding peaks at 367.6 eV and 373.5 eV). The effectiveness of charge migration and isolation was scrutinized *via* EIS (Fig. 8c) and photoinduced fluorescence spectroscopy (Fig. 8d) which demonstrated significantly deprived recombination rate of photocarriers in ternary g-C$_3$N$_4$/Ag/LaFeO$_3$ ASS system as compared with pristine and binary heterostructures. Consequently, the ASS Z-scheme heterojunction systems having noble-metal NPs as electron mediator remarkably boost the photocatalytic efficiency by effectively broadening the visible light response range along with increment in photocarriers migration and separation.

\<Please Insert Fig. 8 Here\>

22

Pt as noble metal NPs ~~have~~ has been vastly utilised as one of the most effectual cocatalysts in ~~water~~ water-splitting reactions owing to its unique features which can modulate the selectivity and activity of a photoreaction depending upon its size [102]. Besides, the electron sink (acceptor/donor) ability of Pt NPs also facilitates its utilisation as electron transmission mediator in Z-scheme photocatalysis. For instance, Wang *et al*. reported Pt noble metal NPs as electron transmission bridge between PCN and TiO_2@C fabricated through impregnation followed by calcination (Fig. 9a) which facilitated electron migration from macroporous ~~carbon~~ carbon-coated TiO_2 (TiO_2@C)$\rightarrow$Pt$\rightarrow$g-C_3N_4 [128]. Formation of ASS Z-scheme photocatalyst rendered effectual space charge separation which boosted photocatalytic CO_2 reduction into CH_4 with a rate of 6.56 $\mu molh^{-1}$ and quantum efficacy 5.67%. Improved charge carrier separation kinetics favoured by ASS heterostructure system was confirmed by intense transient photocurrent responses and decreased Photoluminescence (PL) peak intensity of as-synthesised DOM-CNPTC nanocomposite. Fig. 9b depicts photocurrent responses of various samples which suggested superior charge migration kinetics in 3DOM-CNPTC nanocomposite with highest photocurrent responses. In another work, charge carrier kinetics of a narrow band semiconductor material Cu_2ZnSnS_4 (CZTC) was improved by forming its Z-scheme heterostructure with g-C_3N_4 through Pt as electron migration bridge [129]. Through LSV curves (Fig. 9c), the slight increase in current density under light illumination was observed which signified extended absorption in visible light leading to amended electronic features due to the involvement of Pt and CZTS. Surface plasmonic resonance along with electron sink property of Pt synergistically boosted opto~~-~~electronic features of as-resulted CZTS@Pt/g-C_3N_4 nanocomposite. The photocatalytic ability of CZTS@Pt/g-C_3N_4 ASS Z-scheme system was evaluated for photocatalytic CO_2 conversion into CO and CH_4 with average yields of 17.351 and 7.961 $\mu molg^{-1}h^{-1}$ which was about 3.31 and 5.56 times higher than bare g-C_3N_4. The mechanistic insight representing potentials and pathway of effectual photocatalytic CO_2 reduction *via* more feasible Z-scheme mode over conventional type-I mode is depicted in Fig. 9d.

Summarily, combining two semiconductor photocatalysts with a noble metal NP as electron mediator serves as a great for amended visible light harnessing and space charge isolation of photoinduced excitons. As a result, the photoreaction kinetics of photocatalytic system gets significantly improved owing to the presence of abundant charge carriers at the surface of photocatalyst which can participate in photo-redox reactions. However, ~~in spite of~~ of~~despite~~ such

703 fascinating features, certain inherent drawbacks of noble metal NPs limit the ~~wide~~ wide-scale

704 applicability of them in photocatalysis.

5.2 Carbon mediated ASS photocatalysts

708 ~~Low~~ Low-cost carbon materials also serve as electron mediators in ASS Z-scheme photocatalysts

709 since noble metals are expensive, photo-corrosive, and their recovery from solution is time-

710 consuming. ~~Carbon~~ Carbon-based materials have more active surface sites and can act as good

711 sink and transporters of electrons [130]. Besides, the photostability of these materials under

712 varying reaction conditions imparts exceptionally high reusability which boosts their

713 performance as a catalyst for various solar energy conversion applications. For instance, in a

714 fascinating work, Hu *et al*. represented the dual role of RGO as electron transmission bridge and

715 binder in g-C_3N_4/BiOI/RGO ASS Z-scheme heterojunction system immobilized on Ni foam for

716 efficient photocatalytic CO_2 reduction [131]. The enhancement in photoefficacy of the Z-scheme

717 system was ascribed by effectual isolation and space separation of charge carriers owing to the

718 incorporation of RGO as electron mediator and substantial difference in work functions of g-

719 C_3N_4, BiOi and RGO which facilitated the migration of electrons from CB of g-C_3N_4 to VB of

720 BiOI *via* RGO. The unique and significant role of carbonaceous material as electron sink and

721 transfer medium not only foster electron migration but also improve the availability of excitons

722 of photo-induced surface reactions leading to excellent photoactivity. 0D carbon dots (CD) are

723 also facilely utilised as an electron mediator in a Z-scheme assembly of $NiFe_2O_4$ (NFO)/g-C_3N_4

724 (CN) fabricated through a simple wet chemical method [132]. Incorporation of 0D CD aided to

725 convert a type-II heterojunction into Z-scheme system with CD as electron donor/acceptor

726 moiety. The improved charge carrier separation efficacy of ASS Z-scheme NFO/CN/CD

727 nanoheterostructure was analysed with PL spectroscopic analysis which showed significantly

728 decreased PL intensity of the nanocomposite as compared to bare samples.

729 In a similar study, nanocarbon (C) as solid electron mediator in ASS g-C_3N_4/$ZnIn_2S_4$ (ZIS) Z-

730 scheme photocatalytic system was reported [133]. The photoactivity of the as-tailored system

731 was assessed by H_2 production through water splitting. Moreover, the synergic effect of g-C_3N_4

732 coupled with nanocarbon coated ZIS boosted the photocatalytic H_2 generation due to the unique

733 visible light harnessing as well as conducting ability of graphic phase nanocarbon. Due to the

24

734 conducting behaviour of nanocarbon present at the interface of g-C$_3$N$_4$ and ZIS, the transference

735 of electrons and holes was significantly improved. SEM and TEM analysis ~~were~~ was utilized to

736 examine the microstructure and composition of the as-synthesised g-C$_3$N$_4$/C/ZIS system as

737 depicted in Fig. 10a-c. From HR-TEM analysis (Fig. 10c) the lattice spacing of 0.328 nm and

738 0.321 nm corresponded to (002) plane of g-C$_3$N$_4$ and (102) plane of hexagonal ZIS, respectively

739 were observed. While the ~~solid~~ solid-state nanocarbon electron mediator having deprived

740 crystallinity did not show any clear lattice fringes. To further explore the presence of nanocarbon

741 in the tailored g-C$_3$N$_4$/C/ZIS nanocomposite, thermogravimetric (TG) analysis were performed

742 as shown in Fig. 10d and e. With increasing temperature range (400-602 °C) gradual decrease in

743 the weight of g-C$_3$N$_4$/C/ZIS ASS Z-scheme system was observed suggesting the ignition of

744 nanocarbon at this temperature. Furthermore, Raman spectrum displayed two apparent peaks at

745 1375 and 1523 cm^{-1} which were ascribed to disordered (D) band and graphitic (G) band of

746 carbon, respectively, and confirmed the presence of graphic carbon in the nanocomposite Fig.

747 10f.

748

<Please Insert Fig. 10 Here>

750 Thus, solid-state electron mediator in the ASS Z-scheme systems can efficiently promote the

751 migration of photocarriers and boost the photocatalytic performance by causing spatially

752 separated charge carriers to induce photo-redox reactions at different semiconductors. However,

753 using solid-state electron mediator as a transmission bridge between two semiconductor

754 photocatalysts accompany several adverse effects on the overall photocatalytic efficacy which

755 are summarized as below;

756 (i) Use of coloured material in the electron transference process affects the effectual

757 harnessing of visible light.

758 (ii) Costly noble metal NPs are not only rare but also obstruct the visible light absorption

759 due to their tendency to act as a strong absorber.

760 (iii) The presence of photocorrosive noble metals substantially limits the photocatalytic

761 activity over varying pH range.

762 (iv) The transmission distance of electrons from one semiconductor to another is

763 significantly large due to the presence of solid electron mediator.

25

764 Therefore, it became necessary to tailor a photocatalytic system which not only avoids the use of

765 electron mediators but also offers significant photocatalytic ability under different reaction

766 conditions. The latest third generation of Z-scheme i.e. direct Z-scheme photocatalytic systems

767 seem to be an effective approach to overcome all the drawback associated with ASS Z-scheme

768 and provide appropriate redox potential for H_2 generation as well as for CO_2 reduction.

769

6. Direct Z-scheme photocatalysts

771 Direct Z-Scheme scheme nanohybrids were primarily introduced in 2013 which comprised of

772 two semiconductor photocatalysts forming a compact surface junction and neglecting the

773 requirement of Transmission Bridge for migration of electrons [134-136]. In comparison with

774 traditional Z-scheme (generation I with redox mediator), direct Z-scheme system conquer

775 backward reactions due to absence of redox mediators. Moreover, the shielding effect produced

776 by charge carrier mediators (A/D pairs) is also effectively reduced. Furthermore, in contrast with

777 ASS Z-scheme systems involving solid electron mediator, there is are no expensive and photo-

778 corrosive metals included in direct Z-scheme system. In addition, the transmission distance for

779 electron transfer gets remarkably decreased due to the absence of electron migration bridge

780 formed by solid-state mediators. Although the structure of both type-II and direct Z-Scheme

781 scheme system is similar yet their charge transfer mechanism is totally different as ascertain by

782 various characterization methods [137, 138]. As mentioned before, in direct Z-scheme system

783 the spatial separation of EHP follows inter cross-sectional electron transfer mechanism

784 stimulated by the induced electric field at the interfacial junction, totally different from

785 conventional heterojunction photocatalysts. Both semiconductors (SC-I and SC-II) under visible

786 light illumination, generates EHP which undergo inter-cross cross-sectional electron transfer via

787 transference of e_{CB}^- present in SC-II to VB of SC-I and combines with holes. Eventually, e_{CB}^- on

788 SC-I and h_{VB}^+ of SC-II are spatially separated with high redox potential values than the potential

789 for radical's production (-0.33 V and +2.4 V *vs*. NHE for $\bullet O_2^-$ and $\bullet OH$ radicals, respectively).

790 Also, through direct Z-scheme migration pathway of photogenerated EHP, the photon shielding

791 problem induced due to redox mediators is effectively overcome resulting in higher absorption of

792 visible light by semiconductor photocatalysts.

26

For instance, Low *et al*. smartly designed reusable TiO_2/CdS direct Z-scheme heterojunction system and evaluate its potential for photoassisted CO_2 reduction into methane [139]. The formation of an intact surface junction between TiO_2 and CdS as a result of direct Z-scheme coupling was investigated with in-situ irradiated X-ray photoelectron spectroscopy (ISI-XPS) as shown in Fig. 11a and b. Precisely, after the exposure of light, the slight positive shift in binding energy (by 0.3 eV) of Ti 2p peaks were observed owing to decreased electron density. Besides, under the same conditions, Cd 3d peaks exhibited negative shift by -0.2 eV due to increased electron density on CdS. These in-situ results depicted significant transference of electrons from TiO_2 to CdS under visible light illumination suggesting the formation of direct Z-scheme system instead of conventional type-II heterojunction. Such in-situ experimental observations provide an effective insight into the mechanistic pathway of charge carrier's migration and separation. In another study, a novel Z-scheme 2D/2D $MnIn_2S_4/g\text{-}C_3N_4$ (MnISCN) nanocomposite was prepared by hydrothermal route followed by in-situ loading of $MnIn_2S_4$ (MnIS) nanoflakes on g-C_3N_4 (CN) nanosheets [140]. Photoactivity of the system was assessed for TC degradation and H_2 production. X-ray diffraction (XRD) study supported the formation of an intact phase structure of MnISCN-20 system providing excellent constancy and durability of MnISCN nanocomposite. Furthermore, H_2 evolution ability of obtained photocatalyst was determined under visible light irradiation in an aqueous solution containing 0.25 M Na_2SO_3 and 0.35 M Na_2S. Bare CN and MnIS exhibited weak photocatalytic activity for H_2 generation with an average efficacy of 24.5 $\mu mol\ g^{-1}\ h^{-1}$ and 58.3 $\mu mol\ g^{-1}\ h^{-1}$, respectively. Besides, MnISCN-20 photocatalyst displayed substantial photocatalytic efficiency of 200.8 $\mu mol\ g^{-1}\ h^{-1}$ which was about 3.5 times more than MnIS nanoflakes. The UV-Vis DRS results displayed that valance band maximum (VBM) of CN nanosheets and MnIS nanoflakes were at 2.35 eV and 1.15 eV, respectively. While, conduction band minimum (CBM) for CN nanosheets and MnIS nanoflakes were calculated to be at -0.58 eV and -0.74 eV, respectively. Thus, the narrow-band gaps of both the photocatalysts facilitate visible light absorption leading to band-to-band transition of photocarriers. It was found that production of •OH radical was not feasible due to more negative VB edge (+1.15 eV vs. NHE) of MnIS than the standard redox potential of •OH/H_2O (+1.99 eV vs. NHE), moreover, CB edge value of CN (-0.58 eV vs. NHE) was more positive as compared to standard potentials of O_2/H_2O_2 (-0.695 eV vs. NHE). Hence, Z-scheme charge transfer mechanism was framed in which the photoexcited electrons get migrated from CB of CN to VB

27

824 of MnIS generating photoexcited EHP with enhanced redox abilities to produce •OH radicals as

825 shown in (Fig. 11d). ~~Evidently, t~~Typical double transfer mechanism (Fig. 11c) is excluded which

826 is in accordance ~~to~~ with PL, ESR and trapping experiments. Thus, with the formation of the

827 intact surface junction, direct Z-scheme heterojunction system endows superior optoelectronic

828 properties which are in agreement with assorted characterisation techniques.

829 Other than binary nanocomposites, g-C_3N_4 based ternary novel Z-scheme heterojunction g-

830 C_3N_4/MoS_2/Ag_3PO_4 (CMA) was successfully designed for O_2 evolution under white light

831 illumination [141]. By exfoliation, highly conductive 2D MoS_2 nanoflakes and altered g-C_3N_4

832 nanosheets were concurrently coupled with Ag_3PO_4 (silver orthophosphate) resulting in a ternary

833 direct Z-scheme CMA heterojunction system for enhanced O_2 production through OWS. The

834 CMA composites with distinct MoS_2 amount showed significant variation in photocatalytic

835 performances. Out of all the prepared CMA composites, CMA-20 composite (CMA composite

836 with 20 mg MoS_2 loading) attributed best photocatalytic water oxidation efficacy. SEM analysis

837 illustrated that large amounts of ECN nanosheets and MoS_2 were dispersed over uniform Ag_3PO_4

838 particles. From DRS plots, the band–gap of MoS_2 nanosheets was determined to be 1.72 eV.

839 Furthermore, CB and VB edge potential were estimated to be at -0.1 V and 1.71 V, respectively.

840 Based on these potential values, the photocarriers migration pathway was direct Z-scheme as

841 illustrated in (Fig. 11e). Under simulated visible light illumination, photoexcited CB electrons in

842 Ag_3PO_4 get transmitted to VB of MoS_2 and combines with photogenerated holes. Besides, photo-

843 induced CB electrons in MoS_2 migrated and combined with VB holes of g-C_3N_4, leaving behind

844 active holes in Ag_3PO_4 along with electrons in CB of g-C_3N_4 for effective photo-illuminated

845 water splitting. In CMA nanocomposite, the presences of highly conductive MoS_2, exceptionally

846 boost the photocarriers transfer efficacy by suppressing photogenerated EHP.

847 **<Please Insert Fig. 11 Here>**

848 Summarily, tailoring direct Z-scheme photocatalytic system with appropriate semiconductor

849 photocatalysts is an effective strategy to overcome various environmental and energy issues.

850 Since~~,~~ direct Z-scheme photocatalytic systems hold great potential for superior migration and

851 separation of photocarriers while maintaining the apt redox ability of the system. However,

852 several challenges involving effectual solar light harvesting, high physicochemical stability, the

853   formation of intact surface junction and utilization of proper characterization techniques ~~in order~~

854   to investigate the charge migration pathways still needs improvement. Nevertheless, with

855   breakthrough discoveries and an ever-growing number of publications in this area, it is evident

856   that direct Z-scheme systems fan the flame in photocatalytic water splitting as well as CO_2

857   reduction applications.

7. Applications of Z-scheme photocatalytic systems

7.1 Photocatalytic CO_2 reduction

860   As the efforts of researchers on photoassisted CO_2 reduction increases, new directions and

861   tendencies emerge~~s~~. Recent reports display certain common perspectives of designing and

862   tailoring Z-scheme photocatalytic systems in order to stimulate high photo to functional energy

863   conversion efficacy with high product selectivity. Since~~,~~ photocatalytic Z-scheme setup involves

864   two different semiconductor materials to bring about dual excitation after visible light exposure

865   and efficaciously separate photocarriers. Thus, photocatalytic CO_2 reduction into useful fuels

866   utilizing Z-scheme photocatalytic systems seems ~~as~~ like a beneficial technique for

867   contemporaneous environmental remediation and ~~partly~~ partial fulfilment of energy requirements

868   [142-149]. However, designing of Z-scheme photosystems with utmost selectivity of products in

869   case of CO_2 reduction is very crucial. For instance, Jo *et al*. rationally tailored Bi_2WO_6/RGO/g-

870   C_3N_4 (BWO/RGO/CN) nanocomposite for photoassisted CO_2 reduction into CO and CH_4 [150].

871   The as-tailored ASS Z-scheme photocatalyst containing 15 wt% BWO and 1 wt% RGO

872   displayed remarkable efficiency in the photoreduction of CO_2 with notable selectivity of 92%

873   against H_2 production. The unique assembly of 2D photocatalytic materials along with the dual

874   role of RGO (electron capture and redox mediator) in ASS Z-scheme system played a leading

875   role in photoactivity enhancement. To scrutinize the CO_2 reduction efficiency of the

876   aforementioned system, experiments utilizing pristine ~~as well as binary samples of~~ BRC-15 PM

877   ~~(a mixture containing RGO- 1 wt%, CN and BWO- 15 wt%) and commercial P25 catalyst~~, as

878   well as binary samples of BRC-15 PM (a mixture containing RGO- 1 wt%, CN and BWO- 15

879   wt%) and commercial P25 catalyst, were performed as depicted in Fig. 12a. ~~Clearly,~~

880   BWO/RGO/CN ASS Z-scheme system exhibited superior photoreduction efficiency which was

881   ascribed to the synergistic effect between 2D components of the heterojunction. Besides, the

882   photocatalytic system also showed improved H_2 evolution with 185 µmol quantum yield which

883 was far better than pristine and binary samples. Furthermore, to investigate the effectiveness of

884 space charge separation ~~as well as the dual functionality of RGO, transient photocurrent analysis,~~

885 as well as the dual functionality of RGO, transient photocurrent analysis, was utilized. From Fig.

886 12b the photocurrent responses of different photocatalysts during five on-off cycles of

887 intermittent light exposure can be seen. ~~Evidently, a~~ All the BWO/RGO/CN nanocomposites

888 exhibited better photocurrent responses in contrast with other photocatalysts suggesting a

889 superior separation of photocarriers in the composite. Notably, the photocurrent results were well

890 consistent with the PL as well as photocatalytic analysis. The proposed Z-scheme charge transfer

891 mechanism of BWO/RGO/CN for photoassisted CO_2 reduction is depicted in Fig. 12c. Through

892 Z-scheme charge transfer mode containing RGO as the transmission bridge, the photoinduced

893 holes were accumulated on VB of BWO while the photoexcited electrons were collected at CB

894 of CN. As a result, the VB holes of BWO reacted with water to produce O_2 and protons while the

895 CB electrons of CN after returning to RGO interacted with adsorbed CO_2 to produce $CO_2 \cdot^-$

896 radicals which in turn generated CO, CH_4 and H_2. Moreover, due to synergistic effect of BWO,

897 RGO and CN in the photocatalytic system the reassembly of photocarriers was drastically

898 decreased resulted in increased electron density on the system which effectively facilitated the

899 formation of CH_4 and CO.

900 **<Please Insert Fig. 12 Here>**

901 Till date, various photocatalytic systems utilizing photosensitive AgCl in Z-scheme

902 photocatalysts have been explored due to their unique property of switching from Ag^+ to metal

903 Ag^0 which facilitate the space isolation of photocarriers. Besides, due to appropriate band edge

904 positioning of AgCl (E_{VB} = 3.19 eV and E_{CB} = -0.05 eV), it can be coupled with reductive g-

905 C_3N_4 photocatalyst in Z-scheme mode to stimulate the photoassisted reduction of CO_2. Keeping

906 that in mind, Murugesan *et al.* tailored a novel direct Z-scheme AgCl@g-C_3N_4 nanohybrid by

907 loading different AgCl ratios on g-C_3N_4 through improved deposition-precipitation synthesis

908 route [151]. Remarkably, the wide band–gap of AgCl (3.26 eV) obstructed visible light

909 absorption but localised SPR effect in Ag^0 facilitated absorption of light leading to the generation

910 of photocarriers. Also, PL studies supported the heterojunction formation between AgCl and g-

911 C_3N_4 resulting in suppressed recombination of photoinduced EHP. Notably, the PL emission

912 intensity of aforementioned photocatalytic system decreased with the presence of AgCl in the

913 composite suggesting the formation of intact surface junction which effectively inhibited the

914 reassembly of EHP. Detailed synthesis and charge migration route ~~is~~ are explicated in (Fig. 13).

915 Proposed Z-scheme mechanism of 1%AgCl@g-C$_3$N$_4$ elucidated that accumulated

916 photogenerated electrons on AgCl surface combine directly with VB holes of g-C$_3$N$_4$ suppressing

917 EHP recombination. Further, photo-illuminated CB electrons of g-C$_3$N$_4$ owing sufficient

918 potential can reduce CO$_2$ into methane, acetic acid and formic acid as confirmed through gas

919 chromatography analysis. The mechanistic reactions involving the photoreduction of CO$_2$ is as

920 follows:

921

$$CO_2 + 8H^+ + 8e^- \rightarrow CH_4 + 2H_2O \qquad E_0 = -0.24\ \text{V vs. NHE} \qquad (20)$$

$$2CO_2 + 8H^+ + 8e^- \rightarrow CH_3COOH + 2H_2O \qquad E_0 = -0.31\text{V vs. NHE} \qquad (21)$$

$$CO_2 + 2H^+ + 2e^- \rightarrow HCOOH \qquad E_0 = -0.58\ \text{V vs. NHE} \qquad (22)$$

925

926 **<Please Insert Fig. 13 Here>**

927
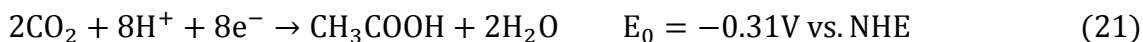
928 Thus, the unique combination of semiconductors with complimentary band edge positioning to

929 extend visible light absorption and to improve the redox ability of photocatalytic systems *via*

930 efficient charge isolation can substantially enhance the photoreduction efficacy of CO$_2$.

931 In another study, Xu and his peer group designed a ternary Ag$_2$CrO$_4$/g-C$_3$N$_4$/GO nanocomposite

932 (CAG) using a photosensitizer (Ag$_2$CrO$_4$) and a cocatalyst (GO) for CO$_2$ reduction into CH$_3$OH

933 and CH$_4$ [152]. Less particle size of Ag$_2$CrO$_4$ facilitated its combination with N-H groups

934 present on the wrinkled g-C$_3$N$_4$ surface *via* co-ordination bond. As a result, the strong junction

935 was established between g-C$_3$N$_4$ and Ag$_2$CrO$_4$ which in turn boosted space separation of

936 photocarriers. The as-synthesised CAG photocatalyst displayed improved photocatalytic

937 efficiency for CO$_2$ conversion with 0.30 h^{-1} turnover frequency (2.3 ×~ g-C$_3$N$_4$). Similar band

938 structure along with suitable loading ratio of Ag$_2$CrO$_4$ helped to construct direct Z-scheme

939 heterojunction stimulated by an internal electric field (IEF) across Ag$_2$CrO$_4$/g-C$_3$N$_4$ junction

940 resulting in CO$_2$ adsorption and subsequent reduction (Fig. 14a). Also, the addition of GO as

941 cocatalyst endorsed charge transfer along with plentiful adsorption and catalytic sites for CO$_2$.

942 Since, the 2D porous network structure of GO containing –COOH and –OH groups stimulated

943 the transportation as well as binding of CO$_2$ molecules. To investigate the effectiveness of charge

944 migration and separation through Z-scheme mode, fluorescent spectroscopy along with

945 photocurrent measurements were carried out. ~~Evidently, t~~The ternary composite displayed

946 weakest PL emission intensity which was attributed to the exceptional electron sink behaviour of

947 GO resulted in inhibited direct recombination of photocarriers. Besides, the photocurrent

948 analysis of ternary CAG photocatalyst also indicated the efficacious charge separation in the

949 sample by showing the highest photocurrent response than that of pristine and binary samples~~-~~.

950 Upon visible light illumination and under the effect of IEF, CB electrons of Ag_2CrO_4 combined

951 with photoinduced VB holes of $g\text{-}C_3N_4$ with an accumulation of electrons and holes in CB of $g\text{-}$

952 C_3N_4 and VB of Ag_2CrO_4, respectively. Photoinduced CB electrons of $g\text{-}C_3N_4$ with sufficient

953 potential reduced CO_2 into functional fuels like CH_3OH and CH_4 whilst, photogenerated VB

954 holes of Ag_2CrO_4 reacted with water to produce O_2. Besides, lower GO potential (-0.49 V vs.

955 NHE, pH = 7) than $g\text{-}C_3N_4$ was a thermodynamically favourable condition for migration of CB

956 electrons of $g\text{-}C_3N_4$ onto the conductive network surface of GO. Thereby, CAG ternary

957 nanocomposite displayed improved photocatalytic CO_2 conversion efficiency because of the

958 effective synergetic outcome of Ag_2CrO_4, $g\text{-}C_3N_4$ and GO. Thus, it is quite evident that by

959 combining plasmonic semiconductor photocatalyst with carbonaceous electron sink materials

960 synergy between extended light absorption and charge separation can be achieved leading to

961 boosted photocatalytic efficacy.

962 It has been widely reported that the transition metal oxides with broad~~-~~band edge positioning

963 contain~~s~~ partly filled d-orbitals which extend the absorption of light in the visible region due to

964 d-d transitions [153]. Typically, MnO_2 with partly filled d-orbitals is a prominent transition metal

965 oxide semiconductor photocatalyst having fascinating features like economic, abundance,

966 superior physicochemical stability and environmental friendly. Moreover, due to the multiple

967 valances of MnO_2, it can act as a semiconductor photocatalyst which can effectively enhance the

968 visible light absorption as well as photoactivity after coupling with reductive $g\text{-}C_3N_4$. For

969 example, Wang *at el.* designed $MnO_2/g\text{-}C_3N_4$ nanocomposite *via* facile in-situ oxidation-

970 reduction reaction comprising $KMnO_4$ and $MnSO_4.H_2O$ absorbed on the $g\text{-}C_3N_4$ surface [154].

971 The as-obtained enhanced CO_2 reduction efficacy was accredited to synergetic catalytic effect

972 developed during heterojunction construction between MnO_2 and $g\text{-}C_3N_4$. Moreover, the

973 interface bonding between Mn^{2+} and ubiquitously present NH_2 functional groups on $g\text{-}C_3N_4$

974 surface boosted the spatial separation of photocarriers. Also, through ohmic contact developed at

975 the interface, the photogenerated CB electrons of MnO_2 shifted to the VB of $g\text{-}C_3N_4$ (Fig. 14b)

32

976 provided effective space charge separation. Besides, CB electrons of g-C₃N₄ reacted with 977 absorbed CO_2 under the influence of protons to generate CO and H_2O. To further elucidate the 978 charge migration and effective separation, electrochemical impedance spectroscopy (EIS) as well 979 as photocurrent responses, as well as photocurrent responses, were examined. It was observed 980 that the MnO_2/g-C₃N₄ nanohybrid exhibited exceedingly enhanced photocurrent density in 981 contrast with bare g-C₃N₄ indicated highly suppressed reassembly and effective separation of 982 EHP. Thus, the notable features like: matched band alignments, improved visible light 983 harvesting and synergistic interactions between MnO_2 and g-C₃N₄ due to solid C-O bonding at 984 the surface junction substantially incremented the photoassisted conversion of CO_2 into CO.

985 As a whole, a large number of semiconductor photocatalysts have been developed lately in order 986 to get the optimal photocatalytic CO_2 conversion efficiency. However, with the present scenario 987 of photocatalytic materials and photo-efficiency, the photoassisted reduction of CO_2 cannot be 988 implemented on an industrial scale. The improved results obtained from Z-scheme photocatalysis 989 involving fascinating reductive type g-C₃N₄ semiconductor seems to be a good approach to attain 990 widespread applications. However, the selection of adjoining semiconductor photocatalyst, 991 design of photoreactor and selective reduction of CO_2 into functional hydrocarbon fuels still 992 require more attention by researchers.

993 **<Please Insert Fig. 14 Here>**

994

995 *7.2 Photocatalytic water splitting*

996 Photocatalytic water splitting is vital in order to meet desirable energy source, without reckoning 997 on fossil reserves [155-163]. However, even after breakthrough discoveries in photocatalysis, H_2 998 generation through photoassisted water splitting utilizing semiconductor materials is still far 999 from the reach of pilot pilot-scale applications. In order to improve the visible light harnessing 1000 along with resultant photo_efficiency a number of several strategies involving texture 1001 engineering, bandgap modifications, incorporation of co-catalyst and so on, have been 1002 developed. So far, mimicking natural photosynthesis to form artificial Z-scheme photocatalysis 1003 empowers efficient solar energy utilization for photocatalytic H_2 generation through water 1004 splitting. In that regard, metal-free 2D reductive type g-C₃N₄ promptly becomes a promising 1005 candidate for photocatalytic H_2 generation due to its exceptional physicochemical features. 1006 Hybridising g-C₃N₄ with another metal-free semiconductor photocatalyst to form a Z-scheme

33

heterojunction system can effectively impart high photocarriers separation efficacy along with superior redox ability to enhance the overall photoactivity.   For example, innovative work by Wang *et al.* anticipated two ~~metal~~ metal-free C$_3$N/g-C$_3$N$_4$ nanocomposites in which g-C$_3$N$_4$ sheet (single layer/bilayer) was concealed with monolayer C$_3$N [164]. Investigations revealed that the band bending caused by strong internal electric fields at the respective interface region of photocatalysts facilitate the migration of photocarriers through Z-scheme rather than type-II route. A proposed direct Z-scheme mechanism for OWS (Fig. 14c) explicates photoexcited CB electrons of C$_3$N monolayer possess sufficient potential for HER while VB holes of g-C$_3$N$_4$ are used to oxidise H$_2$O into O$_2$. From experimental results, it was observed that due to migration of photoinduced electrons from C$_3$N to monolayer or bilayer g-C$_3$N$_4$ sheet, strongly ~~built~~ built-in electric field was induced which caused band bending in C$_3$N and g-C$_3$N$_4$ sheets upward and downward, respectively. Consequently, the CB edge potential of C$_3$N monolayer and VB edge of g-C$_3$N$_4$ in the nanocomposite were suitable enough with the photocatalytic water redox potentials. Moreover, the synergistic effect induced due to coupling of two ~~metal~~ metal-free 2D materials facilitated the harnessing of visible light from visible to NIR region.

The concept of hydrogen evolution through water decomposition using Z-scheme photocatalysis is a ground—breaking strategy for the sustainable and eco-friendly method for energy development [165-174]. However, the key concern of tailoring a Z-scheme photocatalytic system involves the semiconductor photocatalysts with well-matched band alignments best suited for water redox potentials. Coupling g-C$_3$N$_4$ with TiO$_2$ serves as a great deal since, there band edge positions match well together. Besides, the involvement of Au NPs as a solid electron mediator with dual functionality to act as a photosensitizer as well as their ability of SPR effect can significantly boost the photocatalytic H$_2$ generation. ~~Best~~ The best example in this regard is the work by Zou *et al.* who engineered g-C$_3$N$_4$/Au/C-TiO$_2$ hollow spheres as ASS Z-scheme photocatalyst with Au NPs as solid-state electron mediator [175]. Upon solar light illumination, incremented photocatalytic efficacy of g-C$_3$N$_4$/Au/C-TiO$_2$ nanocomposite was evaluated for H$_2$ production. It was reported that incorporation of Au NPs as electron mediator facilitated the absorption of light in visible range due to SPR effect. From HR-TEM experiments, presence of Au NPs in the heterojunction system was evaluated where the lattice fringes with d-spacing of 0.35 nm ((001) facet of anatase TiO$_2$) and 0.24 nm ((111) facet of Au) were observed. On the other hand, C-doping introduced a mid-gap state near the VB of TiO$_2$ extending light absorption

34

to longer wavelength. PL studies indicated that •OH radicals were the leading ROS for photocatalytic H_2 evolution which is possible only through the Z-scheme migration pathway. Since, through the double-charge migration route, the redox potential of the system was not sufficient enough for the generation of •OH radicals in the majority. The proposed ASS Z-scheme charge transfer mode illustrating the band alignments of g-C_3N_4, Au and C-doped TiO_2 is depicted in Fig 15a. The electrons from CB of C-TiO_2 migrated through Au NPs to VB of g-C_3N_4 and combined with holes. Simultaneously, photogenerated CB electrons in g-C_3N_4 reduced H^+ to H_2 besides VB holes of C-TiO_2 oxidized sacrificial agents into products. As a result, the aforementioned nanocomposite exhibited superior photoassisted H_2 evolution rate which was 42 and 86 times higher than that of g-C_3N_4 and C-TiO_2, respectively. Thus, efficient visible light harnessing, superior redox ability and effectual migration/separation of photocarriers through ASS g-C_3N_4/Au/C-TiO_2 nanocomposite synergistically stimulated the photocatalytic efficacy.

In summary, the reductive type g-C_3N_4 with appropriate CB and VB edge potentials is undoubtedly a fascinating semiconductor photocatalyst in Z-scheme water splitting applications. Also, the coupling of g-C_3N_4 with an appropriate photocatalyst in order to form a Z-scheme hybrid is a promising tactic to boost its photoassisted water splitting performance. Various direct Z-scheme photocatalysts with their photocatalytic abilities for H_2 generation and CO_2 reduction are ~~summarised~~ summarized in Table. 2.

\<Please Insert Fig. 15 Here\>

7.3. Other applications

Although dinitrogen (N_2) is the most abundant gas in the atmosphere, yet 'fixed' nitrogen form bioavailability for living organisms is minimal [176]. In order to fulfil these necessities, nitrogen fixation under mild conditions is essential since artificial N_2 fixation through the Haber-Bosch process involves high energy involvements. Thus, developing advanced strategies which involve green and sustainable energy sources is highly desired. Photocatalytic N_2 fixation utilizing never lasting solar energy is a green and economical technique for the conversion of N_2 into NH_3 [177, 178]. For example, Cao *et al.* described aromatic rings of 3, 4-dihydroxybenzaldehyde (DBD) as an electron mediator in Ga_2O_3/graphitic carbon nitride (Ga_2O_3-DBD/g-C_3N_4) ASS Z-scheme heterojunction for solar light assisted photocatalytic nitrogen fixation [179]. The as-tailored nanocomposites were found to exhibit high photocarriers separation efficacy, improved visible-

light absorption along with high redox capacity due to the formation of a conductive interface between Ga_2O_3-DBD and g-C_3N_4. The proposed charge migration mechanism in relevance with experimental results was Z-scheme mode with DBD rings as electron mediator instead of typical type-II as illustrated in (Fig. 15b). Spin trapping electron paramagnetic resonance (EPR) technique confirmed •CO_2^- as the main active species responsible for N_2 fixation (Fig. 15c). Moreover, the facile generation of •CO_2^- ($E_0 = 1.8V$) radicals with sufficient potential prompted the photoassisted reduction of N_2 to NH_3. The photocurrent measurements observed for 2.4% Ga_2O_3-C_3N_4 and 2.4% Ga_2O_3-DBD/g-C_3N_4 are depicted in Fig. 15d. It can be clearly seen that the photocurrent response of 2.4% Ga_2O_3-DBD/g-C_3N_4 was observed to be much higher than that of 2.4% Ga_2O_3-C_3N_4, suggesting the superior space charge separation due to the construction of Z-scheme involving DBD rings as the electron mediator. Due to Z-scheme charge migration route, high potential photogenerated CB electrons of g-C_3N_4 converted O_2 to H_2O_2 while VB holes of Ga_2O_3 with sufficient redox potential generated •OH radicals from H_2O. Furthermore, •OH radicals reacted with CH_3OH to produce •CO_2^- which facilitated the reduction of N_2 to NH_3.

<Please Insert Fig. 15 Here>

In another work, Liu and his team reported the facile fabrication of porous g-C_3N_4 loaded with Fe_2O_3 for the photocatalytic conversion of N_2 to ammonia [180]. Coupling g-C_3N_4 (porous) with Fe_2O_3 substantially incremented the photocatalytic N_2 reduction rate driven by artificial solar light. Of note, the g-C_3N_4/Fe_2O_3 (< 1 wt%) (GF) nanocomposite exhibited 47.9 mg/L/h rate of photocatalytic production NH_3 from N_2 reduction which was about 6 times higher than pristine g-C_3N_4. To examine the photocatalytic activities of GF composites annealed at different temperatures for the photoassisted reduction of N_2, the experiments were performed in a water system with bubbling N_2 atmosphere under the exposure of 300 W Xe lamp. And the rate of NH_3 production by different GF composites is depicted in Fig. 16a. The investigation further revealed that the GF composite annealed at 500 °C (GF-500) exhibited an exceedingly high rate of NH_3 generation (47.9 mg/L/h) which significantly decreased after an additional increase in annealing temperature, suggesting the importance of Fe_2O_3 in the composite. Moreover, the photocurrent responses also suggested that the GF composites exhibited higher photocurrent intensity due to the effectual separation of photocarriers (Fig. 16b). The GF-500 composite displayed photocurrent intensity of 4.5×10^{-6} A which was much higher than that of g-C_3N_4 (1.0×10^{-6} A).

1100 Furthermore, the possible Z-scheme charge transfer pathway is depicted in Fig. 16c. Because of
1101 suitable band edge positioning, the photo-excited CB electrons of Fe_2O_3 rapidly combine with
1102 VB holes of g-C_3N_4 and form a Z-scheme system. Due to Z-scheme charge transfer mode,
1103 effectual space charge separation was attained resulted in well well-maintained redox abilities
1104 suitable for photocatalytic N_2 reduction.

<Please Insert Fig. 16 Here>

1106 Other than energy conversion applications, photocatalysis is in constant limelight for
1107 environmental remediation involving biotic and abiotic pollutant degradation, noxious gases
1108 removal and harmful electromagnetic waves absorber [181-185]. Thus, with consistent research
1109 efforts in the field of photocatalysis, more efficient semiconductor materials with high stability,
1110 recyclability, non-toxicity and extended visible spectral response can be designed with critical
1111 significance in both theory and practice.

1112

8. Conclusion and viewpoint

1114 The discussion in the present review highlights the photoassisted energy conversion applications
1115 that could provide a light of hope to overcome the energy issues rising globally. Selecting an
1116 appropriate photocatalytic material which fulfils all the imperative criteria is of utmost concern.
1117 Architecting visible light stimulated Z-scheme photocatalysts is in rife attention by dint of its
1118 great potential in various photocatalytic applications that aids to serve as a promising aspirant for
1119 solar light harvesting and environmental restoration. As explained in a review of literature,
1120 fascinating properties of reductive type g-C_3N_4 like its tunable electronic structure and first-rate
1121 physicochemical stability complements its coupling with other semiconductor materials with
1122 appropriate band potentials in order to achieve improved photoactivity. This review encircles far-
1123 reaching aspects of recent research work on all solid state and direct Z-scheme photocatalysis
1124 inspired by artificial photosynthesis together with its captivating applications like CO_2 reduction,
1125 photocatalytic water splitting and nitrogen fixation (Fig. 17). Construction of Z-scheme
1126 photocatalysts involving reduction type photocatalysts has some characteristic qualities which
1127 extend its application in various pitches as:
1128 (1) To attain water splitting, Z-scheme system involving reduction type photocatalysts has
1129 overruled conventional double transfer system by outspreading wavelength towards NIR to offer
1130 maximum optical absorption along with improved redox ability. Furthermore, the Z-scheme

1131 photocatalytic system is capable to encompass both half-cell reactions deprived using sacrificial

1132 reagents for water splitting.

1133 (2) For photocatalytic CO_2 reduction, constructing reduction type g-C_3N_4 based Z-scheme

1134 photocatalytic system provides efficiently high redox ability. Since g-C_3N_4 is a reduction type

1135 photocatalyst moreover existence of ubiquitous -NH and -NH_2 Lewis basic groups provide

1136 effective absorption sites for CO_2 along with the generation of photocarriers for its reduction.

1137 (3) Tailoring of Z-scheme systems which include reductive photocatalysts render sufficient

1138 catalytic surface sites, improved generation of ROS and suppressed EHP recombination which

1139 boosts the overall photocatalytic efficacy.

1140 (4) Integrating g-C_3N_4 with a suitable photocatalytic material which offers SPR effect is of great

1141 potential as it extends visible light harnessing ability of Z-scheme system. As a result, the Z-

1142 scheme mode synergistically improves optical response along with charge carrier isolation

1143 efficiency.

1144 (5) Involvement of carbonaceous material as electron sink provides additional help to boost the

1145 charge carrier's kinetics and enhance the availability of electrons to participate in photo-redox

1146 reactions.

<Please Insert Fig. 17 Here>

1148 • *Current scenario*

1149 To date, Z-scheme photocatalysis is a developing strategy as it provides superior photocatalytic

1150 efficacy over traditional double charge transfer mechanism. The reason of improved

1151 photoactivity is ascribed by its ability to generate photo-illuminated charge carriers, their

1152 effective spatial separation, more catalytic surface sites, the formation of active species, a

1153 prolonged life-time of ROS and enhanced redox abilities by using two photocatalysts. However,

1154 the first and second generation of Z-scheme photocatalysis has some pitfalls which restrict their

1155 widespread applications. In detail, traditional or liquid-phase Z-scheme photocatalysts use liquid

1156 state redox mediators which undergo thermodynamically favourable backward reactions

1157 resulting in low photoactivity. Moreover, in the second generation of the Z-scheme system, use

1158 of noble-metals as solid-state electron mediators not only renders visible light absorption but is

1159 also photo-corrosive which affect the photocatalytic efficiency. In ASS Z-scheme system,

1160 optimal modification in the geometrical configuration is the most desirable strategy to boost the

1161 photocatalytic performance. On the other hand, various efforts in in-band modification of direct

Z-scheme photocatalysis unleashed its inside out properties. Still, significant efforts by researchers are underway to architect more efficient systems of this type.

- *Challenges and outlook for researchers*

In Z-scheme systems, a rational assortment of photocatalytic material is protagonist among all other conditions. Choosing an appropriate semiconductor material with apt band edge potentials is of foremost importance along with some other 'nuts-and-bolts';

(1) Semiconductors with narrow band gap and sufficient redox sites are favourable for the development of Z-scheme photocatalysis as it expedites harnessing of visible light and generation of active species for various oxidation/reduction reactions.

(2) Morphological features also play an important role in active species generation as semiconductor materials with ultrathin structure accelerates the diffusion of photoinduced carriers onto the semiconductor surface and stimulates redox reactions.

(3) Alongside, fabrication of new coupled systems hinge on rational interface-engineering methodologies is an additional tactic that should be taken into account. In direct Z-scheme systems establishment of surface phase junction between two photocatalysts plays a key role in space charge separation due to induced internal electrical field. Nevertheless, it is important that the migration pathway of photocarriers and direction of built-in electric field must overlap each other in order to achieve accelerated charge separation which can be further improved by band bending through polarization.

(4) For effective forward charge transference and utilization along with suppressed reassembly, integrated co-catalyst/semiconductor systems should be rationally designed. Of note, challenging deposition of ultrathin layer precisely on the semiconductor surface without obstruction in migration of photocarriers to co-catalyst can be prevailed partially using atomic layer deposition technique.

(5) Deprived absorption of undeviating sun-light is another bottleneck along with scalability and operability of photocatalytic material for their long lifespans in forthcoming practical applications.

(6) Higher practicability of a photocatalyst is associated with its separation efficiency, thereby, semiconductor materials should be anchored on functional polymeric inorganic membranes to achieve effectual separation efficacy.

(7) Advanced characterization techniques should be implemented to understand interfacial activities of semiconductors to utilize their worth fully in photocatalytic activity.

(8) More in-situ investigation techniques should be incorporated in order to examine the charge migration pathway and the underlying reaction mechanism.

To trigger a plethora of attempts in the modification of g-C$_3$N$_4$ based Z-scheme photocatalysis, some other considerations should also be envisaged like; semiconductor material should have improved visible light response, relatively high VB edge to provide strong oxidation potential, high physicochemical endurance and surface contact should be compact. From future perspectives, the development of Z-scheme photocatalysis involving reductive photocatalysts is in need ofneeds revision as; the mechanistic charge transfer pathway on the surface of semiconductors is still blurred and should be explored more. In ASS systems fermi level positions of solid-state electron mediator and semiconductor must be precisely concerned. Furthermore, modification in band edge positioning should be exploited in order to achieve superior redox abilities. Also, factors which influence the quantum efficiency of photocarriers should be evaluated. Only a few studies have reported in-situ characterisation techniques for clarity of charge carrier migration pathway *via* Z-scheme mode. More such techniques should be involved for scrutinising charge transfer pathways through Z-scheme mechanism.

Considering our present level of knowledge and available technology, updating photocatalytic efficacy on industrial level utilizing narrow band-gap semiconductors which are lucrative and abundant still needs improvement. More development in the field of Z-scheme photocatalysis is peremptory, preferably in conjunction with innovative discoveries emanate from inclusive research areas. Thus, it is our genuine hope that putting more efforts on this research area will definitely accelerate its widespread applications.

References

[1]   K. Qi, B. Cheng, J. Yu, W. Ho, Chin. J. Catal. 38 (2017), pp. 1936–1955.

[2]   J. Yu, S. Wang, J. Low, W. Xiao, Phys. Chem. Chem. Phys. 15 (2013), pp. 16883-16890.

[3]   S.Y. Lee, S. J. Park, J. Ind. Eng. Chem. 23 (2015), pp. 1-11.

[4]   N. Chandela, S. Sharmaa, V. Duttaa, P. Raizadaa, A.H. Bandegharaeic, R. Kumar, V.K. Gupta, S. Agarwal, P. Singha, Desalin. Water Treat. (2020), pp. 1–19.

[5]   J. Hu, P. Zhang, J. Cui, W. An, L. Liu, Y. Liang, Q. Yang, H. Yang, W. Cui, J. Ind. Eng. Chem. 84 (2020), pp. 305-314.

[6]   L.S. Yoong, F.K. Chong, Binay K. Dutta, Energy 34 (2009), pp. 1652–1661.

[7]   M. Ni, M.K.H. Leung, D.Y.C. Leung, K. Sumathy, Renew. Sust. Energ. Rev. 11 (2007), pp. 401–425.

[8]   M.S. Akple, J. Low, Z. Qin, S. Wageh, A.A. Al-Ghamdi, J. Yu, S. Liu, Chin. J. Catal. 36 (2015), pp. 2127–2134.

[9]   A. Kumar, P. Raizada, P. Singh, A.H. Bandegharaei, V.K. Thakur, J. Photochem. Photobiol. A: Chem. (2020), pp. 112588.

[10]   P. Singh, K. Sharma, V. Hasija, V. Sharma, S. Sharma, P. Raizada, M. Singh, A.K. Saini, A.H. Bandegharaei, and V.K. Thakur, Mater. Today Chem. 14 (2019), pp. 100186.

[11]   X.H. Xia, Z.J. Jia, Y. Yu, Y. Liang, Z. Wang, L.L. Ma, Carbon 45 (2007), pp. 717–721.

[12]   K. Sharma, P. Raizada, A.H. Bandegharaei, P. Thakur, R. Kumar, V.K. Thakur, V.H. Nguyen, P. Singh,   Process Saf. Environ. Prot. 142 (2020), pp. 63-75.

[13]   P. Raizada, A. Sudhaik, P. Singh, A.H. Bandegharaei, V.K. Gupta, S. Agarwal, Desalination Water Treat. 171 (2019), pp. 344-355.

[14]   P. Raizada, P. Thakur, A. Sudhaik, P. Singh, V.K. Thakur, A.H. Bandegharaei, Arab. J. Chem. 13 (2020), pp. 4538-4552.

[15]   N. Chandel, K. Sharma, A. Sudhaik, P. Raizada, A.H. Bandegharaei, V.K. Thakur, P. Singh, Arab. J. Chem. 13 (2020), pp. 4324-4340.

[16]   P. Raizada, A. Sudhaik, V.P. Singh, V.K. Gupta, A.H. Bandegharaei, R. Kumar, P. Singh, Desalination Water Treat. 148 (2019), pp. 338-350.

1254 [17] P. Singh, A. Sudhaik, P. Raizada, P. Shandilya, R. Sharma, A.H. Bandegharaei, Mater.

1255 Today Chem. 12 (2019), pp. 85-95.

1256 [18] B. Priya, P. Shandilya, P. Raizada, P. Thakur, N. Singh, P. Singh, J. Mol. Catal. A:

1257 Chem. 423 (2016), pp. 400-413.

1258 [19] A.R. Sani, P. Singh, P. Raizada, E.C. Lima, I. Anastopoulos, D.A. Giannakoudakis, S.

1259 Sivamani, T.A. Dontsova, A.H. Bandegharaei, Bioresour. Technol. 297 (2020), pp.

1260 122452.

1261 [20] J. Fu, J. Yu, C. Jiang, B. Cheng, Adv. Energy Mater. 8 (2017), pp. 1701503.

1262 [21] W. Jiang, W. Luo, J. Wang, M. Zhang, Y. Zhu, J. Photochem. Photobiol. C Photochem.

1263 Rev. 28 (2016), pp. 87–115.

1264 [22] J. Low, J. Yu, M. Jaroniec, S. Wageh, A.A. Al-Ghamdi, Adv. Mater. 29 (20) (2017), pp.

1265 1601694.

1266 [23] H. Du, Y. Liu, C. C. Shen, and A. W. Xu, Chinese J. Catal. 38 (8) (2017), pp. 1295-

1267 1306.

1268 [24] P. Raizada, J. Kumari, P. Shandilya, P. Singh, Desalin. Water Treat. 79 (2017), pp. 204-

1269 213.

1270 [25] P. Thakur, P. Raizada, P. Singh, A. Kumar, A.A.P. Khan, A.M. Asiri, Arab. J. Chem.

1271 (2020), In press, https://doi.org/10.1016/j.arabjc.2020.04.026

1272 [26] A. Hezam, K. Namratha, D. Ponnamma, Q. A. Drmosh, A.M.N. Saeed, C. Cheng, K.

1273 Byrappa, ACS Omega 3 (2018), pp. 12260-12269.

1274 [27] T. Zhang, X. Shao, D. Zhang, X. Pu, Y. Tang, J. Yin, B. Ge, W. Li, Sep. Purif. Technol.

1275 195 (2018), pp. 332-338.

1276 [28] X. Zheng, L. Yang, Y. Li, L. Yang, S. Luo, Electrochim. Acta. 298 (2019), pp. 663-669.

1277 [29] J. Chen, Q. Yang, J. Zhonga, J. Li, C. Hu, Z. Deng, R. Duan, Mater. Chem. Phys. 217

1278 (2018), pp. 207–215.

1279 [30] S.L. Prabavathi, K. Govindan, K. Saravanakumar, A. Jang, V. Muthuraj, J. Ind. Eng.

1280 Chem. 80 (2019), pp. 558-567.

1281 [31] P. Chen, X. Dai, P. Xing, X. Zhao, Q. Zhang, S. Ge, J. Si, L. Zhao, Y. He, J. Ind. Eng.

1282 Chem. 80 (2019), pp. 74-82.

1283 [32] Sonu, V. Dutta, S. Sharma, P. Raizada, A.H Bandegharaei, V.K. Gupta, P. Singh, J.

1284 Saudi Chem. Soc. 23 (2019), pp. 1119-1136.

1285 [33] A. Kumar, P. Raizada, P. Singh, R.V. Saini, A.K. Saini, A.H. Bandegharaei. Chem.

1286 Eng. J. (2019), pp. 123496.

1287 [34] P. Singh, S. Gautam, P. Shandilya, B. Priya, V.P. Singh, P. Raizada, Adv. Mater. Lett. 8

1288 (2017), pp. 229-238.

1289 [35] V. Hasija, P. Raizada, V.K. Thakur, A.A.P. Khan, A.M. Asiri, P. Singh, J. Env. Chem.

1290 Eng. (2020), pp. 104307.

1291 [36] P. Raizada, A. Sudhaik, P. Singh, P. Shandilya, V.K. Gupta, A.H. Bandegharaei, S.

1292 Agrawal, J. Photochem. Photobiol. A: Chem. 374 (2019), pp. 22-35.

1293 [37] A. Sudhaik, P. Raizada, S. Thakur, A.K. Saini, P. Singh, A.H. Bandegharaei, J.H. Lim,

1294 D.Y. Jeong, V.H. Nguyen, Appl. Nanosci. (2020), pp. 1-23.

1295 [38] R. Marschall, Adv. Funct. Mater. 24 (2014), pp. 2421-2440.

1296 [39] Y. Wang, H. Suzuki, J. Xie, O. Tomita, D. Martin, M. Higashi, D. Kong, R. Abe, and J.

1297 Tang, Chem. Rev. 118 (10) (2018), pp. 5201-5241.

1298 [40] Y. Tachibana, L. Vayssieres, J. R. Durrant, Nat. Photonics 6 (2012), pp. 511–518.

1299 [41] M. Higashi, Y. Abe, A. Ishikawa, T. Takata, B. Ohtani, K. Domen, Chem. Lett. 37

1300 (2008), pp. 138-139.

1301 [42] R. Abe, K. Sayama, H. Sugihara, J. Phys. Chem. B 109 (2005), pp. 16052-16061.

1302 [43] H. Tada, T. Mitsui, T. Kiyonaga, T. Akita, K. Tanaka, Nat. Mater. 5 (2006), pp. 782.

1303 [44] D. Zhou, Z. Chen, Q. Yang, X. Dong, J. Zhang , L. Qin, Sol. Energy Mater. Sol. Cells

1304 157 (2016), pp. 399–405.

1305 [45] L. Jiang, X. Yua, G. Zeng, J. Liang, Z. Wu, H. Wang, Environ. Sci. Nano 5 (3) (2018),

1306 pp. 599-615

1307 [46] J. Low, C. Jiang, B. Cheng, S. Wageh, A. A. Al-Ghamdi, J. Yu, Small Methods 1 (5)

1308 (2017), pp. 1700080.

1309 [47] X. Wang, G. Liu, Z. G. Chen, F. Li, L. Wang, G. Q. Lu, H. M. Cheng, Chem. Commun.

1310 0 (2009), pp. 3452-3454.

1311 [48] J. Zhang, J. Fu , Z. Wang, B. Cheng, K. Dai, W. Ho, J. Alloys Comp. 766 (2018), pp.

1312 841-850.

1313 [49] J. Zhang, Y. Hu, X. Jiang, S. Chen, S. Meng, X. Fu, J. Hazard. Mater. 280 (2014), pp.

1314 713-722.

[50] X. Yue, X. Miao, Z. Ji, X. Shen, H. Zhou, L. Kong, G. Zhu, X. Li , S. A. Shah, J. Colloid Interface Sci. 531 (2018), pp. 473–482.

[51] T.S. Natarajana, K.R. Thampi, R.J. Tayade, Appl. Catal. B Environ. 227 (2018), pp. 296–311.

[52] J. Wen, J. Xie, X. Chen, X. Li, Appl. Surf. Sci. 391 (2017), pp. 72–123.

[53] S.C. Yan, Z.S. Li, Z.G. Zou, Langmuir 25 (2009), pp. 10397–1040.

[54] M. Ge, Z. Li, Chinese J. Catal. 38 (2017), pp. 1794-1803.

[55] Q. Xu, L. Zhang, J. Yu, S. Wageh, A.A. Al-Ghamdi, M. Jaroniec, Mater. Today 21 (2018), pp. 1042-1063.

[56] S.C. Roy, O.K. Varghese, M. Paulose, C.A. Grimes, ACS Nano 4 (2010), pp. 1259-1278.

[57] N.N. Vu, S. Kaliaguine, T.O. Do, Adv. Funct. Mater. 29 (2019), pp. 1901825.

[58] D. Adekoya, M. Tahir, N.A.S. Amin, Renew. Sust. Energ. Rev. 116 (2019), pp.109389.

[59] L. Spadaro, F. Arena, A. Palella, Methanol (2018), pp. 429-472, In press, 10.1016/B978-0-444-63903-5.00016-9

[60] J.L. White, , M.F. Baruch, J.E. Pander III, Y. Hu, I.C. Fortmeyer, J.E.Park, T. Zhang, Chem. Rev. 115 (2015), pp. 12888-12935.

[61] I. Ganesh, Renew. Sust. Energ. Rev. 31 (2014), pp. 221-257.

[62] K. Li, B. Peng, T. Peng, ACS Catal. 6 (2016), pp. 7485-7527.

[63] A. Corma, H. Garcia, J. Catal. 308 (2013), pp. 168-175.

[64] S. Sato, T. Arai, T. Morikawa, Inorg. Chem. 54 (2015), pp. 5105-5113.

[65] N.T.T. Truc, N.T. Hanh, M.V. Nguyen, N.T.P.L. Chi, N.V. Noi, D.T. Tran, M.N. Ha, D.Q. Trung, T.D. Pham, Appl. Surf. Sci. 457 (2018), pp. 968-974.

[66] P. Melian E,Gonza´lez Dı´az O,OrtegaMe´ndez A,Lo´pez CristinaR, NereidaSua´rez M,Don~aRodrı´guez JM,etal. Int. J. Hydrogen Energy 38 (5) (2013), pp. 2144-2155.

[67] J.J. Suk, K.H. Gyu, L.J. Sung. Cat. Tod. 185 (2012), pp. 270–277.

[68] Z. Wang, C. Li, K. Domen. Chem. Soc. Rev. 48 (2019), pp. 2109-2125.

[69] K. Lalitha, J. K. Reddy, M.V.P. Sharma, V.D. Kumari, M. Subrahmanyam, Int. J. Hydrogen Energy 35 (2010), pp. 3991-4001.

[70] T. da S. Veras, T.S. Mozer, A. da S. César, Int. J. Hydrogen Energ. 42 (2017), pp. 2018-2033.

[71] 1346 N.S. Lewis, Sci. 315 (2007), pp. 798-801.

[72] 1347 I. Roger, M.A. Shipman, M.D. Symes. Nat. Rev. Chem. 1 (2017), pp. 0003.

[73] 1348 J. Yang, D. Wang, H. Han, C. Li, Acc. Chem. Res. 46 (2013), pp. 1900–1909.

[74] 1349 A. Kudo, & Y.Miseki, Chem. Soc. Rev. 38 (2009), pp. 253–278.

[75] 1350 S. Chen, T. Takata K. Domen, Nat. Rev. Mater. 2 (2017), pp. 17050.

[76] 1351 V. Hasija, A. Sudhaik, P. Raizada, A.H. Bandegharaei, P. Singh, J. Environ. Chem. 1352 Eng. 7 (2019), pp. 103272.

[77] 1353 Y. Zheng, , L. Lin, B. Wang, X. Wang, Agew. 54 (2015), pp. 12868-12884.

[78] 1354 M.S. Nasir, G. Yang, I. Ayub, S. Wang, L. Wang, X. Wang, W. Yan, S. Peng, and S. 1355 Ramakarishna. Appl. Catal. B 257 (2019), pp. 117855.

[79] 1356 P. Raizada, , P. Thakur, A. Sudhaik, P. Singh, A.A.P. Khan, V.K Thakur, A.H. 1357 Bandegharaei. Arab. J. Chem. (2019), In press, 10.1016/j.arabjc.2019.10.001

[80] 1358 P. Raizada, A. Sudhaik, P. Singh, A.H. Bandegharaei, P. Thakur. Sep. Purif. Technol. 1359 227 (2019), pp. 115692.

[81] 1360 Y. Wang, Y. Li, X. Bai, Q. Cai, C. Liu, Y. Zuo, S. Kang, L. Cui, Catal. Commun. 84 1361 (2016), pp. 179-182.

[82] 1362 J. Gao, Y. Wang, S. Zhou, W. Lin, Y. Kong, ChemCatChem, 9 (2017), pp. 1708-1715.

[83] 1363 L. Zhou, H. Zhang, H. Sun, S. Liu, M.O. Tade, S. Wang, W. Jin, Catal. Sci. Technol. 6 1364 (2016), pp. 7002-7023.

[84] 1365 S. Xie, Q. Zhang, G. Liu, Y. Wang, Chem. Commun. 52 (2016), pp. 35-59.

[85] 1366 C. Acar, I. Dincer, C. Zamfirescu, Int. J. Energ. Res. 38 (2014), pp. 1903-1920.

[86] 1367 N.S. Lewis, D.G. Nocera, Proc. Natl. Acad. Sci. 43 (2006), pp. 15729-15735.

[87] 1368 K. Maeda, J. Photochem. Photobiol. C 12 (2011), pp. 237-268.

[88] 1369 R.D. Tentu, S. Basu. "Photocatalytic water splitting for hydrogen production, Curr. 1370 Opin. Electrochem. 5 (2017), pp. 56-62.

[89] 1371 M.R. Hoffmann, S.T. Martin, W. Choi, D.W. Bahnemann, Chem. Rev. 95 (1995), pp. 1372 69-96.

[90] 1373 Q. Wang, K. Domen, Chem. Rev. (2019), In press, 10.1021/acs.chemrev.9b00201

[91] 1374 R. Godin, Y. Wang, Martijn A. Zwijnenburg, Junwang Tang, and James R. Durrant, J. 1375 Am. Chem. Soc. 139 (2017), pp. 5216-5224.

1376 [92] J. Shi, J. Chen, Z. Feng, T. Chen, Y. Lian, X. Wang, C. Li, J, Phys. Chem. 111 (2007),
1377 pp. 693-699.

1378 [93] G. Zhang, G. Li, T. Heil, S. Zafeiratos, F. Lai, A. Savateev, M. Antonietti, X. Wang,
1379 Angew. Chem. 131 (2019), pp. 3471-3475.

1380 [94] A. Yamakata, H. Yeilin, M. Kawaguchi, T. Hisatomi, J. Kubota, Y. Sakata, K. Domen,
1381 J. Photochem. Photobiol. A 313 (2015), pp. 168-175.

1382 [95] J. Boltersdorf, I. Sullivan, T.L. Shelton, Z. Wu, M. Gray, B. Zoellner, F.E. Osterloh,
1383 P.A. Maggard, Chem. Mater. 28 (2016), pp. 8876-8889.

1384 [96] B.M. Hunter, H.B. Gray, A.M. Muller, Chem. Rev. 116 (2016), pp. 14120-14136.

1385 [97] S.C. Tsang, V. Caps, I. Paraskevas, D. Chadwick, D. Thompsett, Angew. Chem. 43
1386 (2004), pp. 5645-5649.

1387 [98] F. Dong, Z. Wang, Y. Li, W.K. Ho, S.C. Lee, Environ. Sci. Technol. 48, (2014), pp.
1388 10345-10353.

1389 [99] W. Yu, J. Chen, T. Shang, L. Chen, L. Gu, T. Peng, Appl. Catal. B Environ. 219 (2017),
1390 pp. 693-704.

1391 [100] B. Qiu, Q. Zhu, M. Du, L. Fan, M. Xing, J. Zhang, Angew. Chem. Int. 56 (2017), pp.
1392 2684-2688.

1393 [101] E. Kroke, M. Schwarz, Coord. Chem. Rev. 248 (2004), pp. 493–532.

1394 [102] C. Dong, C. Lian, S. Hu, Z. Deng, J. Gong, M. Li, H. Liu, M. Xing, J. Zhang, Nat.
1395 Commun. 9 (2018), pp. 1-11.

1396 [103] J. Zhou, M. Zhang, Y. Zhu, Phys. Chem. Chem. Phys. 16 (2014), pp. 17627–17633.

1397 [104] S.T. Kochuveedu, Y.H. Jang, D.H. Kim, Chem. Soc. Rev. 42 (2013), pp. 8467-8493.

1398 [105] W. Ong, L. Tan, Y. Hua, S. Yong, S. Chai, Chem. Rev. 116 (2016), pp. 7159−7329.

1399 [106] B. Chai, T. Peng, J. Mao, K. Li, L. Zan, Phys. Chem. Chem. Phys. 14 (2012), pp.
1400 16745–16752.

1401 [107] Y. Zhang, J. Liu, G. Wu, W. Chen, Nanoscale 4 (17) (2012), pp. 5300-5303.

1402 [108] Y. Wang, Z. Wang, S. Muhammad, J. He, Cryst. Eng. Comm. 14 (2012), pp. 5065–
1403 5070.

1404 [109] S. C. Yan, Z. S. Li, and Z. G. Zou, Langmuir 26 (6) (2010), pp. 3894–3901.

1405 [110] F. Dong, L. Wu, Y. Sun, M. Fu, Z. Wu, S.C. Lee, J. Mater. Chem. 21 (2011), pp.
1406 15171-15174.

1407 [111] J. Hong, X. Xia, Y. Wang, R. Xu, J. Mater. Chem. 22 (2012), pp. 15006-15012.

1408 [112] F. Dong, Y. Sun, L. Wu, M. Fu, Z. Wu, Sci. Technol. 2 (2012), pp. 1332–1335.

1409 [113] Y. Kang, Y. Yang, L.C. Yin, X. Kang , G. Liu, H.M. Cheng, Adv. Mater. 27 (2015), pp.
1410 4572–4577.

1411 [114] D.J. Martin, K. Qiu, S.A. Shevlin, A.D. Handoko, X. Chen, Z. Guo, J. Tang, Angew.
1412 Chem. Int. Ed. 53 (2014), pp. 9240–9245.

1413 [115] S. Cao, J. Yu, J. Phys. Chem. Lett. 5 (2014), pp. 2101–2107.

1414 [116] A. Thomas, A. Fischer, F. Goettmann, M. Antonietti, J.O. Muller, R. Schlogl, J.M.
1415 Carlsson, J. Mater. Chem. 18 (2008), pp. 4893–4908.

1416 [117] K. E. Byun, H. J. Chung, J. Lee, H. Yang, H. J. Song, J. Heo, D. H. Seo, S. Park, S. W.
1417 Hwang, I. Yoo, K. Kim, Nano Lett. 13 (2013), pp. 4001-4005.

1418 [118] F. Ou , D.B. Buchholz , F. Yi , B. Liu , C. Hseih , R.P.H. Chang , S.T. Ho, ACS Appl.
1419 Mater. Inter. 3 (2011), pp. 1341.

1420 [119] H. Li, W. Tu, Y. Zhou and Z. Zou, Adv. Sci. 3 (2016), pp. 1500389.

1421 [120] P. Zhou, J. Yu and M. Jaroniec, Adv. Mater. 26 (2014), pp. 4920–4935.

1422 [121] N. Wei, H. Cui, M. Wang, X. Wang, X. Song, L. Ding, J. Tian, RSC Adv. 7 (2017), pp.
1423 18392-18399.

1424 [122] E. Rahmanian, R. Malekfar, M. Pumera, Chem. Eur. J. 23 (2017), pp. 1-15.

1425 [123] F. Shi, L. Chen, M.Chen, D. Jiang, Chem. Commun. 51 (96) (2015), pp. 17144-17147.

1426 [124] S. Chang, A. Xie, S. Chen, J. Xiang, Electroanal. Chem. 719 (2014), pp. 86–91.

1427 [125] S. Samanta, S. Martha and K. Parida, Chem. Cat. Chem. 6 (2014), pp. 1453–1462.

1428 [126] W. Li, C. Feng, S. Dai, J. Yue, F. Hu, H. Hou, Appl. Catal. B Environ. 168 (2015), pp.
1429 465–471

1430 [127] X. Gao, Y. Shang, L. Liu, W. Nie, Opt. Mater. 88 (2019), pp. 229-237.

1431 [128] C. Wang, X. Liu, W. He, Y. Zhao, Y. Wei, J. Xiong, J. Liu et al., J. Catal. 389 (2020),
1432 pp. 440-449.

1433 [129] A. Raza, H. Shen, A.A. Haidry, Appl. Catal. B Environ. 277 (2020), pp. 119239.

1434 [130] M. Dong, W. Juan, G. Mengchun, X. Yanjun, M. Tianjin, S. Yuying, Chem. Eng. J. 290
1435 (2016) 136–146.

1436 [131] X. Hu, J. Hu, Q. Peng, X. Ma, S. Dong, H. Wang, Mater. Res. Bull. 122 (2020), pp.
1437 110682.

1438 [132] B. Palanivel, and Alagiri Mani, ACS Omega 31 (2020), pp. 19747–19759.

1439 [133] F. Shi, L. Chen, M. Chen, D. Jiang, Chem. Comm. 51 (2015), pp. 17144-17147.

1440 [134] J. Hong, D.K. Hwang, R. Selvaraj, Y. Kim, J. Ind. Eng. Chem. 79 (2019), pp. 473-481.

1441 [135] P. Raizada, A. Sudhaik, Pardeep Singh, Mater. Sci. Energy Technol. 2 (2019), 509-525.

1442 [136] L. Jin , Z. Xiaosong, M. Lin , X. Limei , D. Zhihua, Z. Jinquan, Mater. Res. Bull. 81
1443 (2016), pp. 16-26.

1444 [137] K. Sharma, V. Dutta, S. Sharma, P. Raizada, A.H. Bandegharaei, P. Thakur, P. Singh, J.
1445 Ind. Eng. Chem. 78 (2019), pp. 1-20.

1446 [138] V. Dutta, P. Singh, P. Shandilya, S. Sharma, P. Raizada, A.K. Saini, V.K. Gupta, A.H.
1447 Bandegharaei, S. Agarwal, A.R. Sani, J. Environ. Chem. Eng. 7 (2019), pp. 103132.

1448 [139] J. Low, B. Dai, T. Tong, C. Jiang, J. Yu, Adv. Mater. 31 (2019), pp. 1802981.

1449 [140] W. Chen, Z. He, G. Huang, C. Wu, W. Cheng, W. Chen X. Liu, Chem. Eng. J. 359
1450 (2018), pp. 244-253.

1451 [141] L. Tian, X. Yang, X. Cui, Q. Liu, H. Tang, Appl. Surf. Sci. 463 (2019), pp. 9-17.

1452 [142] N. Shehzad, M. Tahir, K. Johari, T. Murugesan, M. Hussai, J. CO_2 Utilization 26
1453 (2018), pp. 98–122.

1454 [143] Y. Sun, Z. Lin, S. Hong, V. Sage, Z. Sun, J. Nanosci. Nanotechnol. 19 (6) (2019), pp.
1455 3097-3019.

1456 [144] J. White, M. Baruch, J. Pander, Y. Hu, I. Fortmeyer, J. Park, T. Zhang, K. Liao, J. Gu,
1457 Y. Yan, T. Shaw, E. Abelev, B. Andrew, Chem. Rev. 115 (23) (2015), pp. 12888-
1458 12935.

1459 [145] K. Li, B. Peng, T. Peng, ACS Catal. 6 (2016), pp. 7485−7527.

1460 [146] P. Raizada, S. Sharma, A. Kumar, P. Singh, A.A.P. Khan, A.M. Asiri, J. Environ.
1461 Chem. Eng. (2020), pp. 104230.

1462 [147] P. Raizada, A. Kumar, P. Singh, Curr. Anal. Chem. 16 (2020), pp. 1-00.

1463 [148] R. Kumar, A. Sudhaik, P. Raizada, A.H. Bandegharaei, V.K. Thakur, A. Saini, V. Saini,
1464 P. Singh, J. Environ. Chem. Eng. (2020), pp. 104291.

1465 [149] P. Raizada, A. Sudhaik, V.P. Singh, V.K. Gupta, A.H. Bandegharaei, R. Kumar, P.
1466 Singh, Desalin. Water Treat. 148 (2019), pp. 338-350.

1467 [150] W.K. Jo, S. Kumar, S. Eslava, S. Tonda, Appl. Catal. B, 239 (2018), pp. 586-598.

[151] P. Murugesan, S. Narayanan, M. Matheswaran, M. Praveen, S. Ravichandran, Appl. Surf. Sci. 450 (2018), pp. 516-526.

[152] D. Xu, B. Cheng, W. Wang, C. Jiang, J. Yu, Appl. Catal. B Environ. 231 (2018), pp. 368-380.

[153] N. Sakai, Y. Ebina, K. Takada, T. Sasaki, J. Phys. Chem. , 109 (2005), pp. 9651-9655.

[154] M. Wang, M. Shen, L. Zhang, J. Tian, X. Jin, Y. Zhou, J. Shi, Carbon 120 (2017), pp. 23-31.

[155] R. Rameshbabu, P. Ravi, M. Sathish, Chem. Eng. J. 360 (2019), pp. 1277-1289.

[156] Y. Zhu, L. Wang, Y. Liu Y, L. Shao, Appl. Catal. B Environ. 241 (2019), pp. 483-490.

[157] X. Wang, W. Gao, Z. Zhao, L. Zhao, J. Claverie, X. Zhang, J. Wang, H. Liu, Y. Sang, Appl. Catal. B Environ. 248 (2019), pp. 388-393.

[158] Y. Lai, Y. Dai, J. Jehng, Catal. Today 325 (2019), pp. 41-46.

[159] S. Bellamkonda, N. Thangavel, H. Yusuf, B. Neppolian, G. Ranga, Catal. Today 321 (2019), pp. 120-127.

[160] Z. Mo, H. Xu, Z. Chen, X. She, Y. Song, J. Lian, X. Zhu, P. Yan, Y. Lei, S. Yuan, H. Li, Appl. Catal. B Environ. 241 (2019), pp. 452-460.

[161] J. Cui, Y. Qi Y, B. Dong, L. Mu, Q. Ding, G. Liu, M. Jia, F. Zhang, C. Li, Appl. Catal. B Environ. 241 (2019), pp. 1-7.

[162] S. Nayak and K. Parida, Sci. Rep. 9 (2019), pp. 2458.

[163] J. Olowoyo, M. Kumar, S. Jain, J. Babalola, A. Vorontsov, U. Kumar, J. Phys. Chem. C 123 (2019), pp. 367−378.

[164] J. Wang, X. Li, Y. You, X. Yang, Y. Wang, Q. Li, Nanotechnology 29 (2018), pp. 365401.

[165] S. Bera, S. Ghosh, S. Shyamal, C. Bhattacharya, R. Basu, Sol. Energy Mater. Sol. Cells 194 (2019), pp. 195−206.

[166]   L. F. Garay, L. M. Torres, E. Moctezuma, J. Energy Chem. 37 (2018), pp. 18-28.

[167] X.Ke, K. Dai, G. Zhu, J. Zhang, C. Liang, Appl. Surf. Sci. 481 (2019), pp. 669-677.

[168] E. Liu, L. Qi, J. Chen, J. Fan, X. Hu, Mater. Res. Bulletin 115 (2019), pp. 27-36.

[169] Y. Jiang, F. Li, Y. Liu, Y. Hong, P. Liu, L. Ni, J. Ind. Eng. Chem. 41 (2016), pp. 130-140.

1498 [170] Y. Li, Z. Yin, G. Ji, Z. Liang, Y. Xue, Y. Guo, J. Tian, X. Wang, H. Cui, Appl. Catal. B
1499 Environ. 246 (2019), pp. 12-20.

1500 [171] J. Xu, Y. Qi, L. Wang, Appl. Catal. B Environ. 246 (2019), pp. 72-81.

1501 [172] L. Tie, S. Yang, C. Yu, H. Chen, Y. Liu, S. Dong, J. Sun, J. Sun, J. Colloid and
1502 Interface Sci. 545 (2019), pp. 63-70.

1503 [173] G. Zhang, W. Ou, J. Wang, Y. Xu, D. Xu, T. Sun, S. Xiao, M. Wang, H. Li, W. Chen,
1504 C. Su, Appl. Catal. B Environ. 245 (2019), pp. 114-121.

1505 [174] H. Yu, Y. Huang, D. Gao, P. Wang, H. Tang, Ceram. Int. 45 (2019), pp. 9807-9813.

1506 [175] Y. Zou, J. W. Shi, D. Ma, Z. Fan, C. Niu, L. Wang, Chem. Cat. Chem. 9 (2017), pp.
1507 3752-3761.

1508 [176] A. J. Medford and M. C. Hatzell, ACS Catal. 7 (2017), pp. 2624-2643.

1509 [177] H. Li, J. Shang, Z. Ai, L. Zhang, J. Am. Chem. Soc. 137 (2015), pp. 6393-6399.

1510 [178] L. Z. zhang, H. Li, J. Shang, J. Shi and K. Zhao, Nanoscale 8 (2016), pp. 1986-1993.

1511 [179] S. Cao, N. Zhou, F. Gao, H. Chen, F. Jiang, Appl. Catal. B Environ. 218 (2017), pp.
1512 600-610.

1513 [180] S. Liu, S. Wang, Y. Jiang, Z. Zhao, G. Jiang, Z. Sun, Chem. Eng. J. 373 (2019), pp.
1514 572-579.

1515 [181] Y. Wang, X. Gao, L. Zhang, X. Wu, Q. Wang, C. Luo, G. Wu, Appl. Surf. Sci. 480
1516 (2019), pp. 830-838.

1517 [182] Y. Wang, X. Gao, X. Wu, C. Luo, Ceram. Int. 46 (2020), pp. 1560-1568.

1518 [183] Y. Wang, W. Zhang, X. Wu, C. Luo, Q. Wang, J. Li, L. Hu, Synthetic Met. 228 (2017),
1519 pp. 18-24.

1520 [184] Y. Wang, X. Gao, Y. Fu, X. Wu, Q. Wang, W. Zhang, C. Luo, Compos. Part B: Eng.
1521 169 (2019), pp. 221-228.

1522 [185] Y. Wang, X. Gao, X. Wu, W. Zhang, C. Luo, P. Liu, Chem. Eng. J. 375 (2019), pp.
1523 121942.

1524 [186] B. J. Ng, L. K. Putri, L. L. Tan, P. Pasbakhsh, S. P. Chai, Chem. Eng. J. 316 (2017), pp.
1525 41-49.

1526 [187] K. Iwashina, A. Iwase, Y. H. Ng, R. Amal, A. Kudo, J. Am. Chem. Soc. 132 (2015), pp.
1527 604-607.

1528 [188] W. K. Jo, N. C. S. Selvam, Chem. Eng. J. 317 (2017), pp. 913-924.

[189] A. Iwase, Y. H. Ng, Y. Ishiguro, A. Kudo, R. Amal, J. Am. Chem. Soc. 133 (2011), pp. 11054-11057.

[190] K. Kamijyo, T. Takashima, M. Yoda, J. Osaki, H. Irie, Chem. Commun. 54 (2018), pp. 7999-8002.

[191] D. Lu, H. Wang, X. Zhao, K.K. Kondamareddy, J. Ding, C. Li, P. Fang. ACS Sustain. Chem. Eng. 5 (2017), pp. 1436-1445.

[192] H. Zhao, X. Ding, B. Zhang, Y. Li, C. Wang, Sci. Bulletin 62 (2017), pp. 602-609.

[193] X. Ma, Q. Jiang, W. Guo, M. Zheng, W. Xu, F. Ma and B. Hou, RSC Adv. 6 (2016), pp. 28263-28269.

[194] W. Zhao, L. Xie, M. Zhang, Z. Ai, H. Xi, Y. Li, Q. Shi, J. Chen, Int. J. Hydrogen Energy 41 (2016), pp. 6277-6287.

[195] J. Wen, J. Xie, H. Zhang, A. Zhang, Y. Liu, X. Chen, X. Li, ACS Appl. Mater. Interfaces 9 (2017), pp. 14031-14042.

[196] X. Yang, Z. Chen, J. Xu, H. Tang, K. Chen, Y. Jiang, ACS Appl. Mater. Interfaces 7 (2015), pp. 15285-15293.

[197] Y. He, L. Zhang, B. Teng, M. Fan, Environ. Sci. Technol. 1 (2014), pp. 649-656.

[198] Y. Bai, T. Chen, P. Wang, L. Wang, L. Ye, X. Shi, W. Bai, Solar Energy Mater. Sol. Cells 157 (2016), pp. 406-414.

[199] J. Wang, Y. Xia, H. Zhao, G. Wang, L. Xiang, J. Xu, S. Komarneni, Appl. Catal. B Environ. 206 (2017), pp. 406-416.

[200] Q. Xu, B. Zhu, C. Jiang, B. Cheng, J. Yu, Sol. RRL 2 (2018), pp. 1800006.

[201] X. She, J. Wu, H. Xu, J. Zhong, Y. Wang, Y. Song, K. Nie, Y. Liu, Y. Yang, M. T. F. Rodrigues, R. Vajtai, J. Lou, D. Du, H. Li, P. M. Ajayan, Adv. Energy Mater. (2017), pp. 1700025.

[202] Z. Dong, Y. Wu, N. Thirugnanam, G. Li, Appl. Surf. Sci. 430 (2018), pp. 293-300.

[203] Y. Liu, H. Liu, H. Zhou, T. Li, L. Zhang, Appl. Surf. Sci. 466 (2019), pp. 133-140.

[204] C. Yang Z. Xue, J. Qin, M. Sawangphruk, S. Rajendran, X. Zhang, and R. Liu, J. phys. Chemi. C photochem. Rev. (2019), In press, DOI: 10.1021/acs.jpcc.8b10604.

[205] Y. Shi, J. Chen, Z. Mao, B. D. Fahlman, D. Wang, J. Catal. 356 (2017), pp. 22-31.

[206] K. He, J. Xie, X. Luo, J. Wen, S. Ma, X. Li, Y. Fang, X. Zhang, Chin. J. Catal. 38 (2017), pp. 240–252.

1560 [207] W. Chang, W. Xue, E. Liu, J. Fan, B. Zhao, Chem. Eng. J. 362 (2019), pp. 392-401.

1561 [208] J. Dong, Y. Shi, C. Huang, Q, Wu, T, Zeng, W. Yao, Appl. Catal. B Environ. 243

1562 (2018), pp. 27-35.

1563 [209] Z. Chen, P. Chen, P. Xing, X. Hu, H. Lin, L. Zhao, Y. Wu, Y. He, Fuel 241 (2019), pp.

1564 1-11.

1565 [210] J. Fu, Q. Xu, J. Low, C. Jiang, J. Yu, Appl. Catal. B Environ. 243 (2018), pp. 556-565.

1566 [211] D. D. Yang, X. J. Sun, H. Dong, X. Zhang, H. L. Tang, J. L. Sheng, J. Z. Wei, F. M.

1567 Zhang, Mater. Sci. Semicond. Process. 85 (2018), pp. 76-82.

1568 [212] M. W. Kadi and R. M. Mohamed, Ceram. Int. 45 (3) (2019), pp. 3886-3893.

1569 [213] E. Liu, J. Chen, Y. Ma, J. Feng, J. Jia, J. Fan, X. Hu, J. Colloid Interface Sci. 524

1570 (2018), pp. 313-324.

1571 [214] X. Wanga, Z. Zhaoa, Z. Shua, Y. Chena, J. Zhoua, T. Lic, W. Wanga, Y. Tana, N. Sun,

1572 Appl. Clay Sci. 166 (2018), pp. 80-87.

1573 [215] X. Lu, J. Xie, A. A. Jeffery, X. Chen, and X. Li, Appl. Catal. B Environ. (2019), In

1574 press, 10.1016/j.apcatb.2019.04.012

1575 [216] J. U. Choi, Y. G. Kim, W. K. Jo, Appl. Surf. Sci. 473 (2019), pp. 761-769.

1576 [217] J. Wang, G. Wang, X. Wang, Y. Wu, Y. Su, H. Tang, Carbon 149 (2019), pp. 618-626.

1577 [218] R. Cao, H. Yang, S. Zhang, X. Xu, Appl. Catal. B 258 (2019), pp. 117997.

1578 [219] P. Mishra, A. Behera, D. Kandi, K. Parida, Nanoscale Adv. 1 (2019), pp. 1864-1879.

1579 [220] Y. Jiao, Q. Huang, J. Wang, Z. He, Z. Li, Appl. Catal. B 247 (2019), pp. 124-132.

1580 [221] F. Raziq, Y. Qu, M. Humayun, A. Zada, H. Yu, L. Jing, Appl. Catal. B Environ. 201

1581 (2017), pp. 486-494.

1582 [222] N. Nie, L. Zhang, J. Fu, B. Cheng, J. Yu, Appl. Surf. Sci. 441 (2018), pp. 12-22.

1583 [223] Y. Huo, J. Zhang, K. Dai, Q. Li, J. Lv, G. Zhu, C. Liang, Appl. Catal. B Environ. 241

1584 (2018), pp. 528-538.

1585 [224] Y. Meng, L. Zhang, H. Jiu, Q. Zhang, H. Zhang, W. Ren, Y. Sun, D. Li, Mater. Sci.

1586 Semicond. Proc. 95 (2019), pp. 35-41.

1587 [225] T. Di, B. Zhu, B. Cheng, J. Yu, J. Xu, J. Catal. 352 (2017), pp. 532-541.

1588 [226] X. Yang, W. Xin, X. Yin, X. Shao, Chem. Phys. Lett. 651 (2016), pp. 127-132.
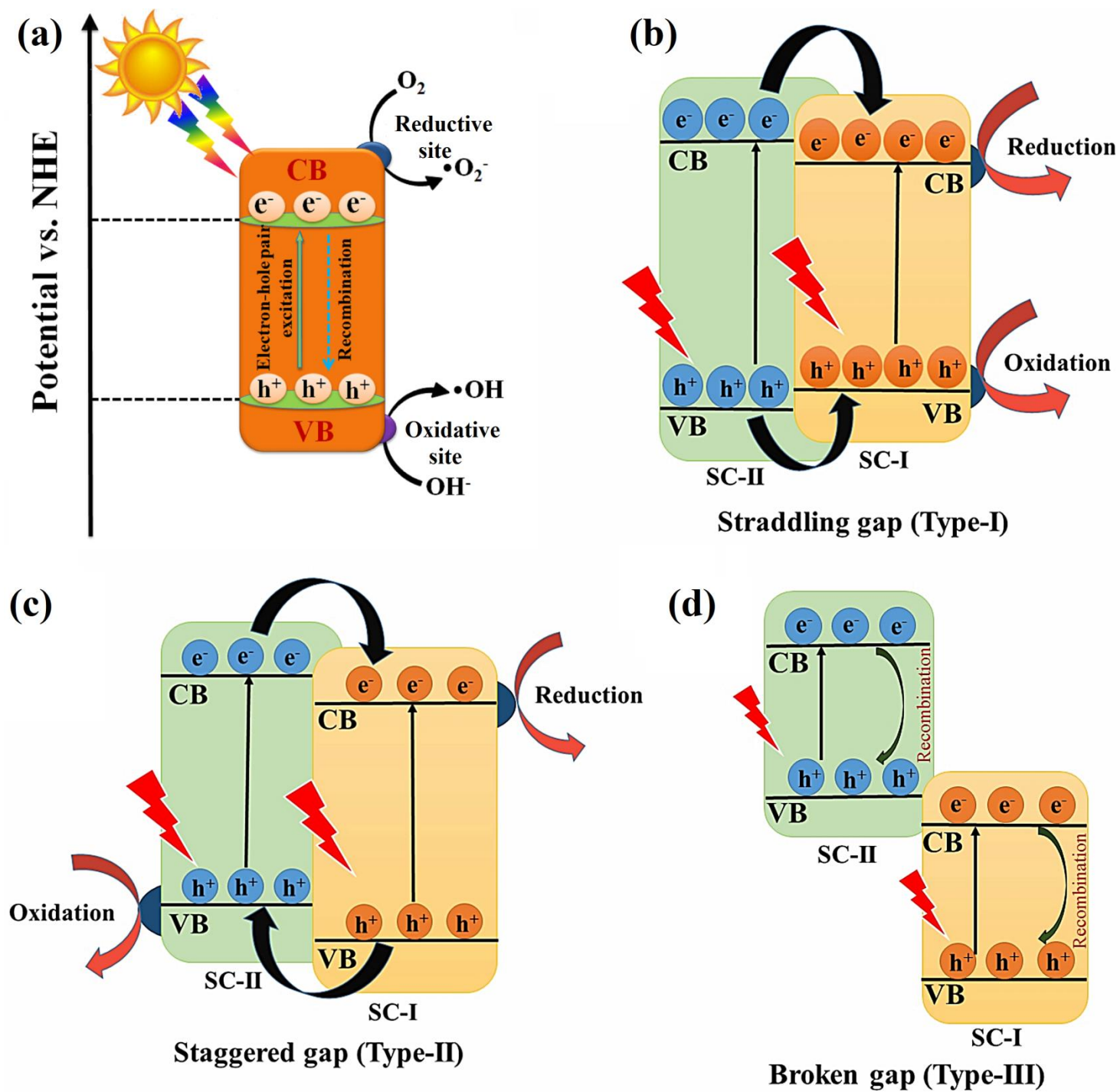
1589

1590

Figure

Fig. 1. (a) Schematic illustration of basic principle of photocatalysis. Traditional heterojunction photocatalysis illustrating double charge transfer mechanism in: (b) Type-I heterojunction, (c)

type-II heterojunction and (c) representation of broken band gap situation in type-III heterojunction, SC-I and SC-II represents semiconductor-I and semiconductor-II, respectively.
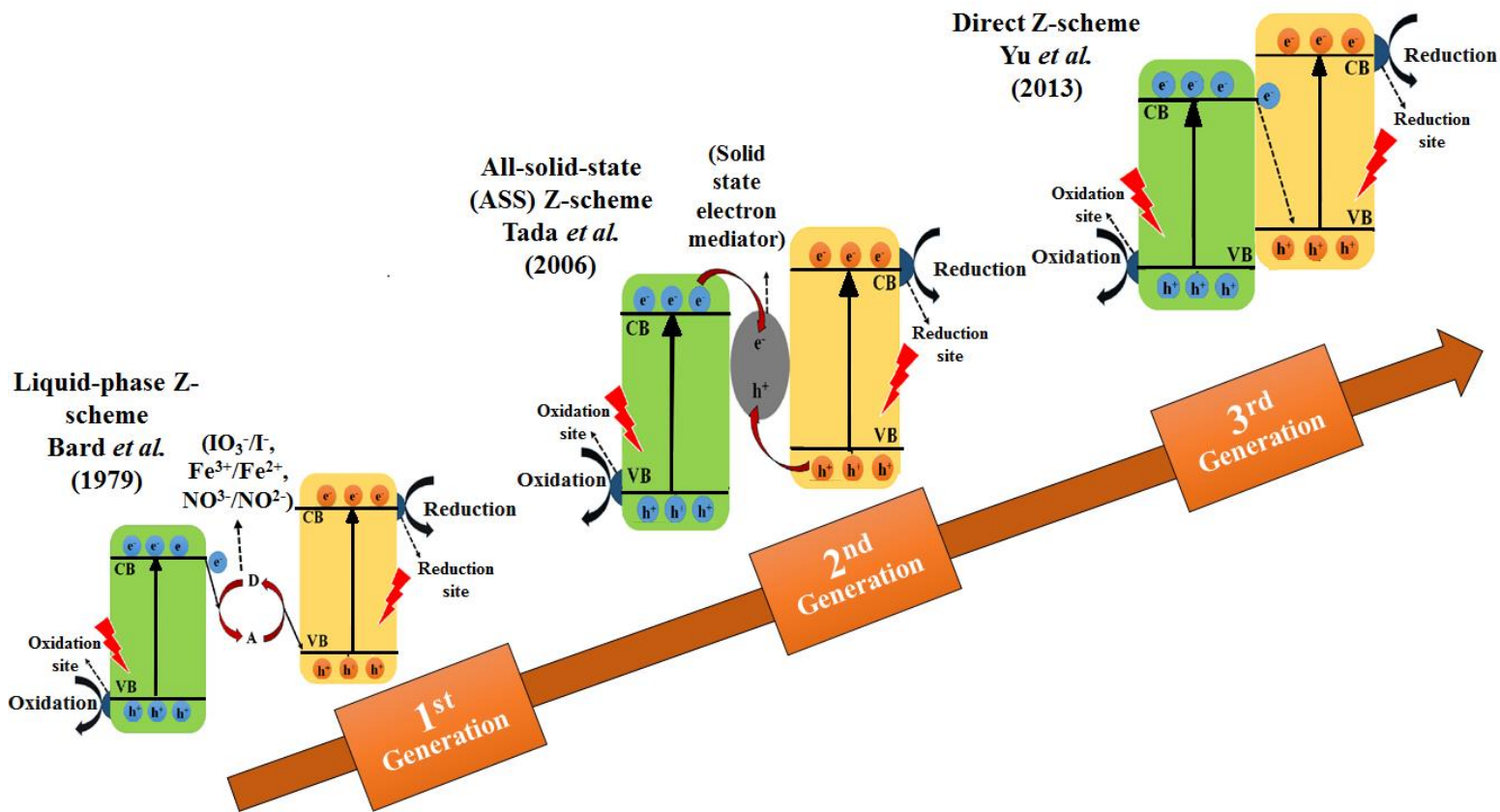

Fig. 2. Schematic illustration showing progression of Z-scheme photocatalysis from 1st generation to current 3rd generation. A/D, Acceptor/Donor pair.
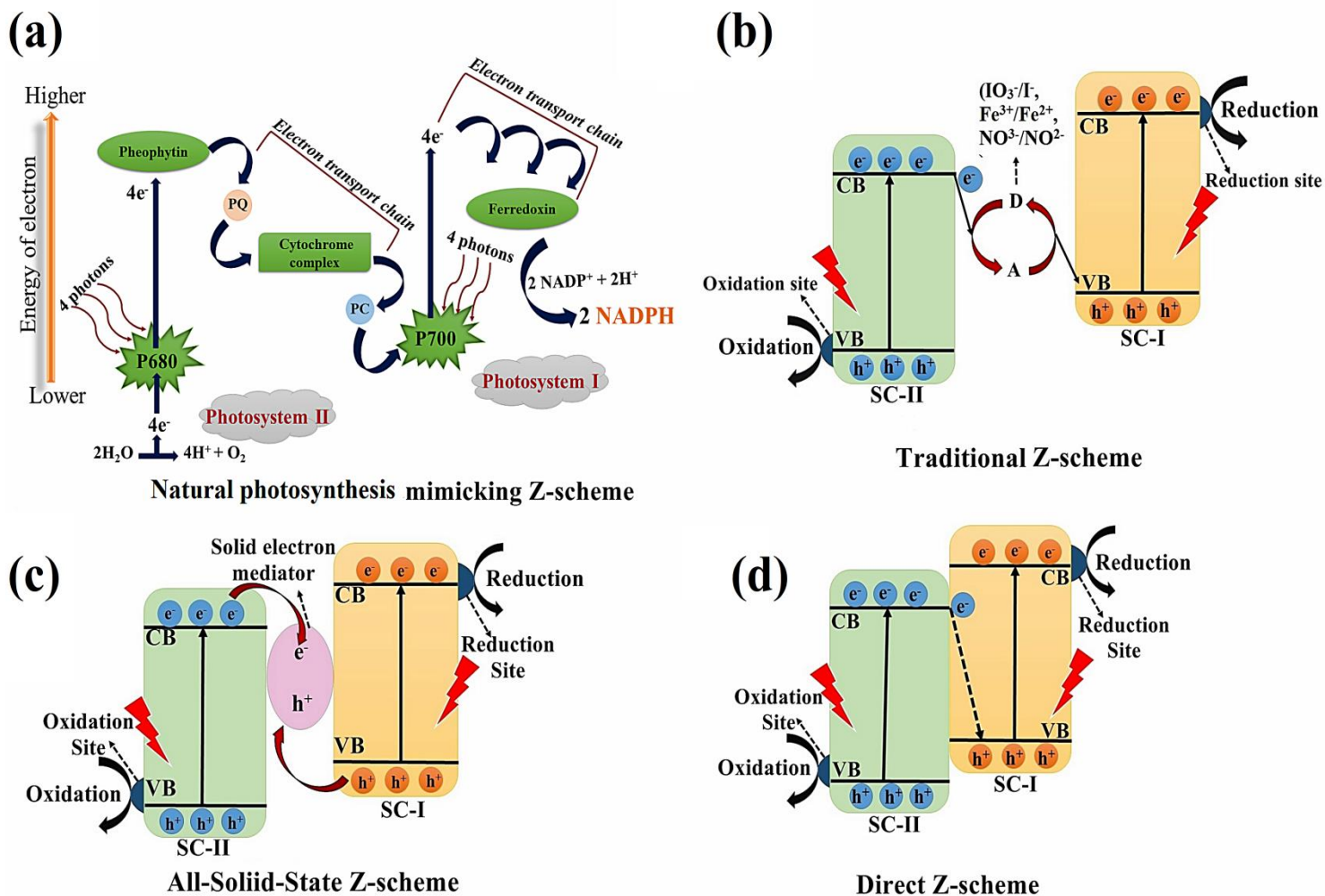
Fig. 3. (a) A schematic representation of double excitation process occurring on P680 and P700 through Natural Photosynthesis. (b) Charge transfer mechanism in traditional Z-scheme system with liquid-phase redox mediators, A and D represents Acceptor and donor pairs, respectively. (c) Charge transfer mechanism in all-solid-state Z-scheme system with solid state electron mediator and (d) Scheme of charge transfer and separation in direct Z-scheme system.
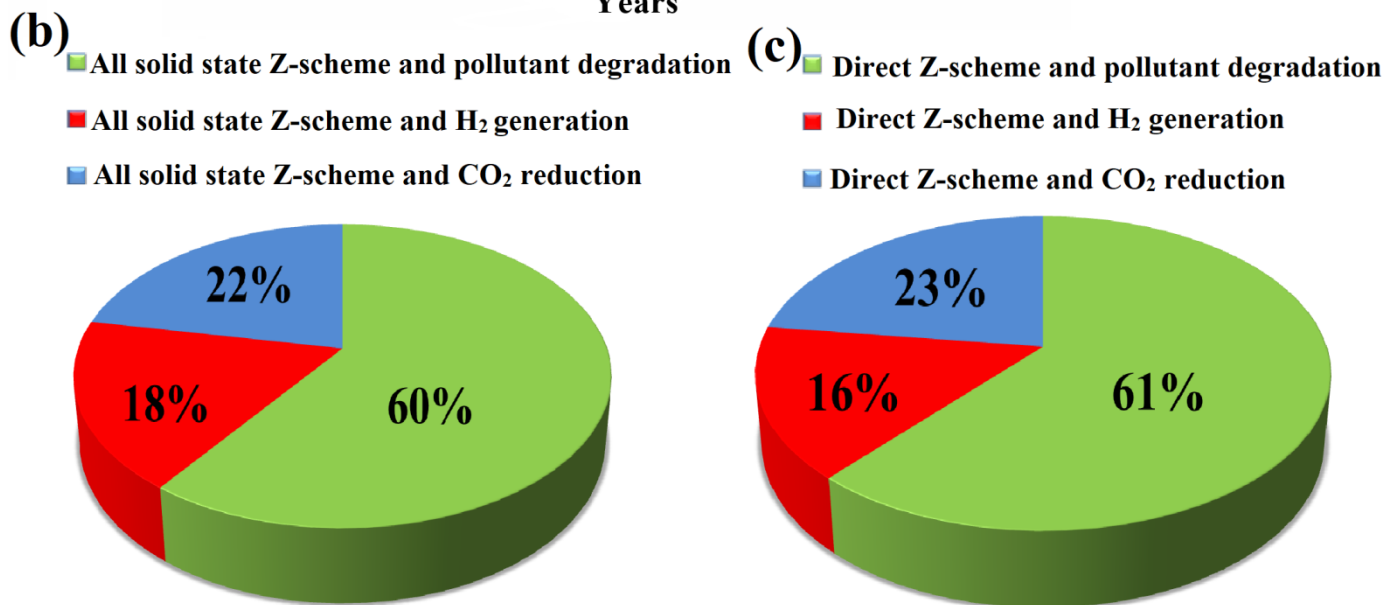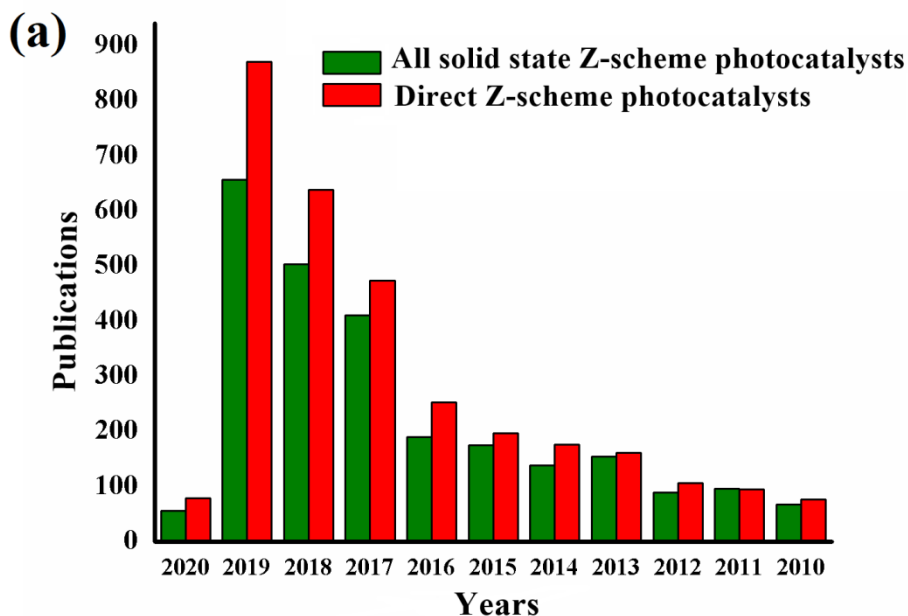
Fig. 4. (a) Total publications from 2009 to January, 2020 through Scopus Search Engine using keywords "All solid state Z-scheme Photocatalysts" and "Direct Z-Scheme Photocatalysts". Environmental and energy applications representing the total percentage of; (b) All solid state Z-scheme photocatalysts and (b) Direct Z-scheme photocatalysts.
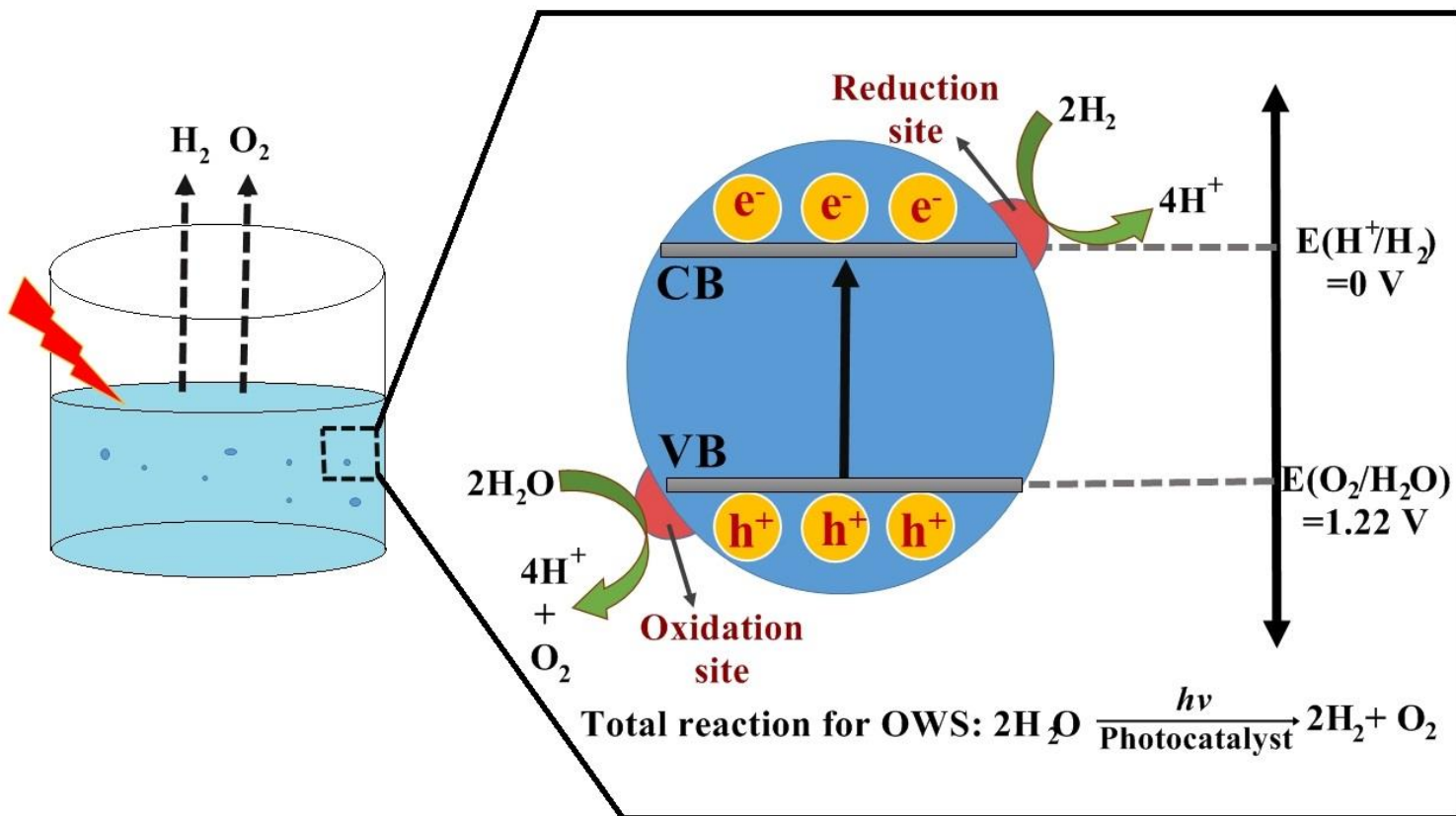
Fig. 5. Schematic illustration of visible light driven water splitting process carried on a single photocatalyst system.
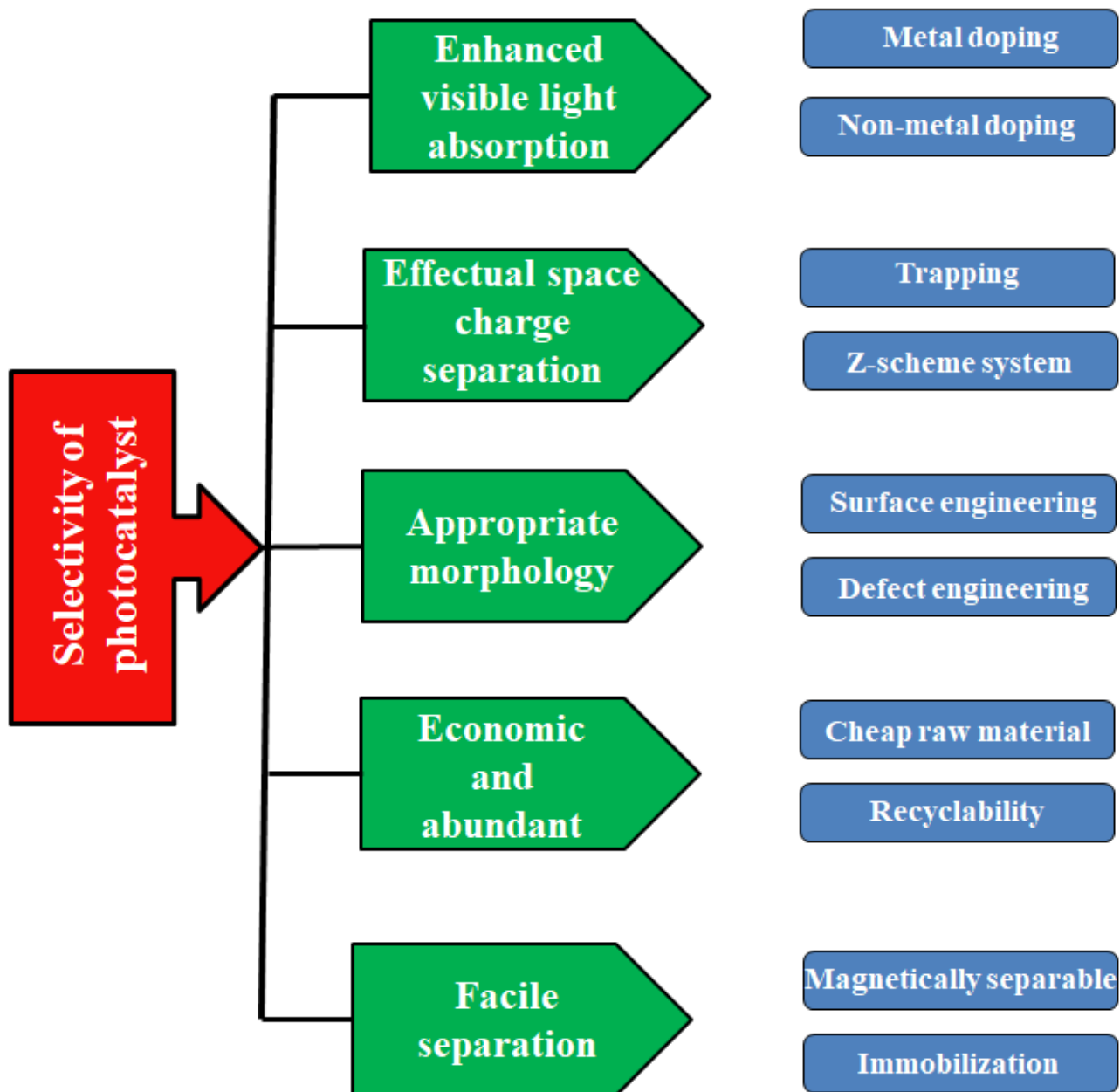
Fig. 6. Diagrammatic representation of basic aspects involved in selectivity of photocatalyst.
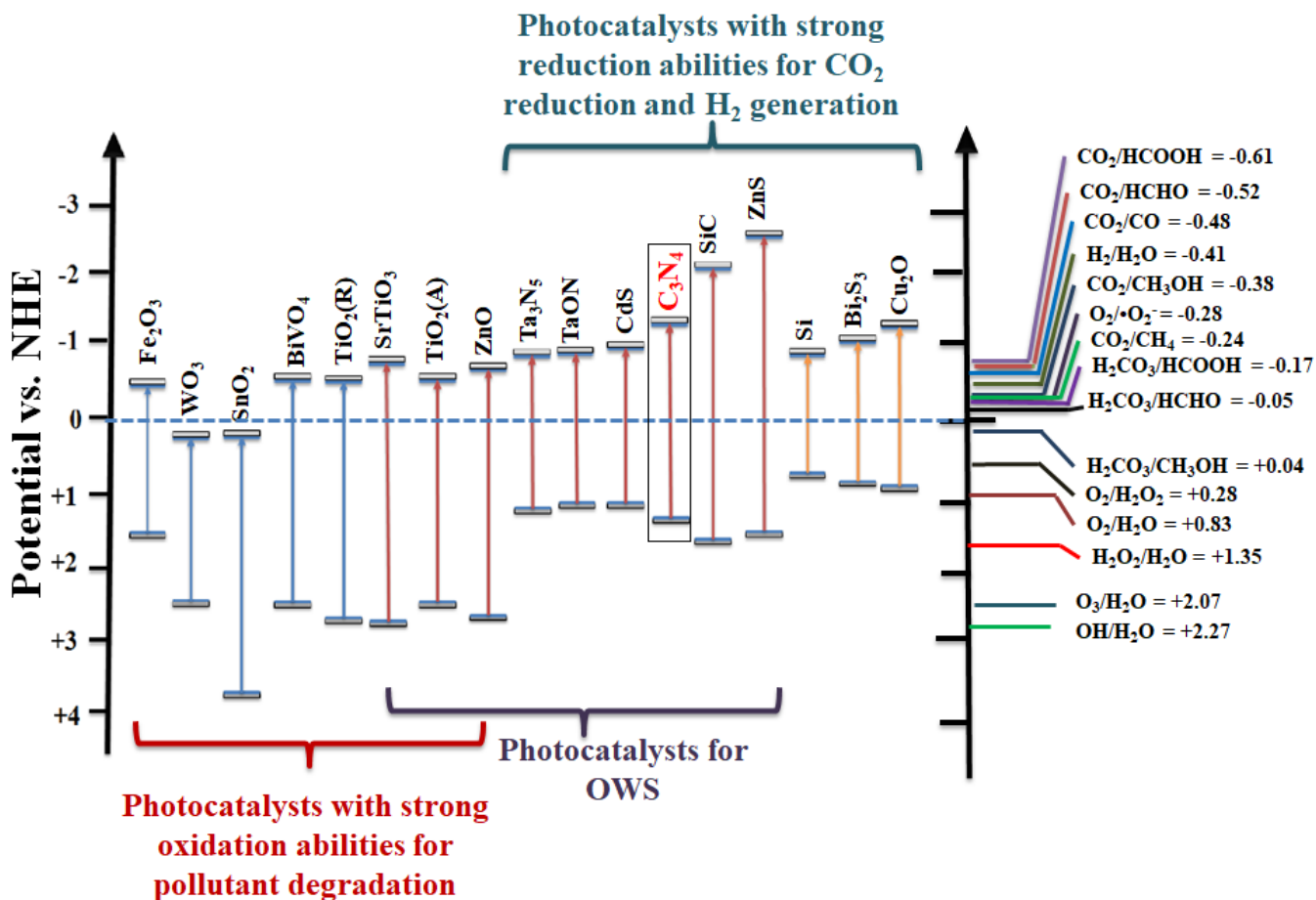
Fig. 7. Representation of redox potentials of various photocatalysts for their application in environmental and energy remediation.
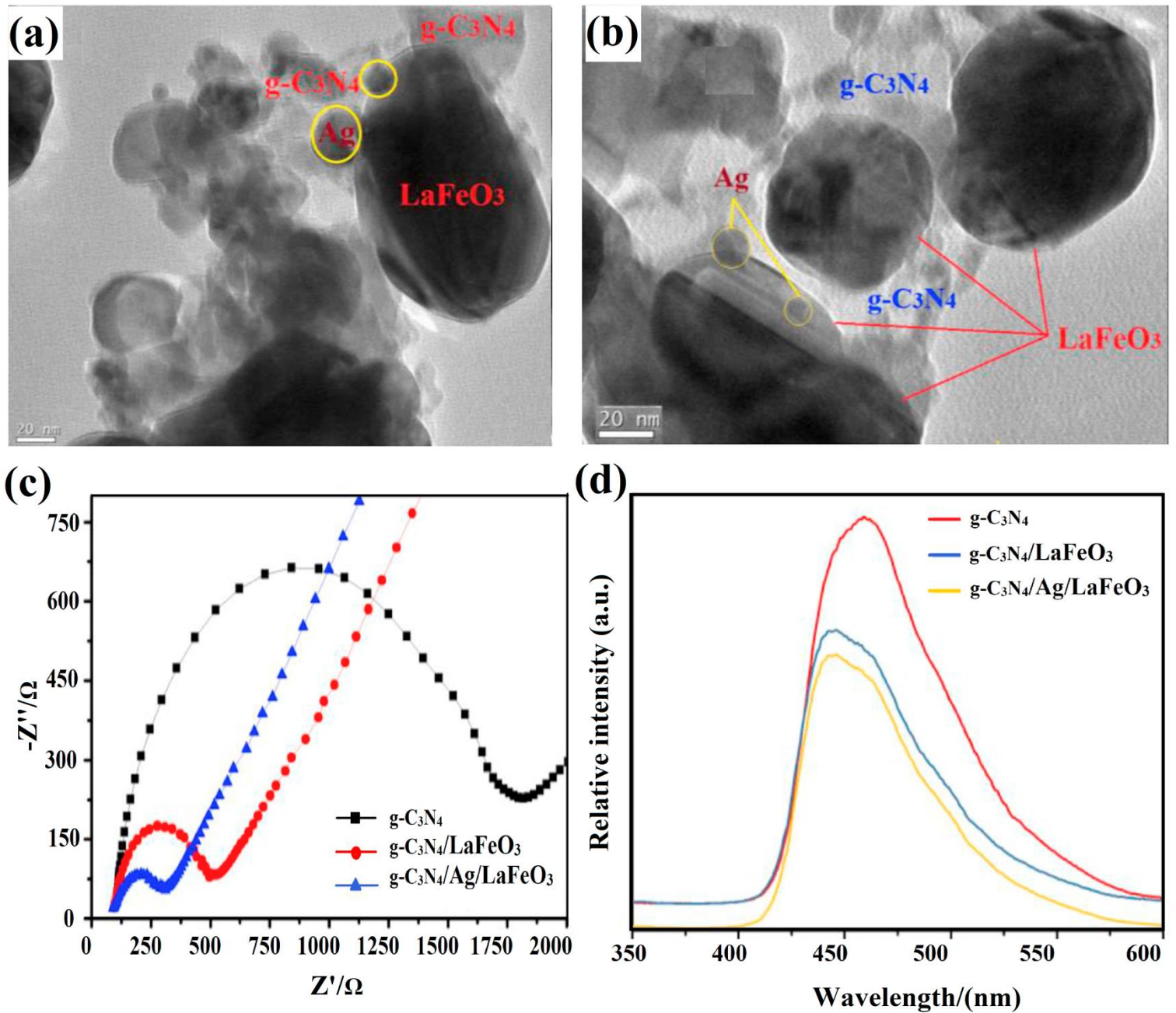
Fig. 8. Schematic illustration of: (a, b) TEM images of g-C$_3$N$_4$/Ag/LaFeO$_3$ nanohybrid, (c) EIS spectrum and (d) photoinduced fluorescence spectroscopic analysis of g-C$_3$N$_4$, g-C$_3$N$_4$/LaFeO$_3$

and g-C$_3$N$_4$/Ag/LaFeO$_3$ nanohybrid. Adapted from Elsevier under <mark>License No. 4891440827977)</mark> <mark>[127]</mark>.

(a)

PMMA opal → Ti Precursor Impregnation → Ti+PMMA

Carbon-coated TiO₂ nanocrystals

Anaerobic Calcination

TiO₂@Carbon

Pt Load GBMR → Pt/TiO₂@C

g-C₃N₄ In-situ growth → CNPT

(b)

Legend:
- 3DOM-TiO₂
- g-C₃N₄
- 3DOM-TiO₂@C
- g-C₃N₄/3DOM-TiO₂@C
- Pt/3DOM-TiO₂@C
- 3DOM-CNPTC

Y-axis: Photocurrent density (A m⁻²)
X-axis: Time (s)

(c)

under Dark
- CZTS
- CZ/3wt% PCN

under Light
- CZTS
- CZ/3wt% PCN

Y-axis: Current density (mA cm⁻²)
X-axis: Potential (v)

(d)

g-C₃N₄ 2.8 eV CZTS 1.52 eV

I Type I Heterojunction
II LSPR effect
III Electron sink effect

Type I Heterojunction

g-C₃N₄ 2.8 eV CZTS 1.52 eV

I Z-scheme charge transfer
II LSPR effect
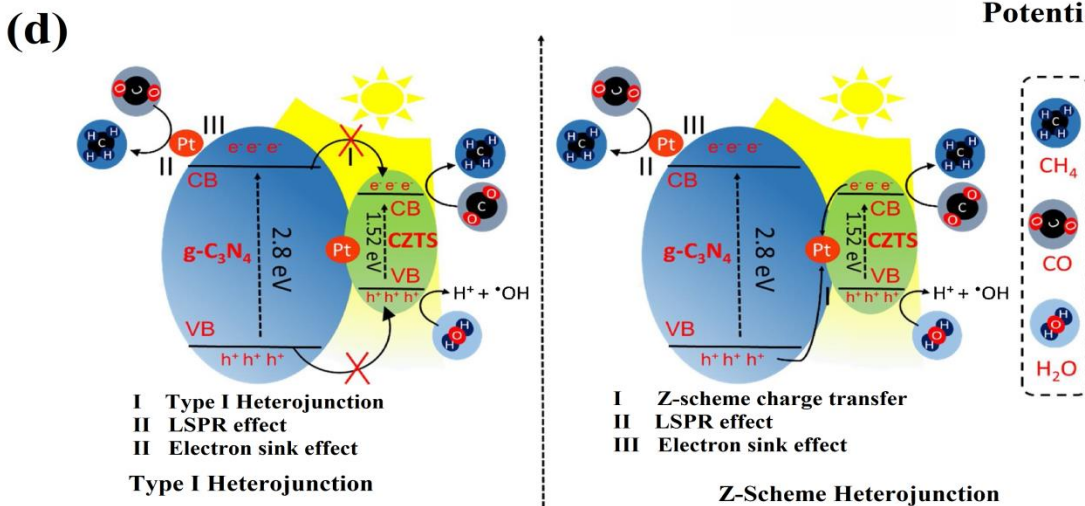III Electron sink effect
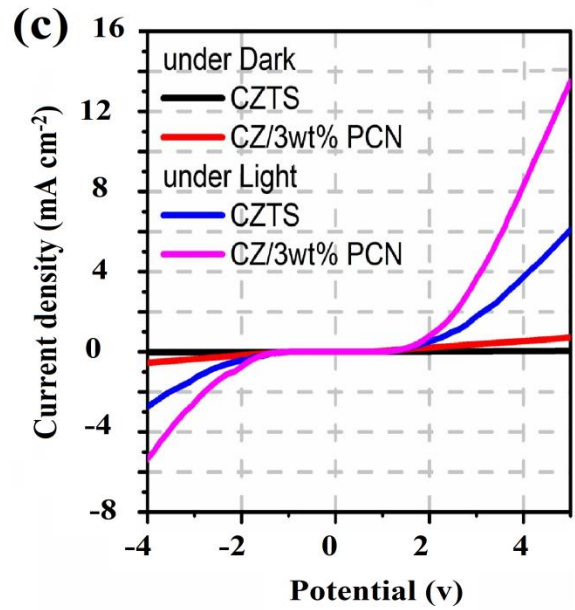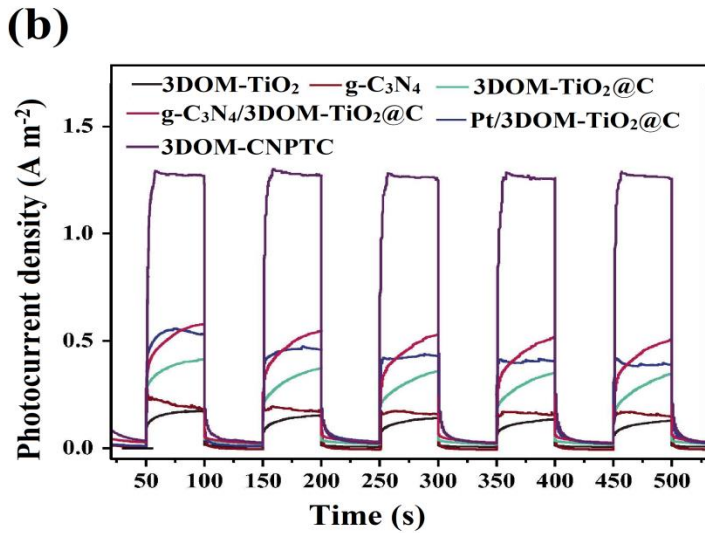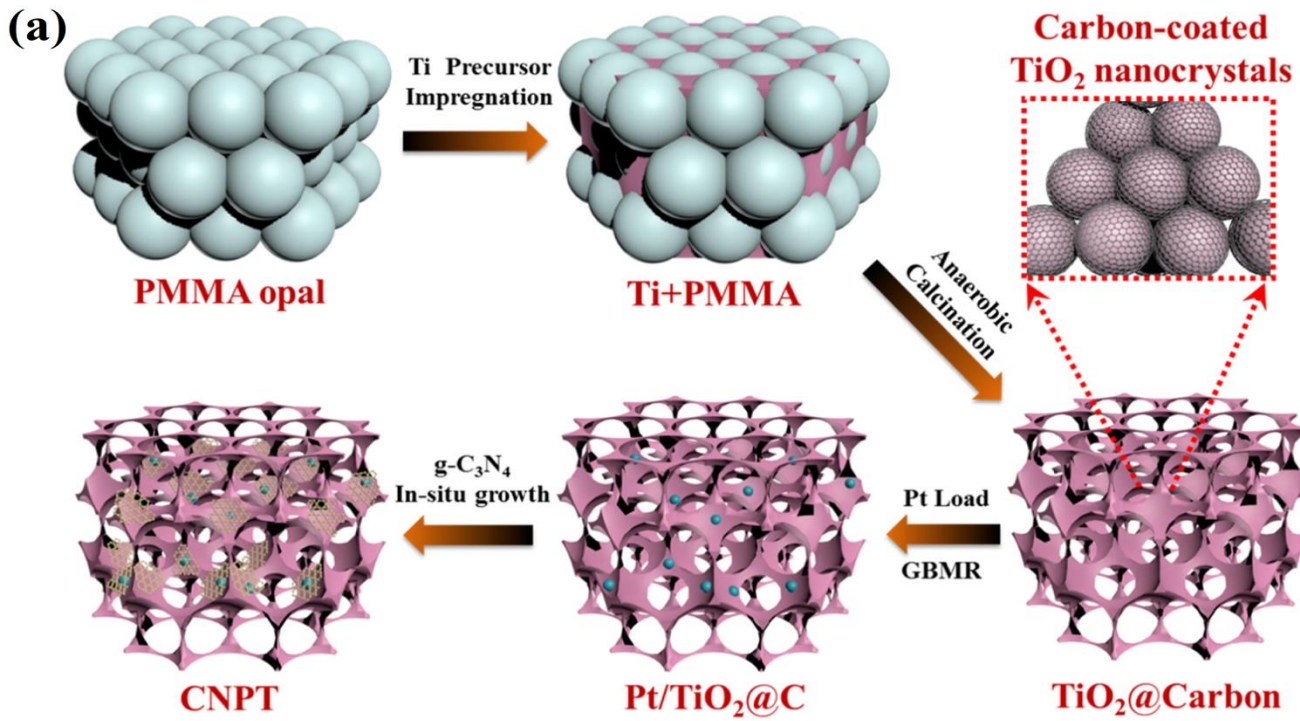
Z-Scheme Heterojunction

CH₄
CO
H₂O

Fig. 9. Schematic illustration of: (a) mechanistic insight into the synthesis process of 3DOM-CNPTC photocatalyst, (b) Photocurrent responses of various samples, (c) LSV curves of various samples under dark and light illumination, adapted with permission from Elsevier (License no. 4891450608052) [128], and (d) distinct charge migration modes for photocatalytic CO_2 reduction in CZ/3 wt% PCN heterostructures, reproduced with permission from Elsevier (License no. 4891450418062) [129].
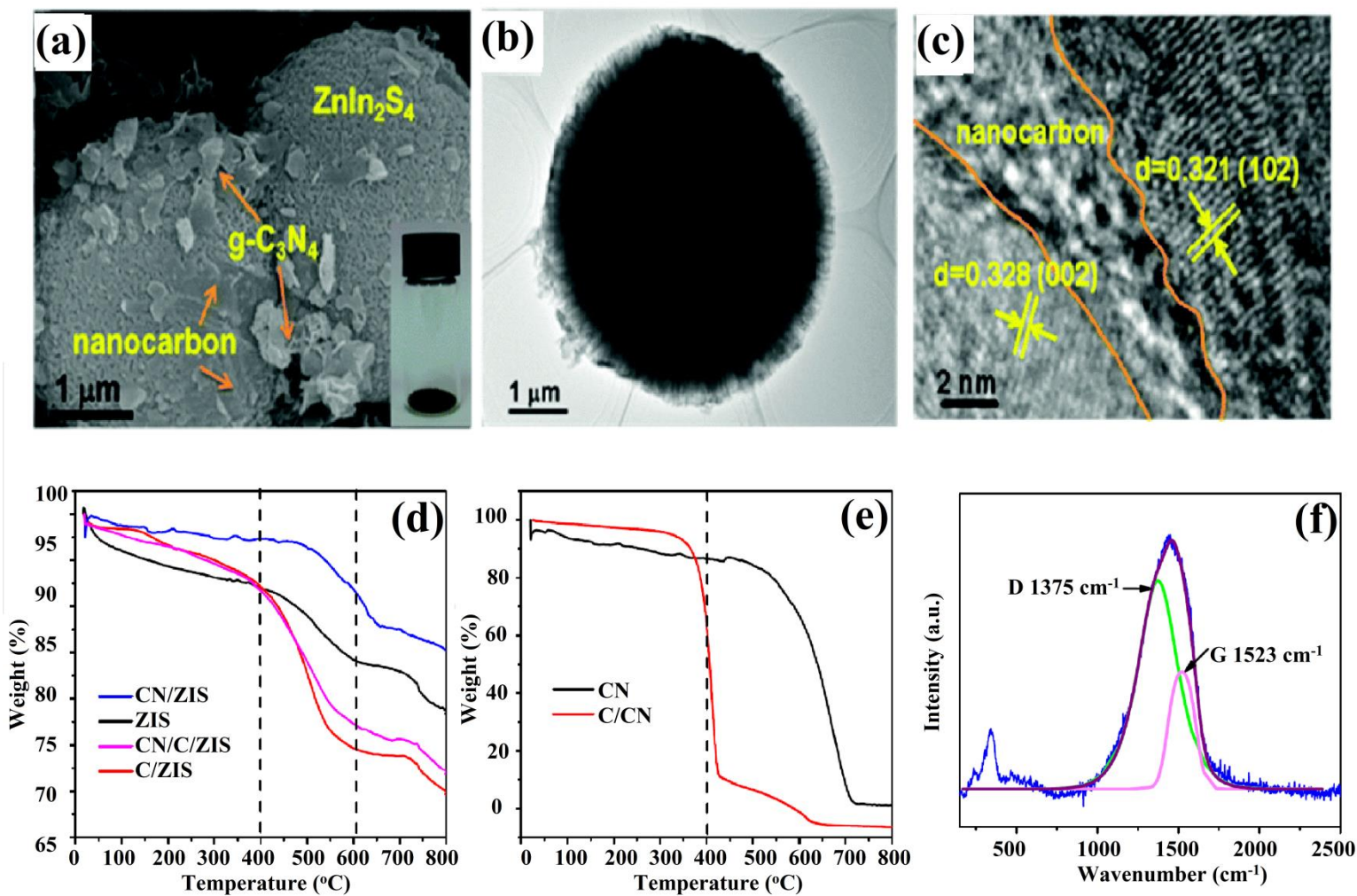
Fig. 10. (a) SEM image, (b) TEM image and (c) HR-TEM image of CN/C/ZIS nanocomposite. TG curves of the samples: (d) ZIS, CN/ZIS, C/ZIS and CN/C/ZIS; (e) CN and C/CN. (f) Raman spectra of CN/C/ZIS nanocomposite. CN represents g-C_3N_4. Reprinted with permission from RSC [133].
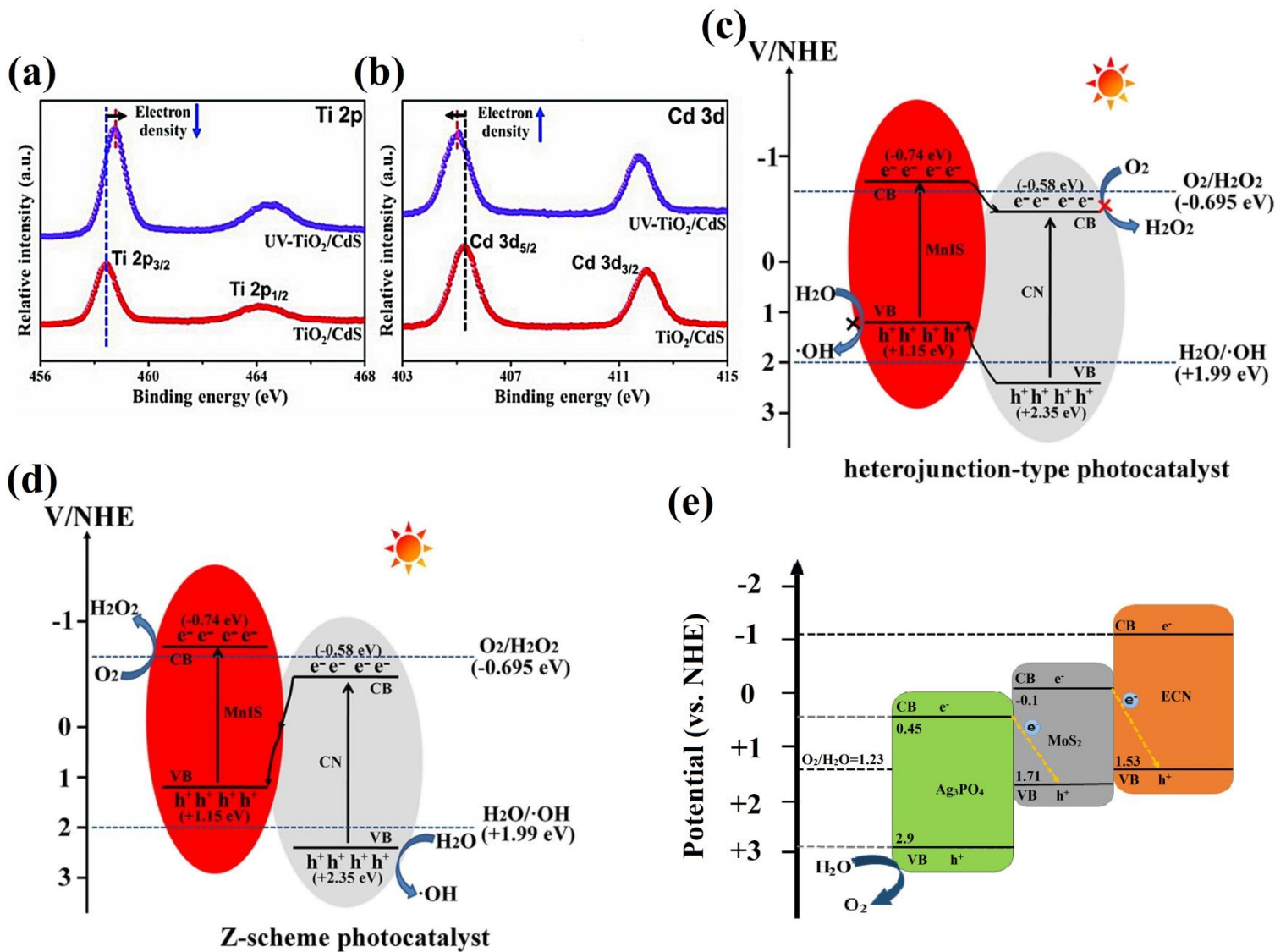
Fig. 11. Schematic illustrating the high-resolution XPS of: (a) Ti 2p and (b) Cd 3d in TiO_2/CdS nanocomposite, Reproduced with permission from Elsevier (License no. 4891850467496) [139] (c) Typical double charge transfer in $MnIn_2S_4/g-C_3N_4$ (MnIS/CN) heterojunction system, which do not form. (d) Direct Z-scheme MnIS/CN photocatalyst for H_2 production, reprinted with permission from Elsevier (Licence no. 4566470506559) [140]. (e) $Ag_3PO_4/MoS_2/g-C_3N_4$ ternary Z- scheme photocatalyst for O_2 evolution from overall water splitting, ECN represents modified $g-C_3N_4$ nanosheets.
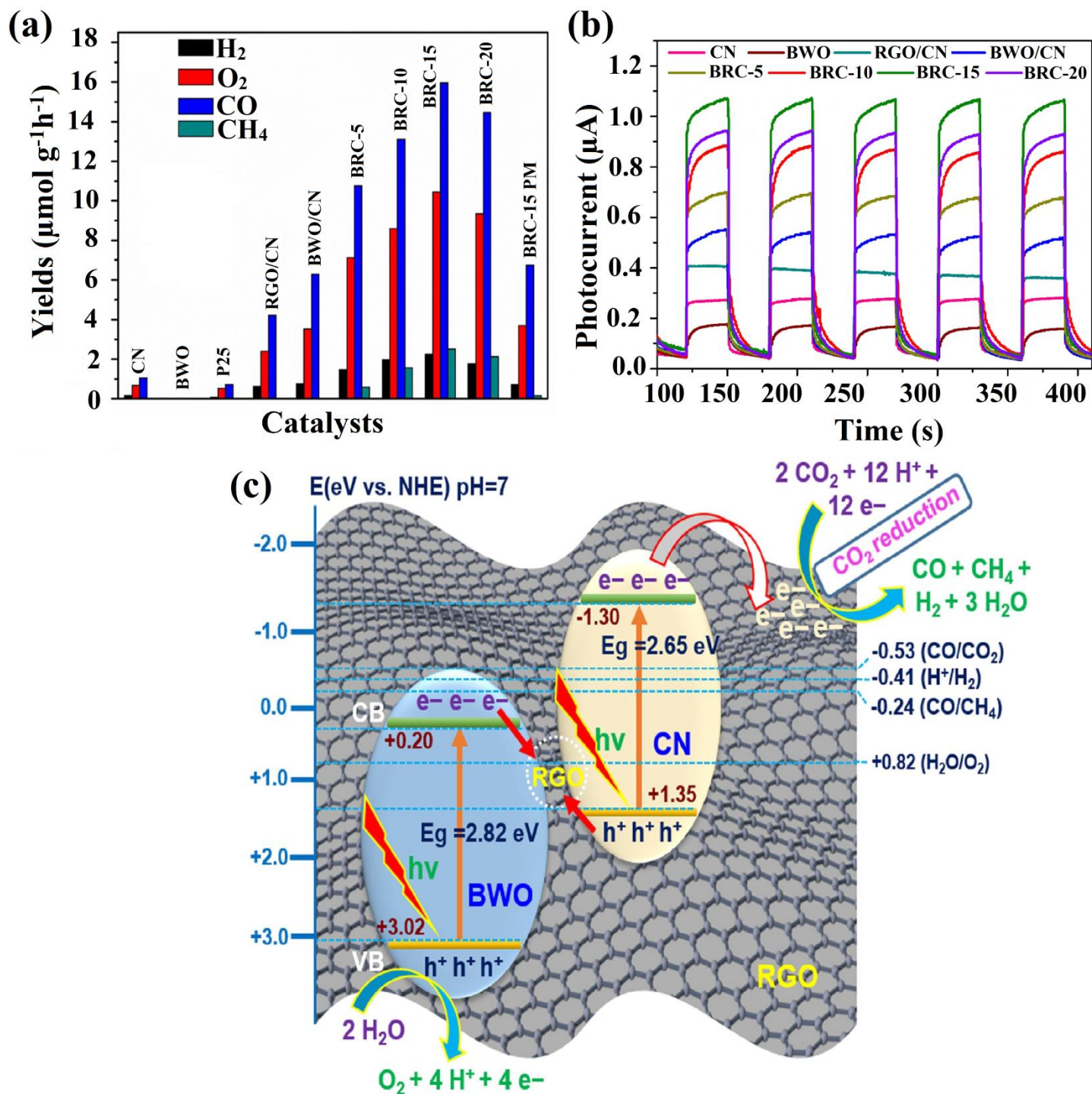
Fig. 12. (a) Comparison of the photoassisted CO, CH4, H2, and O2 production rates of all the synthesized photocatalysts under visible light illumination for 5 h. (b) Photocurrent responses of CN, BWO, BWO/CN, RGO/CN, and BWO/RGO/CN photocatalysts. (c) Schematic illustration of the proposed mechanism for CO_2 photoreduction in the BWO/RGO/CN nanohybrid. Reproduced with permission from Elsevier (License No. 4700150753077) [150].

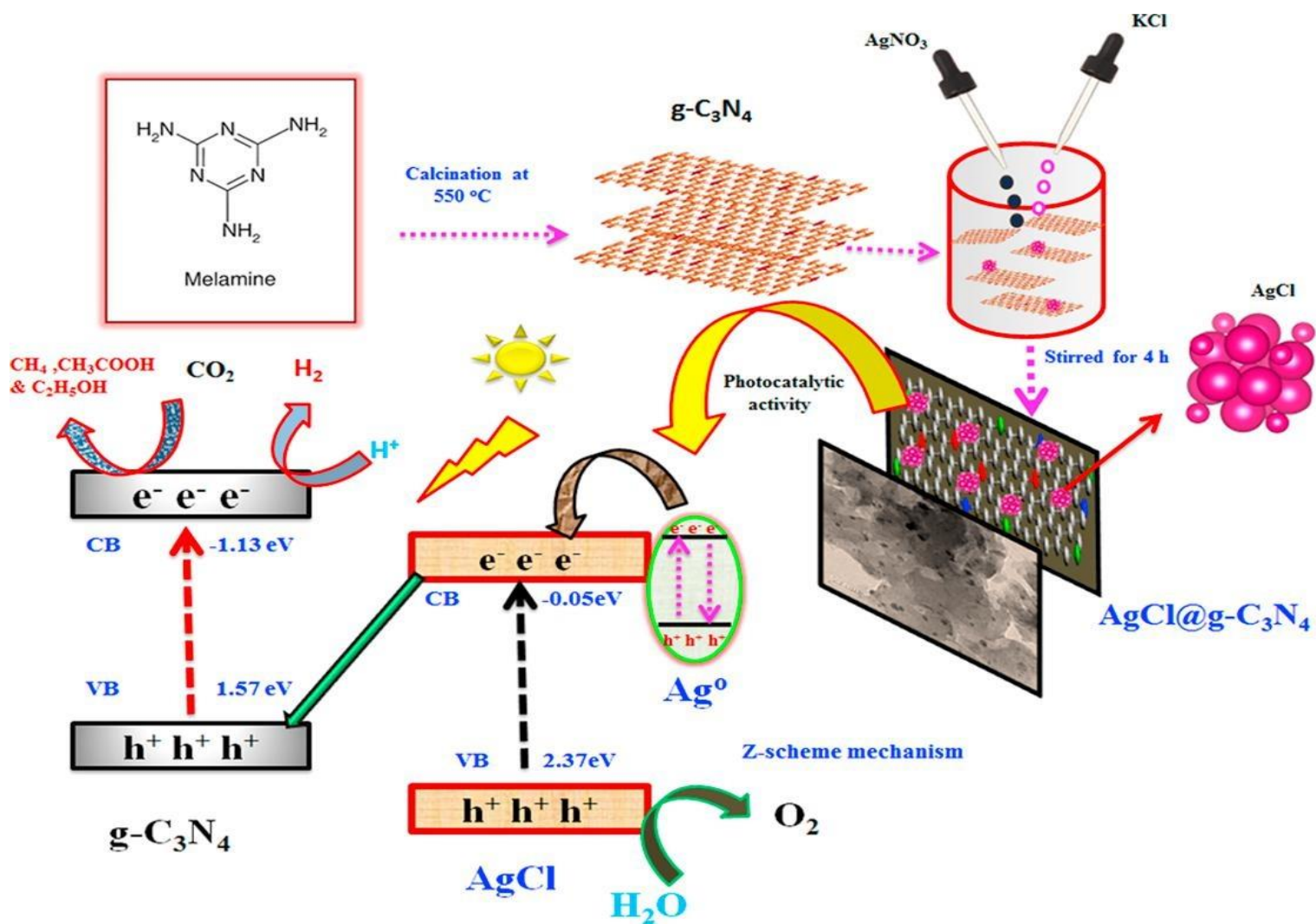**Fig. 13.** Synthesis route along with spatial charge separation of a direct Z-scheme AgCl@g-C_3N_4 photocatalyst for CO_2 reduction into CH_4, CH_3COOH and C_2H_5OH, reproduced with permission from Elsevier (Licence no. 4566480298200) [151].
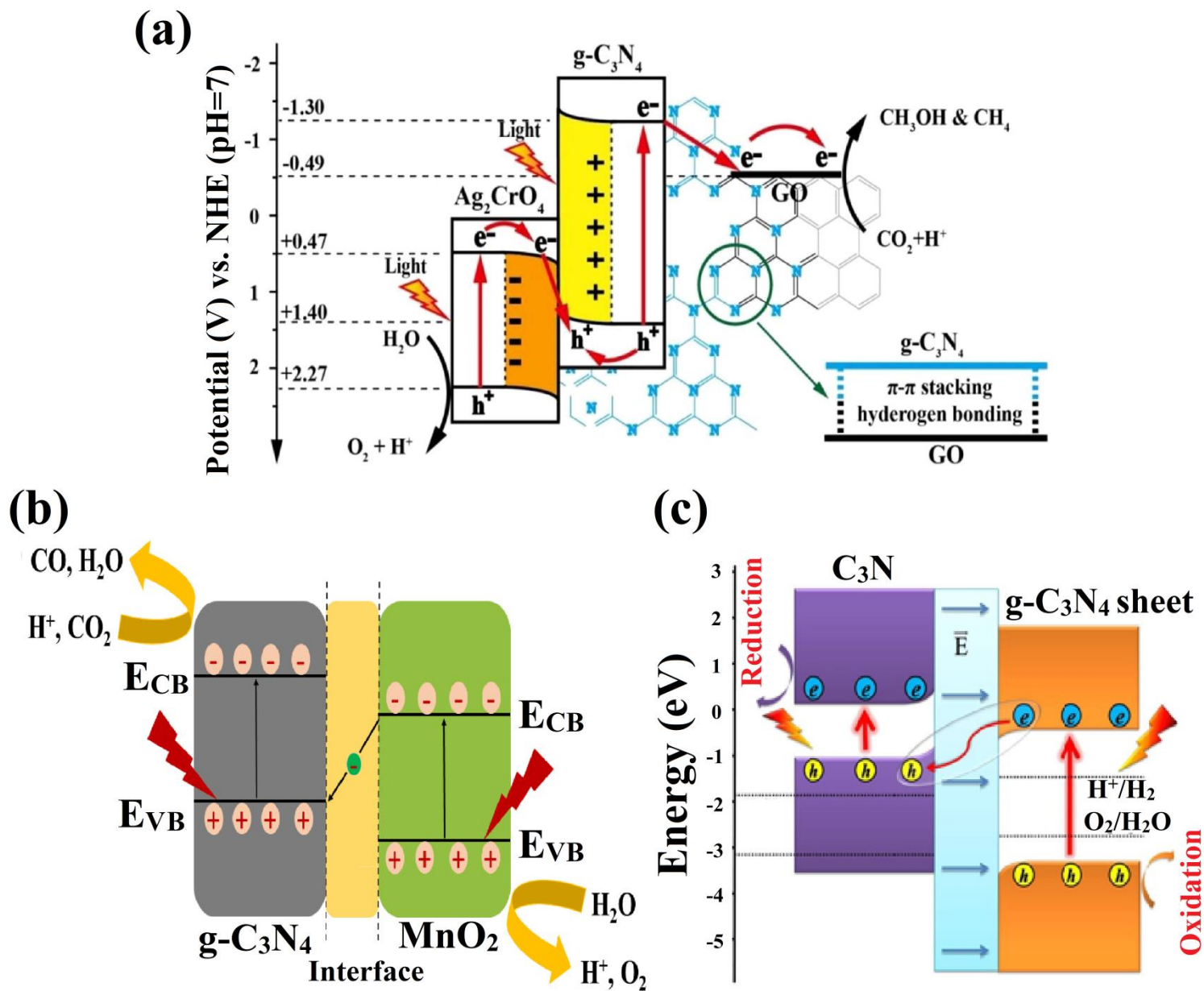
Fig. 14. Schematic representation of: (a) A novel ternary Ag_2CrO_4/g-C_3N_4/GO Z-scheme photocatalyst for CO_2 reduction into CH_3OH and CH_4, reproduced with permission from Elsevier (Licence no. 4566481143580) [152]. (b) Charge carrier migration in g-C_3N_4/MnO_2 photocatalyst through interfacial ohmic-contact, reprinted with permission from ACS [154], (c) Charge transfer pathway in metal free C_3N/g-C_3N_4 photocatalyst for overall water splitting [164].

(a) g-C₃N₄ C-TiO₂ diagram (Potential vs. NHE (eV))

(b) O₂ → H₂O₂ reaction scheme with g-C₃N₄ and Ga₂O₃

(c) ·CO₂⁻ EPR spectrum (Intensity (a.u.) vs. Magnetic Field (G))

(d) 2.4%Ga₂O₃-DBD/g-C₃N₄ photocurrent response (Photocurrent (μA) vs. Time (s))
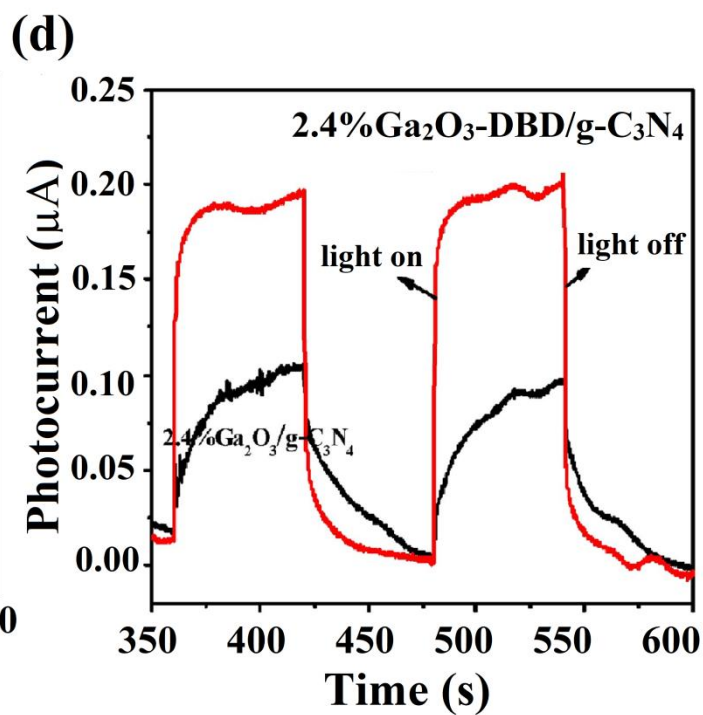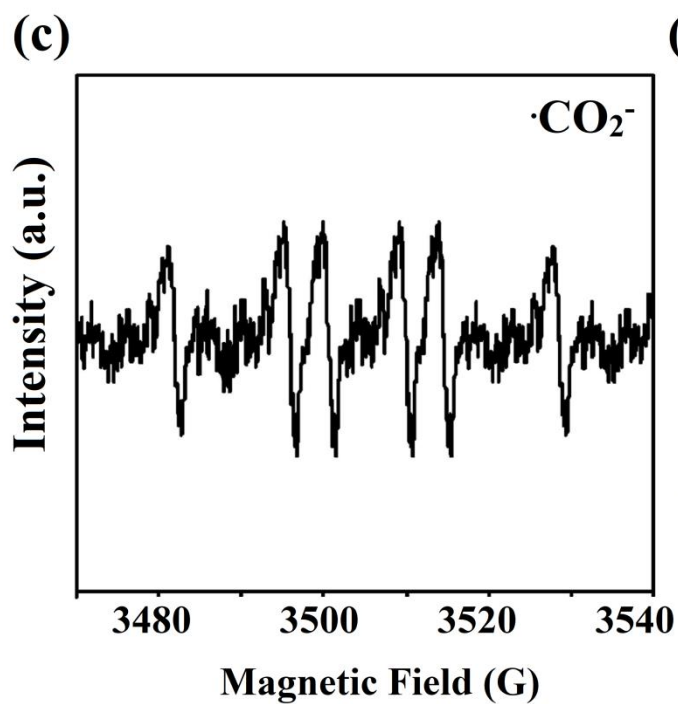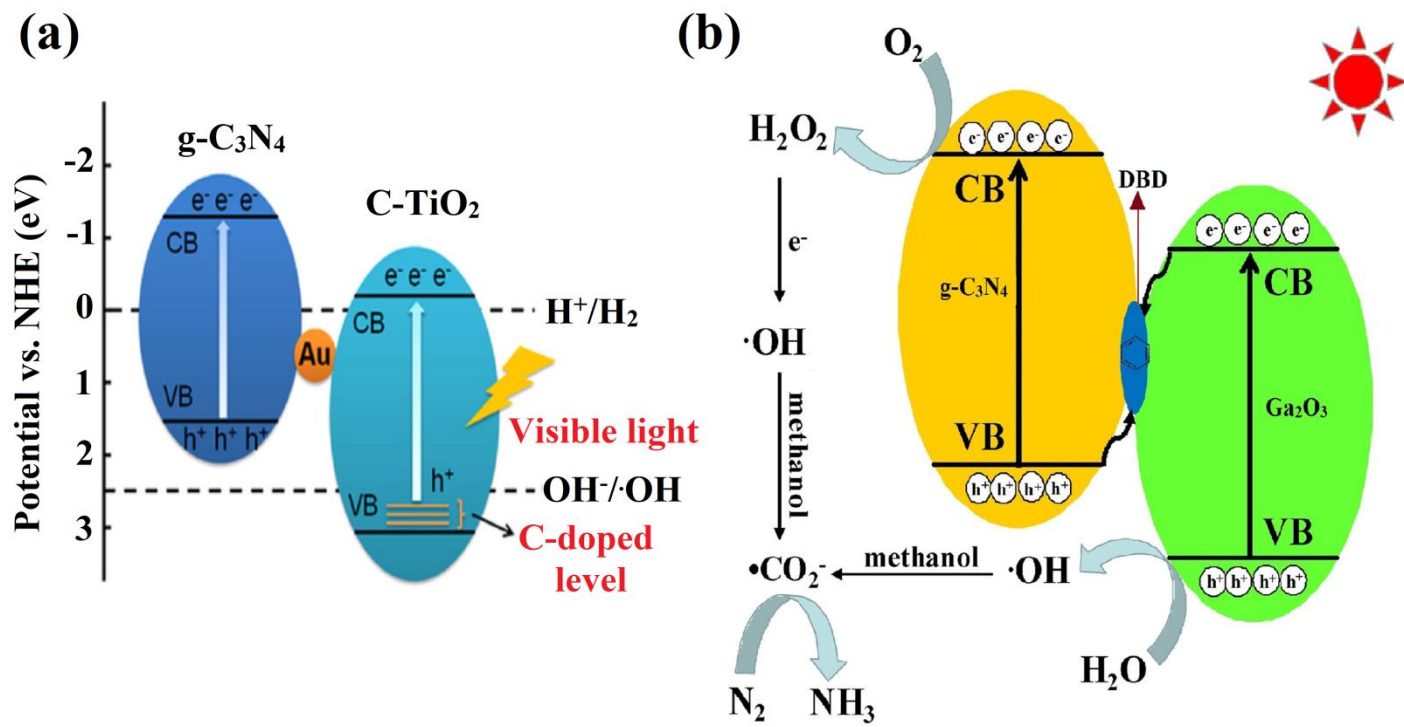
Fig. 15. Schematic representation of: (a) Au mediated all-solid-state Z-scheme photocatalyst for H_2 production, reprinted with permission from Wiley (license no. 4566490300093) [175], (b) 3,4-dihydroxybenzaldehyde (DBD) as an electron mediator in Ga_2O_3/g-C_3N_4 for visible light assisted photocatalytic N_2 fixation. (c) DMPO spin-trapping ESR spectra recorded for $\bullet CO_2^-$ in 0.2 mol L^{-1} methanol aqueous solution. (d) Photocurrent transient responses of 2.4%Ga_2O_3/g-C_3N_4 and 2.4%Ga_2O_3-DBD/g-C_3N_4, reproduced with permission from Elsevier (Licence no. 4703761323347) [179],
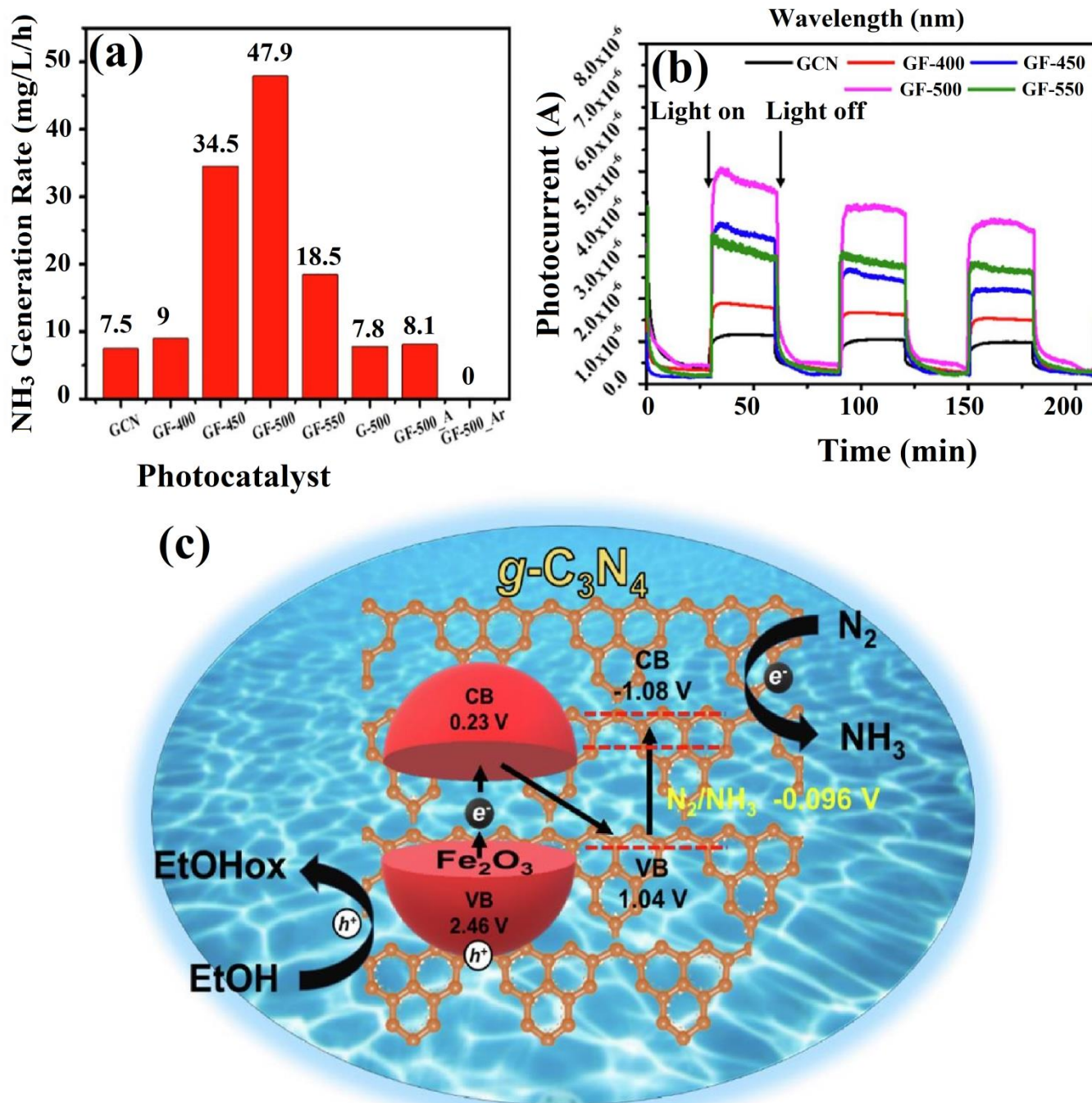
Fig. 16. (a) Rates of NH$_3$ generation of GCN, GF-400, GF-450, GF-500, GF-550, G-500, and HCl solution treated GF-500 (GF-500_A) as well as GF-500 in a control experiment with Ar. (b) Photocurrent generation analysis of different composites. (c) Schematic representation of photocatalytic N$_2$ reduction over Fe$_2$O$_3$ loaded g-C$_3$N$_4$. Reprinted with permission from Elsevier (License No. 4703770265600) [180].

Fig. 16. Conclusive overview of g-C₃N₄ based Z-scheme photocatalytic system.

Table

Table 1: *Summary of ASS Z-scheme photocatalytic systems for H_2 production and CO_2 reduction.*
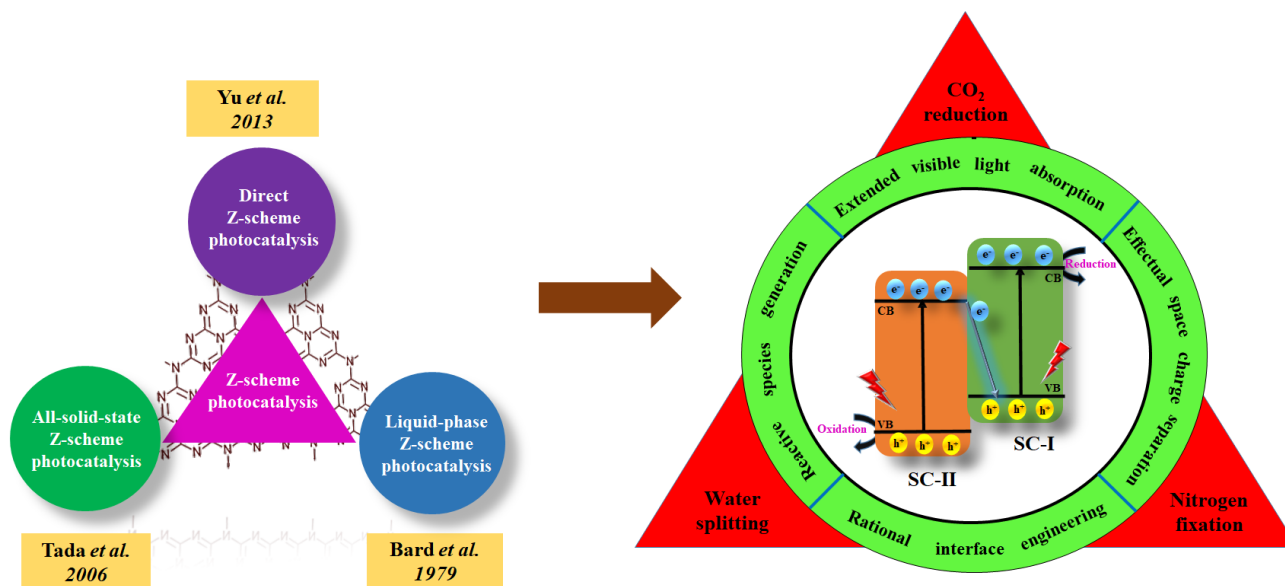
Photocatalyst	Solid-state electron mediator	Synthesis route	Active species	Application	Enhanced photocatalytic efficiency (%)/ Activity	Ref.
Zn0.5Cd0.5S-MWCNT-TiO$_2$	multi-walled carbon nanotubes (MWCNTs)	coating and hydrothermal route	-	H$_2$ production	Zn0.5Cd0.5S-MWCNT-TiO$_2$: 21.9 $\mu mol\ h^{-1}$	[186]
TiO$_2$/RGO/Metal sulphide	RGO	Photodeposition method		Overall water splitting	H$_2$ production :19.8 $\mu mol\ h^{-1}$ O$_2$ production : 10.3 $\mu mol\ h^{-1}$	[187]
CdS/RGO/g-C$_3$N$_4$	RGO	Hydrothermal process	e$^-$ and h$^+$	H$_2$ production and Atrazine degradation	**H$_2$ production :** CdS/RGO/g-C$_3$N$_4$: 1980.2 $\mu mol\ g^{-1}$ ***Atrazine degradation :*** CdS/RGO/g-C$_3$N$_4$: 90.50 %	[188]
PRGO/Ru/SrTiO$_3$: Rh (BiVO$_4$)	Photoreduced graphene oxide (PRGO)	Photoreduction method	h$^+$ and e$^-$	Overall water splitting	**H$_2$ production :** Ru/SrTiO$_3$:Rh/PRGO(BiVO$_4$) : 11 μmol ***O$_2$ production :*** Ru/SrTiO$_3$:Rh/PRGO(BiVO$_4$) : 5.5 μmol	[189]
ZnRh$_2$O$_4$/Au/Bi$_4$V$_2$O$_{11}$	Au	Calcination method	e$^-$ and h$^+$	Overall water splitting	**H$_2$ production :** ZnRh$_2$O$_4$/Au/Bi$_4$V$_2$O$_{11}$: 0.016 $\mu mol\ h^{-1}$ **O$_2$ production :** ZnRh$_2$O$_4$/Au/Bi$_4$V$_2$O$_{11}$: 0.088 $\mu mol\ h^{-1}$	[190]

g-C$_3$N$_4$/Ag/MoS$_2$	Ag	Calcination followed by photodeposition	•O$_2^-$, •OH, e$^-$ and h$^+$	RhB degradation, H$_2$ production	MoS$_2$: 16.2% g-C$_3$N$_4$: 50.02% g-C$_3$N$_4$/Ag/MoS$_2$: 95.8 % **H$_2$ production:** g-C$_3$N$_4$/Ag/MoS$_2$: 10.40 μmol h^{-1}	[191]
Cd$_x$Zn$_{1-x}$S/Au/g-C$_3$N$_4$	Au	Deposition method	e$_{CB}^-$	H$_2$ production	Cd$_{0.8}$Zn$_{0.2}$/Au/g-C$_3$N$_4$: 123 μmol h^{-1} g^{-1} (52.2×~ Au/g-C$_3$N$_4$) (8.63×~CdS/Au/g-C$_3$N$_4$)	[192]
C$_3$N$_4$/Au/CdZnS	Au	Hydrothermal followed by Deposition	e$^-$ and h$^+$	H$_2$ production	C$_3$N$_4$/Au/CdZnS : 24.6 mmolg^{-1} (6.3×~ C$_3$N$_4$/CdZnS)	[193]
g-C$_3$N$_4$/Au/P25	Au	Calcination method	e$^-$	H$_2$ production	g-C$_3$N$_4$/Au/P25 : 259 μmol h^{-1} g^{-1} (30 ×~g-C$_3$N$_4$)	[194]
g-C$_3$N$_4$-Ni-NiS	Ni	In-situ process	e$^-$	H$_2$ production	g-C$_3$N$_4$: 0.5% Ni :1.0 % NiS : 515 μmol h^{-1} g^{-1} (2.8 ×~g-C$_3$N$_4$-1.0 % NiS) (4.6 ×~g-C$_3$N$_4$-0.5 %Ni)	[195]
Ag$_3$PO$_4$/Ag/g-C$_3$N$_4$	Ag	In-situ process	h$^+$	O$_2$ evolution	Ag$_3$PO$_4$/Ag/g-C$_3$N$_4$: 19 μmol L^{-1}	[196]
g-C$_3$N$_4$/Au/C-TiO$_2$	Au	Photodeposition	•OH	H$_2$	20 % g-C$_3$N$_4$/2 % Au/C-TiO$_2$: 129 μmol h^{-1} g^{-1}	[175]

$Ag_3PO_4/g\text{-}C_3N_4$	Ag	In-situ deposition method	$\bullet O_2^-$ and h^+	CO_2 reduction	CO_2 reduction : 57.5 μmol $h^{-1}gcat^{-1}$	[197]
$g\text{-}C_3N_4/BiOBr/Au$	Au	Xe lamp irradiation	$\bullet O_2^-$	CO_2 reduction	$g\text{-}C_3N_4/BiOBr/Au\text{-}S$: CO : 0.39 $\mu mol\ h^{-1}\ g^{-1}$ CH_4 : 0.05 $\mu mol\ h^{-1}\ g^{-1}$	[198]

Table. 2. Summary of direct Z-scheme photocatalytic systems for various applications.

Photocatalyst	Synthesis route	Active species	Application	Enhanced photocatalytic efficiency (%)/ Activity	Ref.
$LaMnO_3/g\text{-}C_3N_4$	Heat-treatment method	h^+ and $\bullet O_2^-$	TC degradation	$LaMnO_3$(4.6 Wt %)/g-C_3N_4: 56.3 % $LaMnO_3$(9.8 Wt %)/g-C_3N_4: 61.4 % $LaMnO_3$(14.6 Wt%)/g-C_3N_4: 43.1 %	[201]
$\beta\text{-}CoOOH/g\text{-}C_3N_4$	Thermal polymerization followed by exfoliation	$\bullet O_2^-$, $\bullet OH$ and h^+	MO and phenol degradation	**MO degradation:** 15 % β-CoOOH/g-C_3N_4: 92.1 % **Phenol degradation:** 15%β-CoOOH/g-C_3N_4: 72.2 %	[202]
2D/2D g-C_3N_4/MnO_2	In-situ method	$\bullet O_2^-$ and $\bullet OH$	RhB and phenol degradation	**RhB degradation:** g-C_3N_4/MnO_2: 91.3 %, g-C_3N_4: 19.6 %, MnO_2: 22.3 % **Phenol degradation:** g-C_3N_4/MnO_2: 73.6 %, g-C_3N_4: 12.3 %, MnO_2: 35.4 %	[203]
g-C_3N_4/$NiWO_4$	Hydrothermal method	$\bullet OH$	Toluene degradation	**Removal efficiency:** g-C_3N_4/$NiWO_4$ (1C/1N): 95.3 % **Mineralization efficiency:** g-C_3N_4/$NiWO_4$ (1C/1N): 99.1 %	[204]

g-C₃N₄/CeO₂	Calcination method	•OH and h⁺	Methylene blue (MB) degradation	Degradation rates: g-C₃N₄/CeO₂: 0.246 h⁻¹	[205]
1D/2D V₂O₅/g-C₃N₄	Impregnation method	•O₂⁻ and •OH	Congo red (CR) degradation	V₂O₅ nanorods (VONRs): 5 % g-C₃N₄ nanosheets (CNNs): 34 % 4-VONRs/CNNs: 90 %	[206]
La₂NiO₄/g-C₃N₄	Mixed calcination route	h⁺ and •O₂⁻	MO degradation	La₂NiO₄(33 wt. %)/g-C₃N₄: 36.2 % g-C₃N₄: 12.4 %	[207]
PTCDA(Perylene-3,4,9,10-tetracarboxylic dianhydride)/g-C₃N₄	Calcination followed by hydrothermal	h⁺ and •O₂⁻	Photooxidation of benzylamine	---	[208]
Fe₂O₃-xSₓ/S-doped g-C₃N₄ (CNS)	One-pot in-situ process	•O₂⁻ and •OH	MB degradation	Fe₂O₃-xSₓ/ (CNS) (6.6 wt. % Fe₂O₃): 82 % Fe₂O₃: 28 % CNS: 54 %	[209]
LaFeO₃/g-C₃N₄	In-situ growth	h⁺ and •O₂⁻	MO and TC degradation	**MO degradation:** LaFeO₃/g-C₃N₄: 85 % **TC degradation:** LaFeO₃(2.0wt %)/g-C₃N₄ : 65.4 %	[210]
(BiO)₂CO₃/g-C₃N₄	Hydrothermal route	•O₂⁻, •OH and h⁺	RhB degradation	---	[211]
g-C₃N₄/Bi₂O₃@N-HMCs (CBH)	Thermal process	•O₂⁻, •OH and h⁺	Tetracycline hydrochloride (TCH) and ciprofloxacin hydrochloride (CFH) degradation	**TCH degradation:** CBH: 90 %, g-C3N4/Bi2O3: 68.78 %, g-C3N4/N-HMCs: 53.30%, Bi2O3/N-HMCs: 37.35%	[212]

				CFH degradation:	
				CBH: 78.06%	
Bi₂WO₆/g-C₃N₄	Hydrothermal process	•O₂⁻	RhB degradation	4% Bi₂WO₆/g-C₃N₄: 68%	[37]
BiOI/g-C₃N₄	In-situ transformation process	•O₂⁻ and •OH	Phenol degradation	---	[213]
β-Bi₂O₃/g-C₃N₄ (BC)	Combined hydrothermal-calcination method	h⁺ and •O₂⁻	RhB degradation	BC70: 98% g-C₃N₄: 87% β-Bi₂O₃: 67%	[214]
Bi₂O₃/g-C₃N₄	In-situ fabrication	h⁺ and •O₂⁻	Phenol degradation	---	[215]
Bi₂O₃/g-C₃N₄	One-step calcination method	•O₂⁻, •OH and h⁺	MB degradation	Photocatalytic activity rate constant : 0.063 min⁻¹	[216]
WO₃/g-C₃N₄/Bi₂O₃ (CWB)	One-step co-calcination method	•O₂⁻, •OH and h⁺	TC degradation	CWB: 80.2%, WO₃/g-C₃N₄: 48.54%, Bi₂O₃/g-C₃N₄: 44.53%	[217]
FeWO₄ nanorodg-C₃N₄ (FWO/g-CN)	In-situ hydrothermal method	•O₂⁻, •OH and h⁺	Salicylic acid (SA) degradation	FWO/g-C₃N₄: 95 % g-C₃N₄: 36%	[218]
N-K₂Ti₄O₉/g-C₃N₄/UiO-66	Calcination	•O₂⁻, •OH and h⁺	RhB degradation	---	[219]
g-C₃N₄/α-Fe₂O₃	In-situ	h⁺ and •O₂⁻	RhB degradation	g-C₃N₄/α-Fe₂O₃: 99 %, g-C₃N₄: 67 %, α-Fe₂O₃: 6 %	[123]
Monoclinic-Bi₂O₄/nitrogen doped carbondots (m-Bi₂O₄/NCDs)	One-step hydrothermal method	h⁺ and •O₂⁻	MO and phenol degradation	**MO degradation:** m-Bi₂O₄/NCDs-4: 94.3 %, m-Bi₂MO₃: 8.64 % **Phenol degradation:** m-Bi₂O₄/NCDs-3: 96.8 %, m-	[50]

				Bi_2MO_3: 70.4 %,	
3:7 BiVO₄/g-C₃N₄	Calcination	•O₂⁻ and •OH	RhB degradation	3:7 BiVO₄/g-C₃N₄ = 10.36×~g-C₃N₄ 3:7 BiVO₄/g-C₃N₄ = 10.68×~BiVO₄	[220]
MnIn₂S₄/g-C₃N₄ (MnISCN)	Hydrothermal route	h⁺ and •O₂⁻	TCH degradation and H₂ production	**TCH degradation:** MnIn₂S₄: 60.5 % **H₂ production:** MnISCN-20: 200.8 μmol h⁻¹ g⁻¹ (3.5×~MnIS)	[116]
g-C₃N₄/0D-ZnO (CN/0DZnO)	Solution conversion, calcination and exfoliation	•O₂⁻ and •OH	4-chlorophenol (4CP)degradation and H₂ production	**4CP degradation:** CN-10/0D-ZnO: 95 %, 0D-ZnO: 64.2 %, g-C₃N₄: 34.2 % **H₂ production:** CN-20/0D-ZnO: 32.2 μmol h⁻¹ (5×~g-C₃N₄)	[221]
Fe₂O₃/g-C₃N₄	Electrostatic self-assembly method	e⁻ and h⁺	H₂ production	10 % Fe₂O₃/g-C₃N₄: 398.0 μmol h⁻¹ g⁻¹ (13×~g-C₃N₄)	[222]
α-Fe₂O₃/g-C₃N₄	Solvothermal and calcination	•O₂⁻ and •OH	Overall water splitting	**H₂ production:** 38.2 μmol h⁻¹ g⁻¹ **O₂ production:** 19.1 μmol h⁻¹ g⁻¹	[223]

Photocatalyst	Synthesis method	Reactive species	Application	Performance	Ref.
ZnO/ZnS/g-C$_3$N$_4$	Two-step chemical route	--	H$_2$ production	ZnO/ZnS/g-C$_3$N$_4$: 1205 8 µmol g^{-1} ZnO/ZnS: 768 µmol g^{-1}	[224]
N-ZnO/g-C$_3$N$_4$	calcination	•O$_2^-$ and •OH	H$_2$ production	N-ZnO/g-C$_3$N$_4$: 152.7 µmol h^{-1} ZnO/g-C$_3$N$_4$: 36.4 µmol h^{-1} g-C$_3$N$_4$: 28.6 µmol h^{-1}	[225]
Bi$_2$O$_2$CO$_3$/g-C3N4	In-situ thermal growth	e$^-$, h$^+$ and •OH	H$_2$ production	Bi$_2$O$_2$CO$_3$/g-C$_3$N$_4$: 965 µmol h^{-1} g^{-1} g-C$_3$N$_4$:337 µmol h^{-1} g^{-1}	[226]
g-C$_3$N$_4$/PSi	Magnesiothermic reduction and polycondensation	e$^-$	H$_2$ production	g-C$_3$N$_4$/(2.50 wt. %) PSi: 870.4 µmol h^{-1} g^{-1} (2×~g-C$_3$N$_4$)	[227]
WO$_3$/g-C$_3$N$_4$/Ni(OH)$_x$	Calcination and photodeposition	•O$_2^-$ and •OH	H$_2$ production	20 wt. % WO$_3$/g-C$_3$N$_4$/4.8 wt. % Ni(OH)$_x$: 576 µmol h^{-1} g^{-1} (10.8×~20 wt. % WO$_3$/g-C$_3$N$_4$)	[228]
NiCo$_2$O$_4$/g-C$_3$N$_4$	Calcination and hydrothermal method	h$^+$	H$_2$ production	17.5 wt %-NiCo$_2$O$_4$/g-C$_3$N$_4$: 5480 µmol h^{-1} g^{-1}	[229]
Mo-Mo$_2$C/g-C$_3$N$_4$	Ultrasound assisted deposition method	--	H$_2$ production	2.0 wt % Mo-Mo$_2$C/g-C$_3$N$_4$: 219.7 µmol h^{-1} g^{-1} (440×~g-C$_3$N$_4$, 3.6×~2.0 wt. % Mo$_2$C/g-C$_3$N$_4$)	[230]
KTa$_{0.75}$Nb$_{0.25}$ (KTN)/g-C$_3$N$_4$	Microwave heating	--	H$_2$ production	(KTN)/g-C$_3$N$_4$: 1673 µmol h^{-1} g^{-1} (2.5×~ KTN) (2.4×~g-C$_3$N$_4$)	[231]
2D/2D WO3/g-C$_3$N$_4$	Ultrasonication and two-step thermal-etching	•O$_2^-$	H$_2$ production	15 % WO$_3$/g-C$_3$N$_4$: 982 µmol h^{-1} g^{-1} (1.7×~g-C$_3$N$_4$)	[232]
g-C$_3$N$_4$-CoNiSe	Calcination under N$_2$ atmosphere	e$^-$	H$_2$ production	CN-CoNiSe = 87.4×~ g-C$_3$N$_4$	[233]

Material	Synthesis Method	Reactive species	Application	Performance	Ref.
$WO_3/g\text{-}C_3N_4$	Pyrolysis	--	H_2 production	9 % $WO_3/g\text{-}C_3N_4$: 11,000 $\mu mol\ g^{-1}$	[234]
2D $SnS_2/g\text{-}C_3N_4$	Microwave assisted	e^-	H_2 production	5wt % $SnS_2/g\text{-}C_3N_4$: 972.6 $\mu mol\ h^{-1}\ g^{-1}$	[235]
Metakaolin/$g\text{-}C_3N_4$ (MK/CN)	One-pot heating treatment	e^-	H_2 production	MK/CN-70.4 % : 288 $\mu mol\ h^{-1}\ g^{-1}$ ($1.5\times\sim g\text{-}C_3N_4$)	[236]
$g\text{-}C_3N_4\text{-}Ni_2P\text{-}MoS_2$	In-situ phosphorization reaction	--	H_2 production	$g\text{-}C_3N_4$-1 % Ni_2P-1.5 % MoS_2 : 532.41 $\mu mol\ h^{-1}\ g^{-1}$ ($2.47\times\sim g\text{-}C_3N_4$-1.5 % MoS2) ($5.15\times\sim g\text{-}C3N4$-1 % Ni_2P)	[237]
Cu-loaded $g\text{-}C_3N_4$/1D hydrogenated black TiO_2 nanofiber (CuCNBTNF)	Electrospinning process followed by thermal treatment	$\bullet O_2^-$	H_2 production	CuCNBTNF-5: 3.3 $mmol\ h^{-1}\ g^{-1}$	[238]
SnO_2-coupled boron and phosphorus co-doped $g\text{-}C_3N_4$(SO/B-P-CN)	Calcination	$\bullet OH$	CO_2 reduction	6SO/0.12B-0.2P-CN: 49 $\mu mol\ h^{-1}\ g^{-1}$ ($9\times\sim g\text{-}C_3N_4$)	[239]
$g\text{-}C_3N_4$/ZnO	Hydrothermal-calcination process	$\bullet OH$ and e^-	CO_2 reduction	CH_3OH production: $g\text{-}C_3N_4$/ZnO: 1.32 $\mu mol\ h^{-1}\ g^{-1}$, ($2.1\times\sim ZnO$), ($4.1\times\sim\mu mol\ h^{-1}\ g^{-1}$)	[240]
Porous $g\text{-}C_3N_4/Sn_2S_3^-$ diethylenetriamine (Pg-$C_3N_4/Sn_2S_3^-$DETA)	Hydrothermal process	e^- and h^+	CO_2 reduction	5 % Pg-$C_3N_4/Sn_2S_3^-$DETA : CH_4: 4.93 $\mu mol\ h^{-1}\ g^{-1}$ CH_3OH: 1.49 $\mu mol\ h^{-1}\ g^{-1}$	[241]
$g\text{-}C_3N_4$/ZIF-67	Aging process	e^- and h^+	CO_2 reduction	C_2H_5OH production: $g\text{-}C_3N_4$/ZIF-67: 325.5 $\mu mol.\ gcat^{-1}$ ($2\times\sim g\text{-}C_3N_4$)	[242]
$g\text{-}C_3N_4/SnS_2$	Hydrothermal process	e^- and h^+	CO_2 reduction	CH_3OH production: $g\text{-}C_3N_4/SnS_2$: 2.3 $\mu mol\ g^{-1}$ CH_4 production: $g\text{-}C_3N_4/SnS_2$: 0.64 $\mu mol\ g^{-1}$	[243]
$Cu_2V_2O_7/g\text{-}C_3N_4$	Hydrothermal and calcination	e^- and h^+	CO_2 reduction	CH_4 production: 50 $Cu_2V_2O_7$/50 $g\text{-}C_3N_4$: 305 $\mu mol.\ g^{-1}cat.\ h^{-1}$ CO production: 50 $Cu_2V_2O_7$/50 $g\text{-}C_3N_4$: 166 $\mu mol.\ g^{-1}cat.\ h^{-1}$ O_2 production: 50 $Cu_2V_2O_7$/50$g\text{-}C_3N_4$: 706 $\mu mol.\ g^{-1}cat.\ h^{-1}$	[58]
$CdS/g\text{-}C_3N_4$	Polycondensation and hydrothermal method	e^- and h^+	CO_2 reduction	Methyl formate production: 1 % CdS/2 % $g\text{-}C_3N_4$: 1352.07 $\mu mol.\ g^{-1}cat.\ h^{-1}$	[244]